AFRL-RV-PS-
TR-2016-0012

AFRL-RV-PS-
TR-2016-0012

TOWARD UNIFIED CORRECTION OF REGIONAL PHASES FOR AMPLITUDE AND TRAVEL TIME EFFECTS OF HETEROGENEOUS STRUCTURE

T. Lay, et al.

University of California Santa Cruz
Department of Earth and Planetary Sciences
1156 High Street
Santa Cruz, CA 95064

04 November 2015

Final Report

APPROVED FOR PUBLIC RELEASE; DISTRIBUTION IS UNLIMITED.

AIR FORCE RESEARCH LABORATORY
Space Vehicles Directorate
3550 Aberdeen Ave SE
AIR FORCE MATERIEL COMMAND
KIRTLAND AIR FORCE BASE, NM 87117-5776

DTIC COPY

NOTICE AND SIGNATURE PAGE

Using Government drawings, specifications, or other data included in this document for any purpose other than Government procurement does not in any way obligate the U.S. Government. The fact that the Government formulated or supplied the drawings, specifications, or other data does not license the holder or any other person or corporation; or convey any rights or permission to manufacture, use, or sell any patented invention that may relate to them.

This report was cleared for public release by the PRS OPSEC Office and is available to the general public, including foreign nationals. Copies may be obtained from the Defense Technical Information Center (DTIC) (http://www.dtic.mil).

AFRL-RV-PS-TR-2016-0012 HAS BEEN REVIEWED AND IS APPROVED FOR PUBLICATION IN ACCORDANCE WITH ASSIGNED DISTRIBUTION STATEMENT.

//SIGNED//	//SIGNED//
Robert Raistrick Project Manager, AFRL/RVBYE	Glenn M. Vaughan, Colonel, USAF Chief, Battlespace Environment Division

This report is published in the interest of scientific and technical information exchange, and its publication does not constitute the Government's approval or disapproval of its ideas or findings.

REPORT DOCUMENTATION PAGE

Form Approved
OMB No. 0704-0188

Public reporting burden for this collection of information is estimated to average 1 hour per response, including the time for reviewing instructions, searching existing data sources, gathering and maintaining the data needed, and completing and reviewing this collection of information. Send comments regarding this burden estimate or any other aspect of this collection of information, including suggestions for reducing this burden to Department of Defense, Washington Headquarters Services, Directorate for Information Operations and Reports (0704-0188), 1215 Jefferson Davis Highway, Suite 1204, Arlington, VA 22202-4302. Respondents should be aware that notwithstanding any other provision of law, no person shall be subject to any penalty for failing to comply with a collection of information if it does not display a currently valid OMB control number. **PLEASE DO NOT RETURN YOUR FORM TO THE ABOVE ADDRESS.**

1. REPORT DATE *(DD-MM-YYYY)* 04-11-2015	**2. REPORT TYPE** Final Report	**3. DATES COVERED** *(From - To)* 03 Aug 2012 to 04 Aug 2015

4. TITLE AND SUBTITLE
Toward Unified Corrections of Regional Phases for Amplitude and Travel Time Effects of Heterogeneous Structure

5a. CONTRACT NUMBER
FA9453-12-C-0234

5b. GRANT NUMBER

5c. PROGRAM ELEMENT NUMBER
62601F

6. AUTHOR(S)
T. Lay, X.-B. Xie, and X. Yang

5d. PROJECT NUMBER
1010

5e. TASK NUMBER
PPM00014494

5f. WORK UNIT NUMBER
EF007787

7. PERFORMING ORGANIZATION NAME(S) AND ADDRESS(ES)
University of California Santa Cruz
Department of Earth and Planetary Sciences
1156 High Street
Santa Cruz, CA 95064

8. PERFORMING ORGANIZATION REPORT NUMBER

9. SPONSORING / MONITORING AGENCY NAME(S) AND ADDRESS(ES)
Air Force Research Laboratory
Space Vehicles Directorate
3550 Aberdeen Avenue SE
Kirtland AFB, NM 87117-5776

10. SPONSOR/MONITOR'S ACRONYM(S)
AFRL/RVBYE

11. SPONSOR/MONITOR'S REPORT NUMBER(S)
AFRL-RV-PS-TR-2016-0012

12. DISTRIBUTION / AVAILABILITY STATEMENT
Approved for public release: distribution is unlimited. (377ABW-OPS-16-1057 dtd 10 Feb 2016)

13. SUPPLEMENTARY NOTES

14. ABSTRACT

We analyze variability of the Pn seismic phase associated with regionally varying seismic velocity structure, seeking to establish self-consistent correction of geometric spreading effects on Pn and regional travel time calculations. This effort has included calculations of frequency-dependent Pn geometric spreading behavior for specific regionally varying 1D structures. We consider a suite of models with varying velocity gradients to establish basic behavior and then explore 2D models with lateral variations in gradient structure. Finite-difference calculations have also explored the effects of small-scale heterogeneity imposed on regional structures to evaluate the stability of frequency-dependent spreading corrections, extending such calculations from 1 Hz as analyzed under a previous contract to 6-10 Hz. We compare the results for various models with calculations for standard assumptions of frequency- independent power law geometric spreading correction models commonly used to correct Pn amplitudes. Pn data analysis for geometric spreading and attenuation from 2 to 10 Hz for the North Korean nuclear tests at stations in northeast China is reported, and the relative effects of oceanic paths on observations of Pn in Japan near 1000 km distance is modeled with 2D laterally varying structures. We compute synthetics for structures in Eurasia based on RSTT (Regional Seismic Travel Time) models and empirically based models that match the observed Pn spreading, contrasting the behavior with standard power-law spreading assumptions. The regional models with Earth flattening and variable lid gradients provide reasonable attenuation estimates and reduced frequency dependence of attenuation. A 2D tomographic Pn velocity gradient model is determined for Eurasia.

15. SUBJECT TERMS
Regional seismic phases, Pn amplitudes, Pn geometric spreading

16. SECURITY CLASSIFICATION OF:			**17. LIMITATION OF ABSTRACT**	**18. NUMBER OF PAGES**	**19a. NAME OF RESPONSIBLE PERSON** Robert Raistrick
a. REPORT Unclassified	**b. ABSTRACT** Unclassified	**c. THIS PAGE** Unclassified	Unlimited	124	**19b. TELEPHONE NUMBER** *(include area code)*

This page is intentionally left blank.

Table of Contents

Approved for public release; distribution is unlimited.

List of Figures

Approved for public release; distribution is unlimited.

Approved for public release; distribution is unlimited.

Approved for public release; distribution is unlimited.

Approved for public release; distribution is unlimited.

Approved for public release; distribution is unlimited.

Approved for public release; distribution is unlimited.

Approved for public release; distribution is unlimited.

Approved for public release; distribution is unlimited.

This page is intentionally left blank.

Approved for public release; distribution is unlimited.

1. SUMMARY

Regional seismic phases (e.g., *Pn*, *Sn*, *Pg*, *Lg*) play a very important role in global monitoring of low yield underground nuclear tests. Given a typical paucity of teleseismic observations for a small event, regional phase arrival times can be critical for locating the source. Numerous empirical observations have also shown that regional phases hold the keys to small event magnitude and yield estimation and to discrimination between small explosions and earthquakes (e.g., Taylor et al., 1989; Kim et al., 1997; Walter et al., 1995; Fisk et al., 1996, 2005; Taylor, 1996; Taylor and Hartse, 1997; Hartse et al., 1997; Patton, 2001; Xie, 2002; Richards and Kim 2007; Zhao et al., 2008). Use of travel times and amplitudes of regional phases for location, discrimination and yield estimation procedures requires that the regional velocity and attenuation structures be sufficiently well approximated (e.g., Myers et al., 2010). As a result there have been extensive efforts to determine regional crustal and upper mantle velocity models and tomographic models for attenuation of regional phases. These efforts commonly proceed independently, with geometric spreading models being used for simple or generic structures even while detailed regional velocity models are determined for travel times. This situation is evolving, with an increasing emphasis on model-based procedures rather than on empirical data trends entering into operational systems, and this presents both challenges and opportunities for developing self-consistent model-based procedures. The guiding theme of this project is working toward unified, self-consistent correction of regional phases for amplitude and travel time effects of heterogeneous Earth structure. Our focus is on the critical regional phase *Pn*, which traverses the uppermost mantle, and commonly is assumed to have very simple wave behavior controlling its amplitudes and travel times. In fact, Pn has complex sensitivity to Earth structure that is not well represented by standard processing assumptions (particularly when determining attenuation models needed for the model-based procedures), motivating use of regionally appropriate velocity structures, just as are motivated for precise event location. Striving toward self-consistency of regional structures used for travel time and amplitude analysis is a logical step as model-based approaches are adopted in the operational environment.

2. INTRODUCTION

This project builds on a prior collaboration in which we developed geometric spreading corrections for regional phases *Pn* and *Sn* for simple reference velocity models and applied these to develop frequency-dependent *Pn* attenuation models for Eurasia. We confirmed that these seismic phases have acute sensitivity to structure, with frequency-dependent geometric spreading behavior for even the simplest spherical structures. The sensitivity to mantle-lid velocity gradient is non-linear and pronounced, but can be characterized well by numerical modeling for specific structures. Current procedures tend to ignore the complex geometric spreading of these phases and thus likely project artificial frequency dependence into attenuation models for the mantle lid. Practical determination of precise regional mantle-lid velocity gradients is challenging, but possible if curvature of *Pn* and *Sn* travel time branches is constrained in a local region. This is exactly what is being performed in RSTT (regional seismic travel time) approaches, although data scatter and trade-off with variable crustal legs certainly reduces confidence in inferred mantle-lid radial velocity gradients. We examine the predictions of RSTT and similar models for amplitude effects, considering both the implications for associated frequency-dependent attenuation models and the prospects of jointly using amplitude and travel time information to better constrain the regional velocity and attenuation structures. Eurasian datasets of regional *Pn* phases are utilized, and our previous work on determining frequency-dependent geometric spreading as a function of 1D velocity model variations is expanded to provide corrections for laterally varying regional composites. We extending our current (up to 10 Hz) 2D finite-difference modeling efforts to more realistic media. The ultimate goal is to work toward procedures for determining regional attenuation and velocity models that are useful for self-consistently correcting both travel-time and amplitude measurements for improved event location, event identification and magnitude/yield determination.

3. BACKGROUND AND TECHNICAL APPROACH

3.1 *Pn and Sn geometric spreading*

Accurately accounting for geometric spreading is critical for the development of meaningful regional-phase attenuation models. This is particularly true for *Pn* and *Sn* waves because the nature of their wave propagation renders them acutely sensitive to uppermost mantle velocity structure and Earth's sphericity. Even simple one-dimensional (1D) velocity models can produce geometric spreading of *Pn* and *Sn* that is strongly dependent on frequency (e.g., Sereno and Given, 1990; Yang et al., 2007; Avants et al., 2011). If frequency dependence of the geometric spreading is neglected, any inferred attenuation model based on using that geometric spreading will acquire incorrect frequency dependence.

In our previous modeling efforts, we generated synthetic seismograms for a 1D, spherical Earth model (Yang et al., 2007; Avants et al., 2011) to simulate *Pn* and *Sn* geometric spreading in such a structure. We used the same generic spherical Earth model considered by Sereno and Given (1990) as the Base Earth Model for our simulations (Figure 1) and developed new *Pn* and *Sn* geometric-spreading models using the synthetics from the simulation.

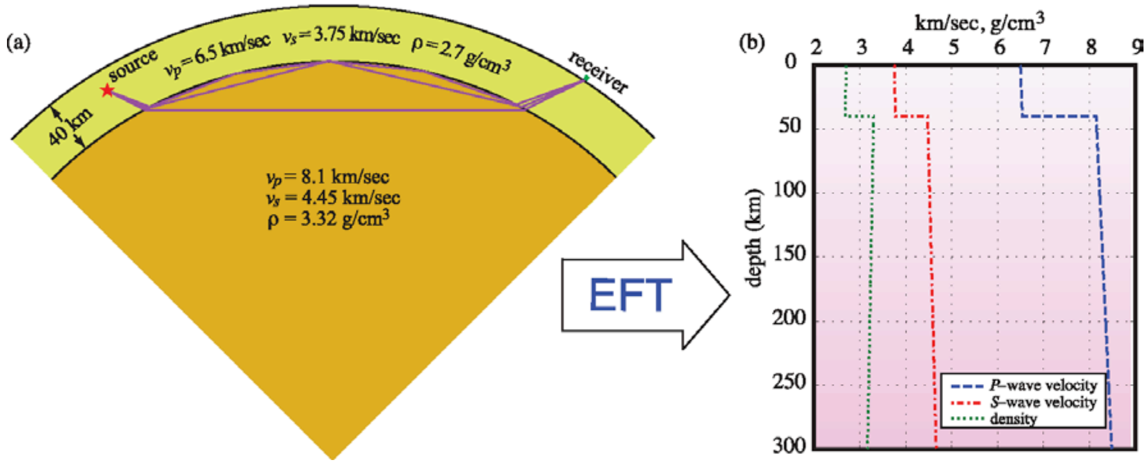

Figure 1. Base Earth Model used for *Pn* and *Sn* simulations and the development of new *Pn* and *Sn* geometric-spreading models. Quality factor *Q* is infinite throughout the model. Earth flattening transform yields the 1D models on the right, which have mild positive velocity gradients even though the mantle lid has constant velocity in the spherical structure.

We computed synthetic seismograms using the source parameterizations and procedures described in detail by Yang et al. (2007) and extracted the *Pn* and *Sn* portions of the synthetic seismograms using fixed-velocity windows. We measured *Pn* and *Sn* amplitudes from the spectra calculated using the *Pn* and *Sn* synthetic seismograms. The 10-Hz *Pn* amplitude decay in the spherical Base Earth Model is shown in Figure 2. Also plotted in the figure is the amplitude decay of a conical head wave in a plane one-layer-over-half-space model (Aki and Richards, 2002; Eq. 6.26) and the amplitude decay of infinite-frequency direct wave in a spherical Earth model from ray tracing. At distances close to the critical distance, *Pn* geometric spreading behaves like that of a conical head wave. As distance increases, *Pn* spreading starts to deviate from that of the head wave and at about 5°, *Pn* amplitudes begin to increase. In the range between the critical distance and about 10°, *Pn* evolves from a wave similar to a conical head wave to the interference head wave, which is a superposition of multiple waves reflected from the Moho. At teleseismic distances, the direct-wave spreading approaches that of the infinite-frequency diving P wave from ray tracing.

Pn geometric spreading in a spherical Earth model is not only different from that of a head wave as is shown in Figure 2, but also frequency dependent. Figure 3 shows the *Pn* amplitude-variation surface as a function of distance and frequency for the simple Base Earth Model. The strong frequency dependence of *Pn* amplitudes is apparent. Amplitudes at higher frequencies are affected more by sphericity than are lower-frequency amplitudes.

Approved for public release; distribution is unlimited.

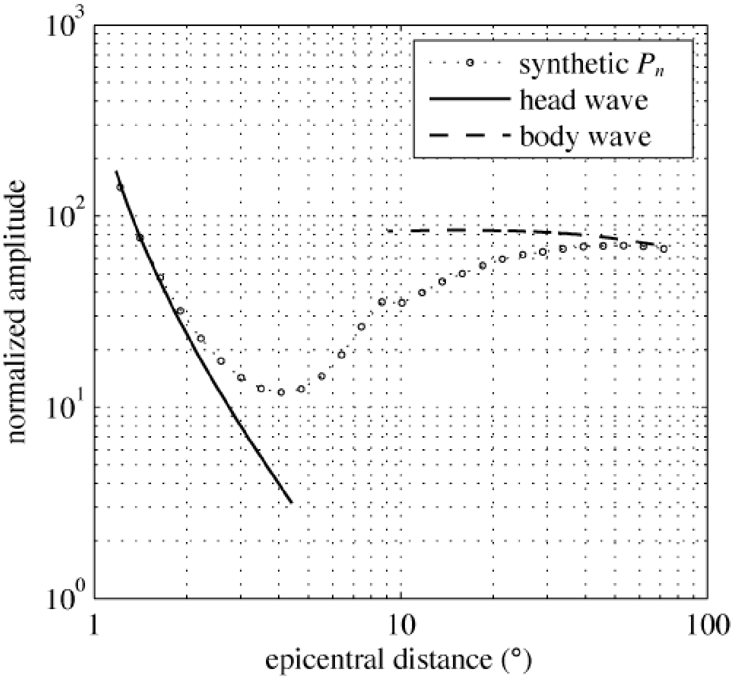

Figure 2. 10-Hz synthetic *Pn* amplitude decay in the spherical Base Earth Model with constant mantle velocities. The solid line depicts the theoretical amplitude decay of a conical head wave in a plane one-layer-over-half-space Earth model. The dashed line is the amplitude decay of infinite-frequency direct wave in a spherical homogeneous Earth model from ray-tracing calculations. From Yang et al. (2007).

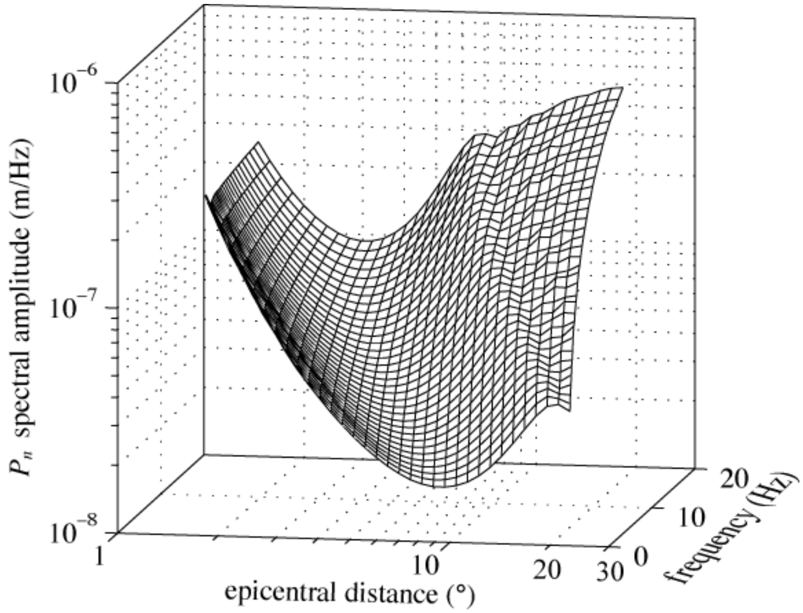

Figure 3. Synthetic *Pn* amplitudes as a function of epicentral distance and frequency. From Yang et al. (2007).

Yang et al. (2007) presented a parameterized description of *Pn* geometric spreading for this simple reference model. The amplitude spectrum of *Pn* can be parameterized as

$$A(r,\theta,f) = K(f)M_0R(\theta)G(r,f)\exp\left(-\frac{\pi f}{Q(f)v}r\right)S(f) \tag{1}$$

with the new geometric-spreading model expressed as

$$G(r,f) = \frac{10^{n_3(f)}}{r_0}\left(\frac{r_0}{r}\right)^{n_1(f)\log\left(\frac{r_0}{r}\right)+n_2(f)} \qquad (r_0 = 1\text{ km}) \tag{2}$$

and

$$n_i(f) = n_{i1}\left[\log\left(\frac{f}{f_0}\right)\right]^2 + n_{i2}\log\left(\frac{f}{f_0}\right) + n_{i3} (i = 1, 2, 3;\ f_0 = 1\text{ Hz}). \tag{3}$$

In Equation 1, K is a frequency-dependent scaling factor; M_0 is source moment; R is source radiation pattern; Q is *Pn* quality factor; v is *Pn* velocity; S is receiver site response; r is epicentral distance; θ is azimuth angle and f is frequency. r_0 and f_0 are included in Equations (2) and (3) in order for the new model to have the same dimension as standard power-law models (e.g., Street et al., 1975; Sereno et al., 1988). Yang et al. (2007) derived the coefficients n_{ij} by fitting Equations (2) and (3) to the synthetic data. As a result, the new spreading models better represent *Pn* and *Sn* geometric spreading in a more realistic Earth. The main differences between the new geometric-spreading model and the standard frequency-independent power-law model are the addition of the first term in the exponent and the frequency dependence of parameters n_i.

3.2 *Pn Spreading Sensitivity to Mantle Velocity Gradients*

The velocity structure of the mantle lid is seldom well constrained. The most direct constraint is provided by the shape of the *Pn* travel time curve as a function of distance over a wide-enough distance range for reliable measurement, and even when there is apparent travel time branch curvature, it is difficult to distinguish between a smooth gradient with depth versus constant velocity layering with small step increases. Receiver function methods and surface wave dispersion inversions sometimes indicate gradients in the lid structure, but resolution tends to be poor, especially for *P*-velocity. As a result, reference velocity structures often assume constant or near-constant velocity in the mantle lid by default, so the Base Earth Model is not a bad starting point in many cases. However, there are regions where the lid velocity appears to increase or decrease with depth. The effects of positive *P*-velocity gradients in the mantle lid on the frequency-dependent spreading of *Pn* are illustrated in Figure 4. The basic shape of the spreading behavior is preserved, but the distance-behavior shifts systematically to shorter distances, with overall higher *Pn* amplitudes as the gradient increases. It is possible to determine appropriate coefficients for a spreading representation like Equation (2) for any specific gradient, but this is only warranted if there are a priori constraints on the specific model in the region for which the spreading is to be utilized.

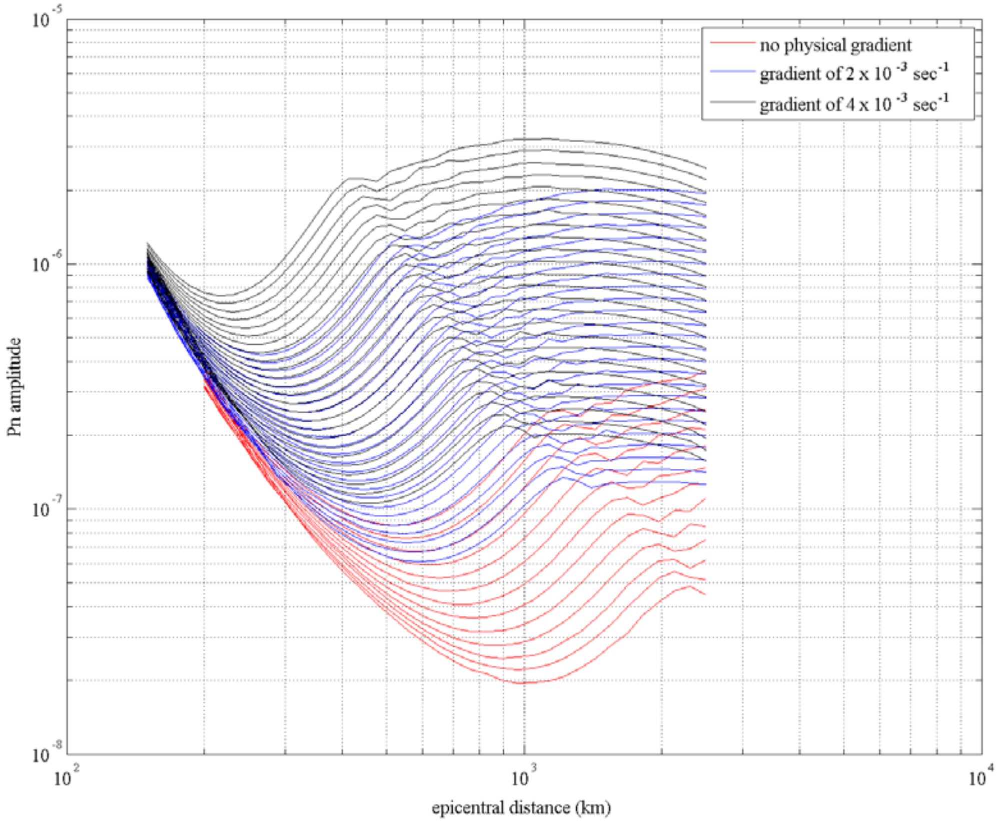

Figure 4. *Pn* amplitude versus distance curves similar to Figure 3, but for the Base Earth Model (red curves, for no physical gradient in the lid) and for two models with mild positive gradients in the mantle lid. The suite of curves for each case corresponds to frequencies ranging from 0.75 Hz (lowest curve) to 12 Hz (highest curve). From Avants et al. (2011).

3.3 *Pn Spreading Sensitivity to Lateral Mantle Velocity Volumetric Heterogeneity*

In Avants et al. (2011), we explored the effects of lateral heterogeneity in the mantle lid velocity structure on *Pn* spreading using a 2D fourth-order finite-difference code (Xie and Lay, 1994). We included random lateral volumetric velocity fluctuations characterized by RMS velocity and varying horizontal and vertical averaging functions with different length scales in the Model. This allowed us to consider 2D random heterogeneity models like those shown in Figure 5.

Approved for public release; distribution is unlimited.

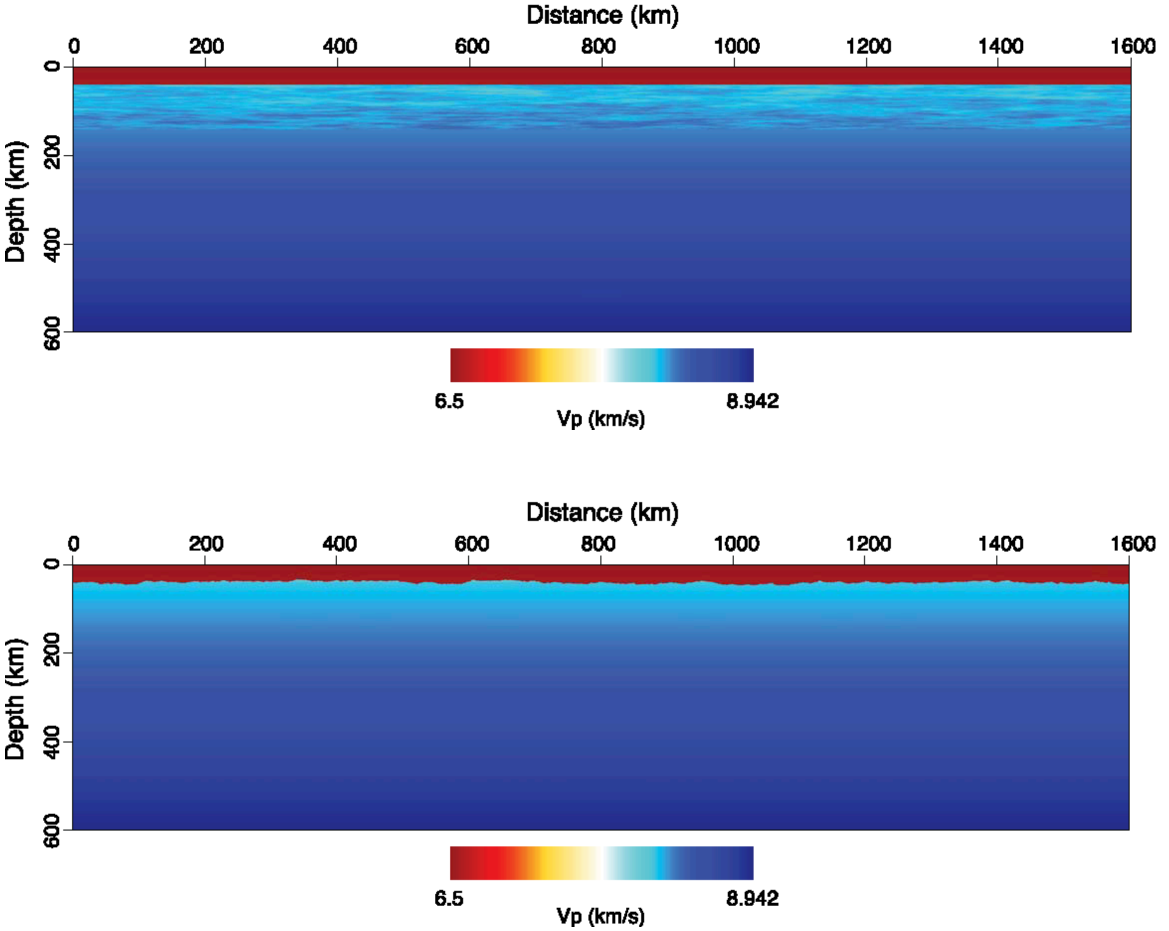

Figure 5. Visualizations of 2D velocity model with (top) 0.5% (rms) *P*-velocity heterogeneity in the upper one hundred kilometers of the mantle lid, and (bottom) exponential 3% (rms) roughness of the Moho with 40 km scale averaging length. The background model is the EFT version of the Base Earth Model, so there is a slight positive velocity gradient across the crust and mantle. From Avants et al. (2011).

The 2D finite-different modeling approach used at that time could not achieve the very high frequencies of the 1D wave-number integration method, so the synthetics are limited to about 1 sec dominant period. Analysis of effects of random heterogeneity requires a statistical sampling of the effects associated with different realizations of the random velocity parameters. Many models have been run for various statistical properties of the mantle lid structure, with complete synthetic seismograms being computed.

Figure 6 shows the synthetic ~1 Hz *Pn* amplitudes for ensemble averages of 5 realizations each for variable heterogeneity aspect ratios and rms velocity fluctuations for structures like that at the top in Figure 5, directly compared to the result for the Base Earth Model.

Approved for public release; distribution is unlimited.

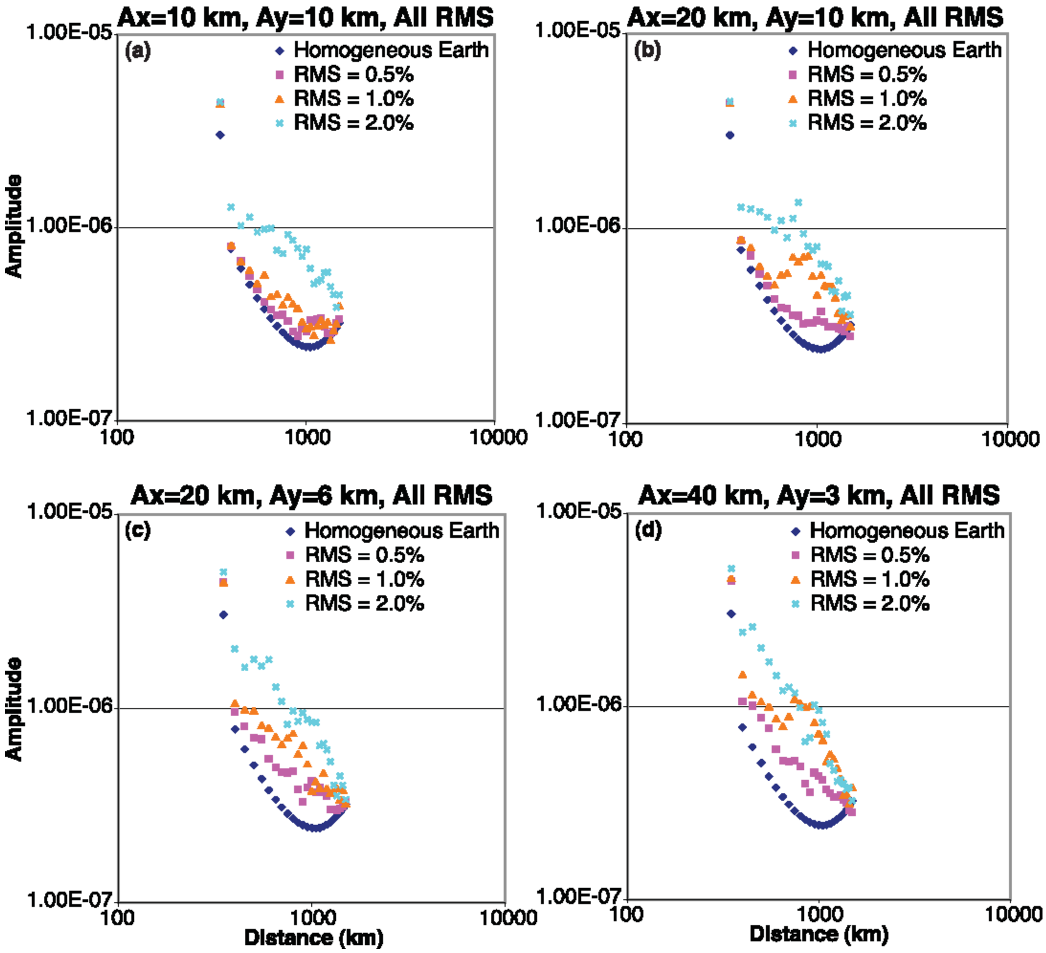

Figure 6. Ensemble-averaged ~1-Hz *Pn* amplitudes as a function of distance for all configurations of random volumetric mantle heterogeneity simulated. *Pn* amplitude for the BEM (diamonds) are compared to models with 0.5% RMS (squares), 1.0% RMS (triangles), and 2% RMS (X's) Vp fluctuation for horizontal (Ax) and vertical (Ay) averaging lengths of (a) Ax = 10 km, Ay = 10 km (isotropic); (b) Ax = 20 km, Ay = 10 km; (c) Ax = 20 km, Ay = 6 km; and (d) Ax = 40 km, Ay = 3 km. Each value is the average of 5 realizations with different seed kernels.

An interesting behavior in Figure 6 is that the presence of velocity fluctuations affects the basic shape of the spreading, and in some cases it could be represented well by a power-law type behavior at this frequency (~ 1 Hz). This suggests that the 1D spreading behavior is rather delicate, with heterogeneity disrupting the specific interference that gives rise to the complex shape. As the strength of the velocity functions increases, there is progressive reduction of curvature of the amplitude-distance trend, and the overall amplitude behavior becomes increasingly power-law like. We emphasize that these simulations are 2D, are very band-limited so any frequency dependencies are not defined, and have prescribed velocity heterogeneity spectra. Whether they represent, or even approach the prevailing situation in the mantle lid is an open question and constraints can only come from observed data. In addition, more accurate modeling will require

Approved for public release; distribution is unlimited.

broadband 2D and 3D simulations. Nevertheless, the results demonstrate the effects of strong velocity heterogeneity on *Pn* geometric spreading.

3.4 *Pn Spreading Sensitivity to Lateral Moho Topography*

While volumetric heterogeneity is expected to result from geological processes during crustal formation and evolution, the same is true for Moho irregularities on multiple scales. *Pn* and *Sn* interactions with the Moho near the source and receiver as well as throughout the propagation and whispering gallery development provide sensitivity to the Moho roughness. Avants et al. (2011) parameterized 2D exponential (Figure 5) and Gaussian statistical irregularities in the Moho depth to explore the effects of random structures, along with simple step-like structure in the Moho.

The exponential model is much richer in small-scale structure and produces longer enduring coda than the smoother Gaussian model, but the overall behavior of the models is similar for the 1 sec dominant period (Figure 7). For an 80 km horizontal averaging function the amplitude decay effects become significant for 5% RMS heterogeneity in the depth of the Moho. There is only minor sensitivity to the choice of horizontal averaging function for values larger than 40 km for a given statistical model.

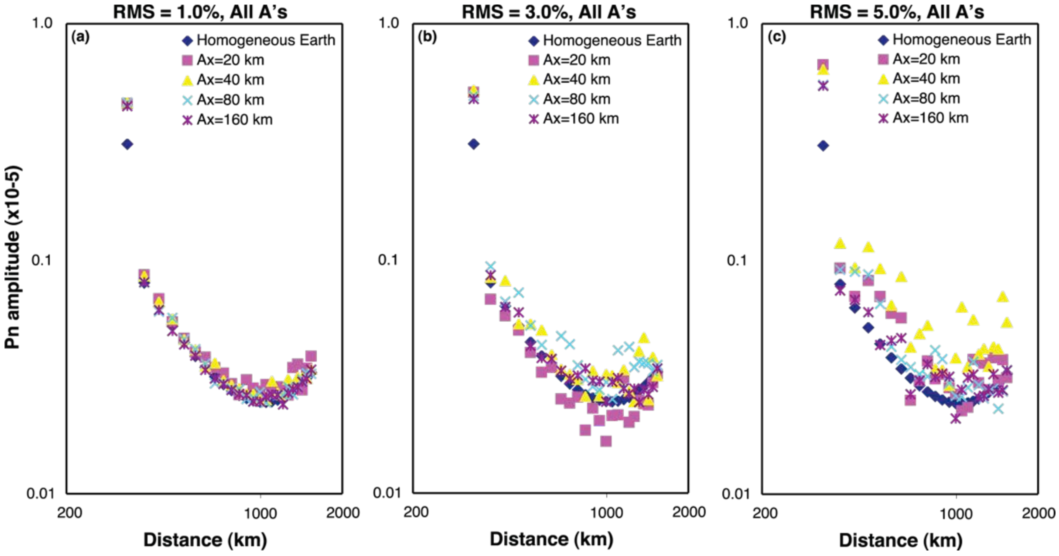

Figure 7. Ensemble-averaged ~1-Hz *Pn* amplitudes plotted as a function of distance for all configurations of random Moho topography heterogeneity, grouped by percent RMS depth fluctuation. *Pn* amplitude for the BEM (diamonds) are compared to horizontal averaging length scales of 20 km (squares), 40 km (triangles), 80 km (X's), and 160 km (asterisks), for percent RMS depth fluctuations of (a) 1%; (b) 3%; and (c) 5%. From Avants et al. (2011).

3.5 *Pn Spreading Model Constrained with Observed Data*

Yang (2011) evaluated the performance of Equation (2) in correcting observed *Pn* amplitudes in Asia. Figure 8 shows the 1-Hz *Pn* amplitudes after source and geometric-

Approved for public release; distribution is unlimited.

spreading correction using Equation (2). The figure shows that Equation (2) provides good spreading correction (leaving a linear trend in log amplitude versus distance) only over a limited distance range between about 860 and 1400 km. Outside this range, corrected amplitudes exhibit undesirable variations (flattening and roughness) relative to a constant decay rate that could be expected for average attenuation of *Pn*.

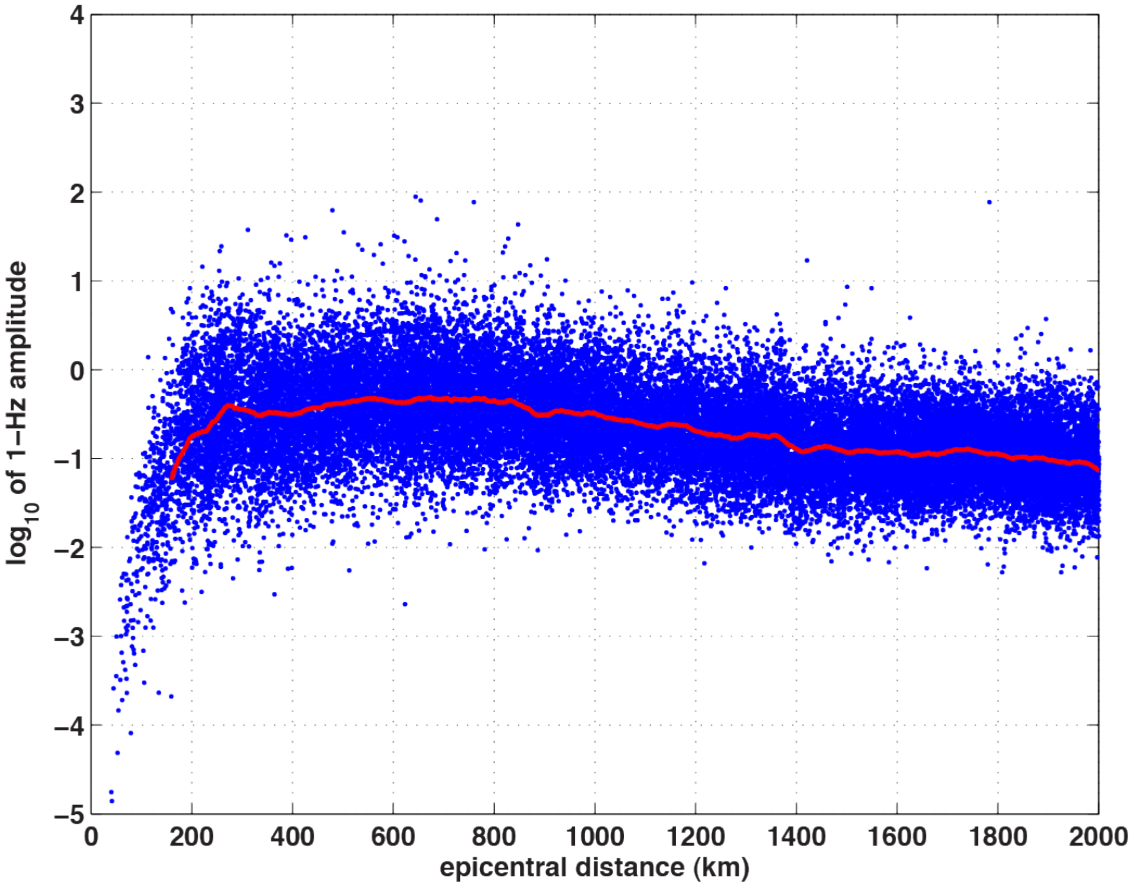

Figure 8. 1-Hz *Pn* amplitudes after source and geometric-spreading correction using the model developed by Yang et al. (2007). The red line is the 400-point moving average showing the decay trend of the data.

To better represent *Pn* spreading, Yang (2011) developed a method to construct observation-based and region-specific *Pn* spreading models. In his method, the average *Pn* *Q* at different frequencies is calculated from source and spreading (using Equation (2)) corrected *Pn* amplitudes. These *Q* values are then used to correct raw *Pn* amplitudes for attenuation. The resulting amplitude residuals are then fit with an observation-constrained spreading model. The *Pn* spreading model that Yang (2011) developed for Asia performs much better, resulting in a set of spreading-corrected amplitudes that have a constant distance decay slope for a wide distance range from 150 km to 1600 km (Figure 9).

Approved for public release; distribution is unlimited.

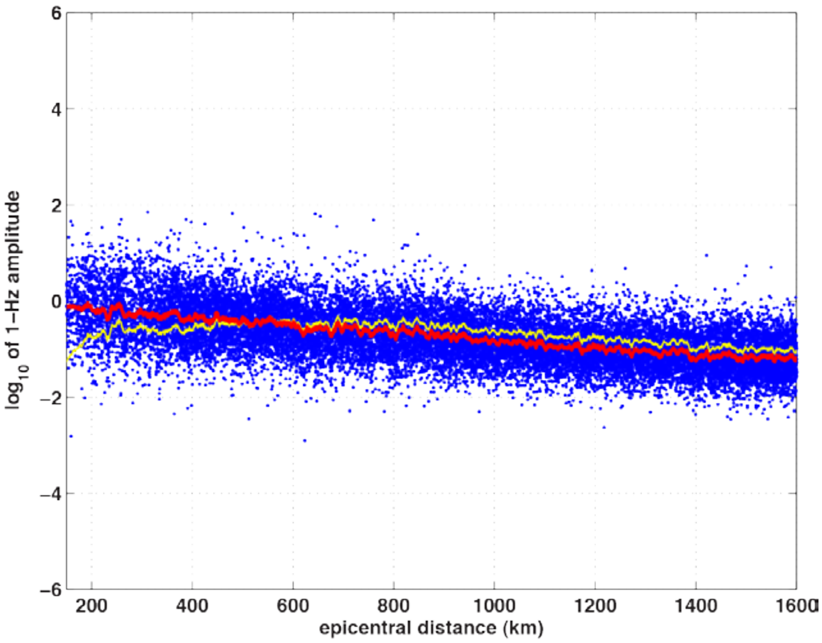

Figure 9. 1-Hz *Pn* amplitudes after source and geometric-spreading correction using the new model developed by Yang (2011). The red line is the 400-point moving average showing the decay trend of the data. The yellow line is the same as the red line in Figure 8.

3.6 *The Effect of Geometric Spreading on Attenuation Determination*

The tradeoff between geometric-spreading and attenuation makes it difficult to accurately estimate one parameter if the other parameter is not well constrained. The problem is particularly acute for *Pn* and *Sn* due to reasons discussed above. As a result, an accurate spreading relationship must be estimated, even for individual paths, in order to develop reliable 2D attenuation models used in amplitude corrections for discrimination and yield estimation.

To demonstrate the advantage and utility of a physics-based spreading model over traditional power-law model, Figure 10 compares the measured 1-Hz *Pn* amplitudes with the spreading model of Yang et al. (2007) and a power-law model. The figure shows that the Yang et al. (2007) model has a consistently slower decay rate than the data toward long distances, which is desirable if progressive attenuation occurs to produce the data trend over a large range of distance (yellow line). The power-law model, on the other hand, decays faster than the data toward long distances, which would result in a negative *Q* when trying to match the data behavior.

Figure 11 demonstrates this, showing examples of *Q* estimates obtained using either the model of Yang et al. (2007) or the power-law model for multiple frequencies. The model of Yang et al. (2007) yields reasonable *Q* values at all frequencies whereas using the power-law model results in either negative or extremely large *Q* values. These examples show that even though the model of Yang et al. (2007) is not optimal, it provides better spreading corrections, due to its physics basis, than a power-law model, which corresponds to no known Earth structure.

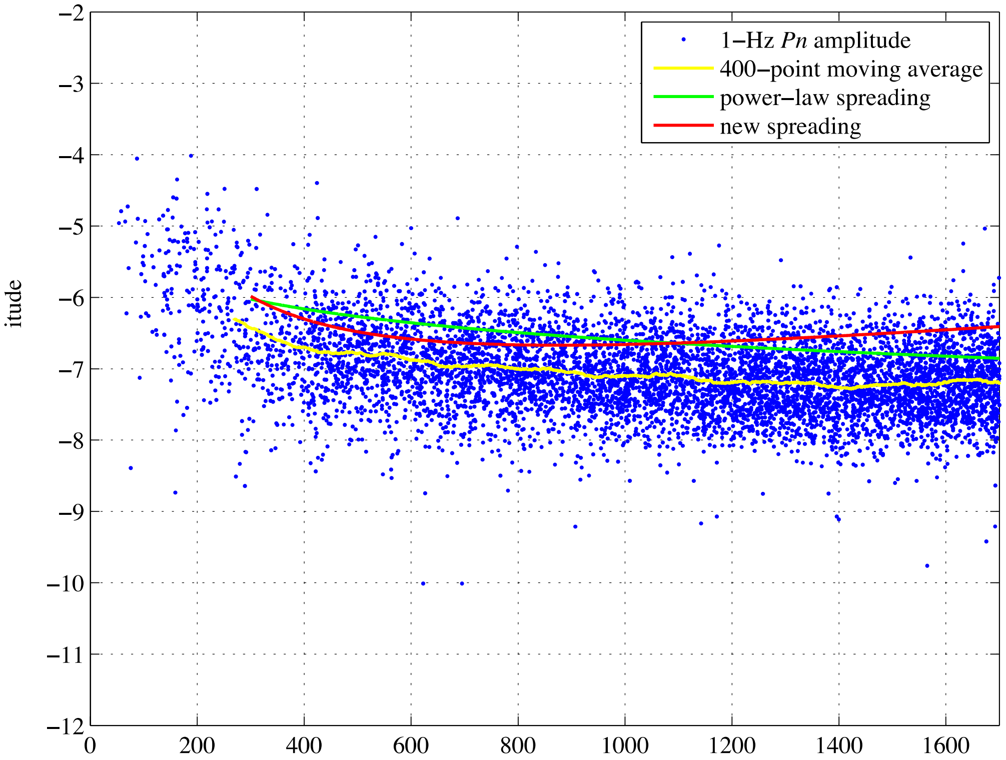

Figure 10. Comparison of 1-Hz *Pn* amplitude decay with decays predicted by a power-law spreading model and by the new spreading model of Yang *et al.* (2007). The yellow line is the 400-point moving average of the *Pn* data points to more-clearly delineate the amplitude-decay trend.

The foregoing review of accomplishments and enhanced understanding of geometric spreading for *Pn* (all attributes hold for *Sn* as well) indicates that reliable models of attenuation can be obtained only if reliable geometric spreading is computed for specific regional structure. Thus, a strategy for determining regional structures with observationally-constrained mantle-lid velocity gradients is needed.

The strategy of regional seismic travel time (RSTT) model parameterization advanced by Myers et al. (2010) adopts a geographic node description of crustal and upper mantle models, where the mantle portion is parameterized by a linear P-wave velocity gradient. This parameterization is very similar to that of the Base Earth Model used in the *Pn* and *Sn* geometric spreading calculations of Yang et al. (2007) and Avants et al. (2011) (Figure 12). Myers et al. (2010) used regional *Pn* travel times to develop a tomographic model of *Pn* velocity variation and mantle-gradient variation in the mantle lid (Figure 13). While the parameterization is not explicitly intended to predict amplitude behavior, nor are the resulting velocity models believed to be accurate in each case, the models can be used as a starting point to explore amplitude behavior.

Approved for public release; distribution is unlimited.

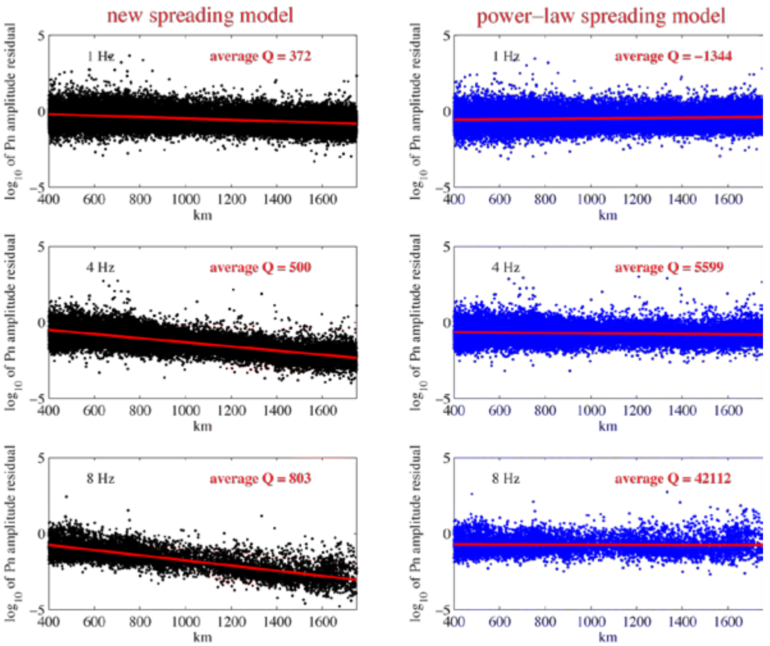

Figure 11. Comparison of average Q estimates from *Pn* amplitudes corrected for source and geometric-spreading effects using different spreading models. Q estimates at 1, 4 and 8 Hz are compared.

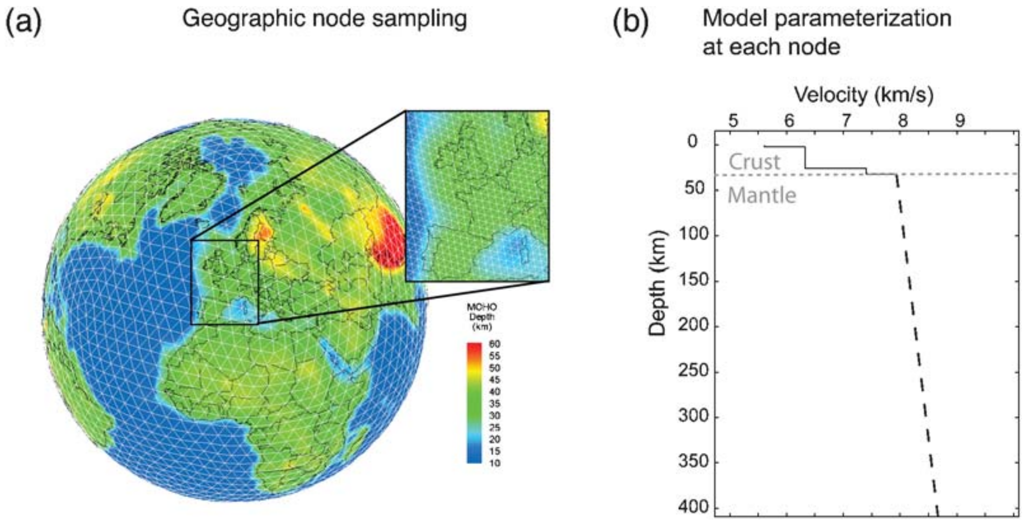

Figure 12. Global model parameterization. (a) An example tessellation with approximately 5° grid spacing. The inset shows the 1° used in the study by Myers et al. (2010). Color indicates Moho depth of the starting model. (b) An example velocity vs. depth profile as defined at each node. The mantle portion of the profile is specified by the velocity at the crust/mantle interface and a linear gradient. From Myers et al. (2010).

Regional phase arrival times were used by Myers et al. (2010) to develop a tomographic model (Figure 13) for variation in velocity of the uppermost mantle and variation in the strength of the mantle gradient. This provides regional models that fit

Approved for public release; distribution is unlimited.

travel times, but the precision of the velocity gradients in the mantle is impacted by scatter in the data, averaging of nodes in a given region, and lack of resolution of curvature of *Pn* travel times. While the parameterization is not explicitly intended to predict amplitude behavior, the models can be used to do so.

We examine RSTT derived models and associated travel time data, with corresponding regional phase amplitude measures as a function of frequency to evaluate use of travel time models as first-order structures for computing regional geometric spreading corrections (thereby having unified model frameworks for travel time and amplitudes), and as a starting point for revision of the models guided by observed amplitude behavior that is not well matched.

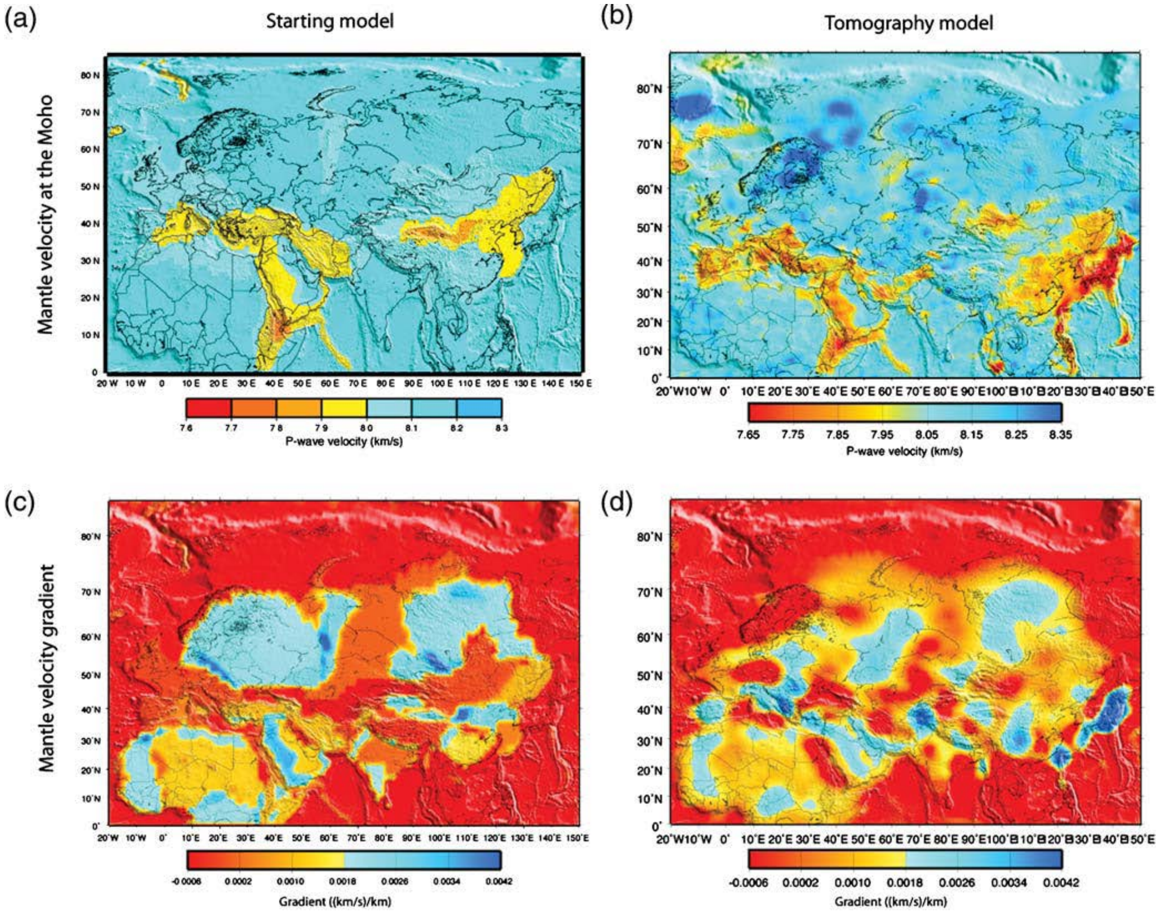

Figure 13. Comparison of starting and RSTT models. (a) Velocity below the Moho for starting model and (b) RSTT model. (c) Mantle gradient (km/sec/km) for starting model and (d) RSTT model. From Myers et al. (2010).

4. RESULTS

Building on the back-ground results discussed above from an earlier contract, we have performed additional forward modeling of Pn geometric spreading in various 1D and 2D structures, analyzed regional variations in Pn around the North Korean test site and modeled effects of oceanic path segments, and explored the RSTT models and empirical spreading correction approach for Eurasia, as discussed in this section.

4.1 *One-Dimensional Velocity Models*

To simulate Pn-wave propagation, a set of 1D and 2D velocity models with different velocity gradients were designed. These models are illustrated in Figures 14 and 15. All model parameters shown are functions of radius before earth flattening transformation (EFT). A constant-velocity lid model (Const-Lid) is shown in Figure 14 and listed in Table 1. For comparison, we also calculated Pn propagation in the Const-Lid model without applying the EFT (Const-Lid w/o EFT). A velocity model with lid radial gradient of $1\times10^{-3}\,\text{sec}^{-1}$ (Gradient-0.001) is shown in Figure 14 and described in Table 2. Velocity models with $0\times10^{-3}\,\text{sec}^{-1}$ and $2\times10^{-3}\,\text{sec}^{-1}$ gradients (Gradient-0.000 and Gradient-0.002) are obtained similarly. These models connect to a steep IASP-91 gradient at greater depth.

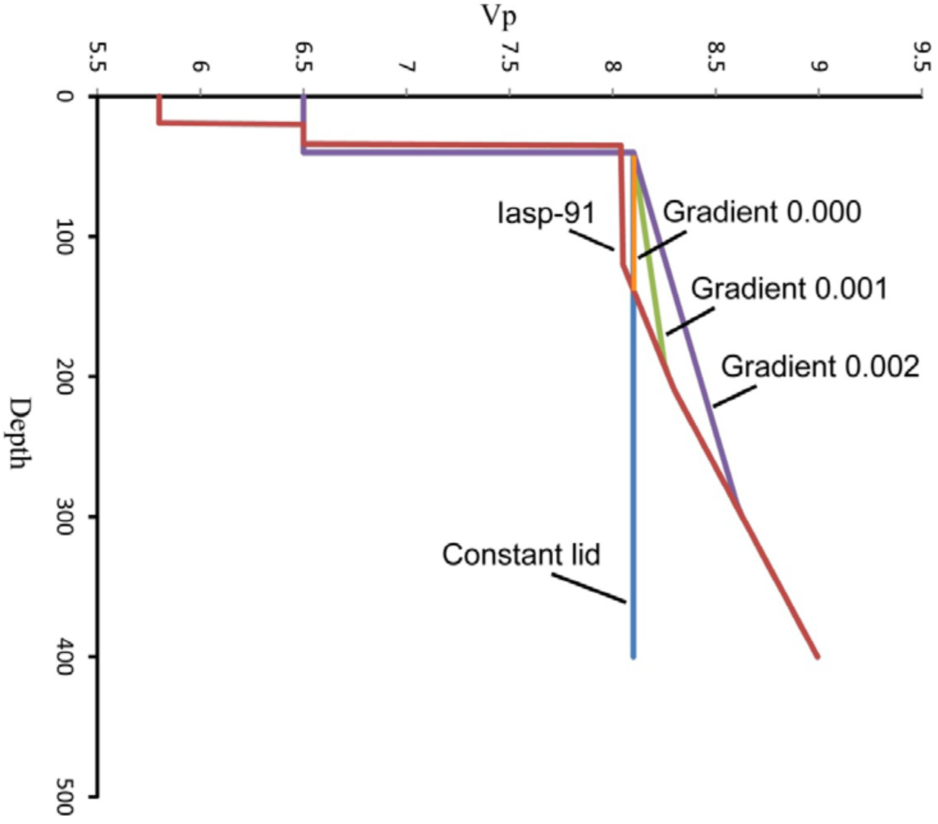

Figure 14. One-dimensional velocity models used for Pn computation. The structures are spherical models prior to Earth Flattening Transform (EFT).

Approved for public release; distribution is unlimited.

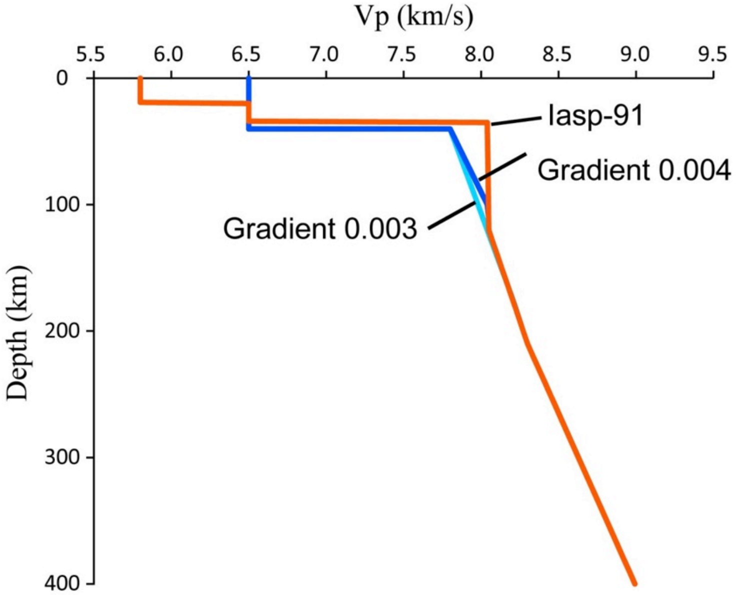

Figure 15. Velocity models for Gradient-0.003 and Gradient-0.004. Note, here the P-velocity beneath the Moho is 7.8 km/s, so that the strong positive gradients do not lead to un-physically high P velocities.

Table 1. Constant velocity lid model, Const-Lid (radial parameters before EFT)

	Depth of the layer	Vp (km/s)	Vs (km/s)	ρ (g cm^{-3})
crust	40 km	6.5	3.75	2.7
mantle	infinity	8.1	4.45	3.32

Table 2. Velocity model with $1\times10^{-3}\,\text{sec}^{-1}$ gradient, Gradient-0.001 (radius parameters before EFT)

		Vp (km/s)	Vs (km/s)	ρ (g/cm^3)
crust	40 km	6.5	3.75	2.7
mantle		Starting from 8.1 km/s below Moho, increasing with a $1\times10^{-3}\,\text{sec}^{-1}$ gradient until reach to a depth where Vp has the same values as model IASP-91 thereafter.	Converted from Vp adopting Vp/Vs values in IASP-91	From PREM

Approved for public release; distribution is unlimited.

4.2. Laterally Varying Velocity Models

Velocity models with laterally varying velocity gradients are used for testing Pn-wave propagation in these environments. These models are composed of two sections with different gradients. One section from 0 – 450 km, another from 550 km – 1000 km. Between them, from 450 km – 550 km, the linear interpolation is used. These velocity models include:

Gradient-0.000-0.001 (velocity gradient varies from $0\times10^{-3}\,\mathrm{sec}^{-1}$ to $1\times10^{-3}\,\mathrm{sec}^{-1}$), Gradient-0.001-0.000 (velocity gradient varies from $1\times10^{-3}\,\mathrm{sec}^{-1}$ to $0\times10^{-3}\,\mathrm{sec}^{-1}$), Gradient-0.000-0.002 (velocity gradient varies from $0\times10^{-3}\,\mathrm{sec}^{-1}$ to $2\times10^{-3}\,\mathrm{sec}^{-1}$), Gradient-0.002-0.000 (velocity gradient varies from $2\times10^{-3}\,\mathrm{sec}^{-1}$ to $0\times10^{-3}\,\mathrm{sec}^{-1}$).
Figure 16 shows displays of these models relative to model Gradient-0.000.

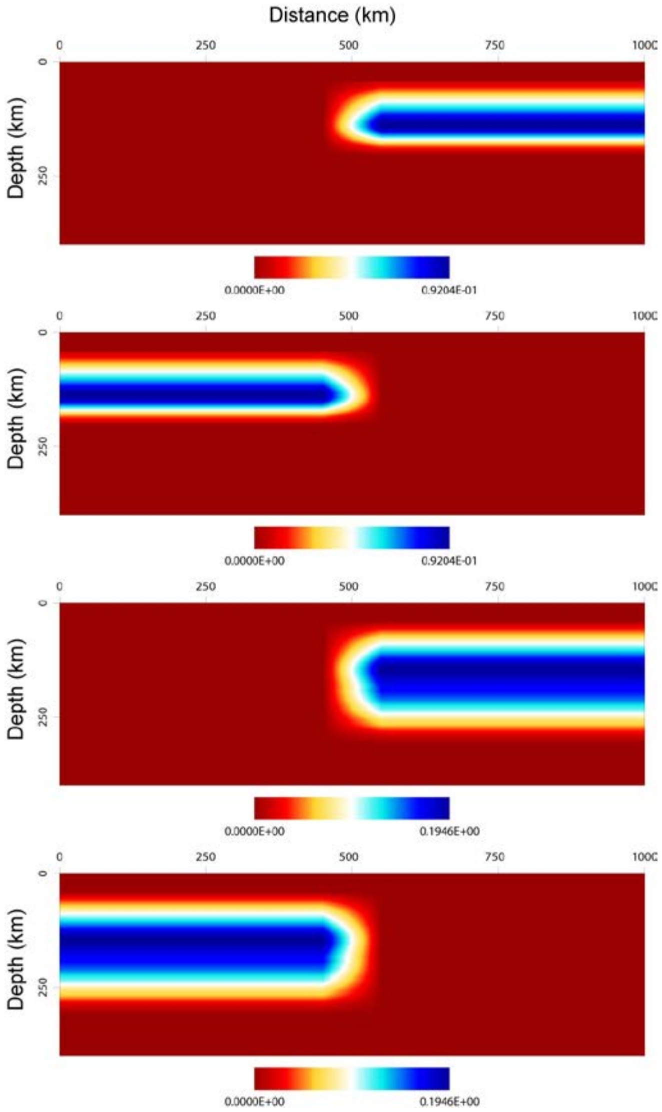

Figure 16. Laterally varying velocity models. Shown here are gradient models subtracting Gradient-0.000. From top to bottom are for Gradient-0.000-0.001, Gradient-0.001-0.000, Gradient-0.000-0.002, and Gradient-0.002-0.000, respectively.

4.3 *Pn Simulations for 1D Velocity Models*

Extending the bandwidth of finite-difference calculations for large-distance Pn synthetics was one of our initial priorities. The fourth-order code used by Avants et al. (2011) was adapted to and tested on our cluster, and stable P-SV and SH calculations were achieved for ranges of up to 1000 km and frequencies up to 10 Hz, for models with a flat free-surface and laterally varying structure, either with or without small-scale statistical heterogeneity being included. This enabled examination of Pn geometric spreading behavior in laterally varying 2D structure over broader bandwidth than in prior work. Table 3 indicated parameters used in the finite-difference calculations.

Table 3. Parameters used for FD calculations

Model size (horizontal)	1000 km
Model size (Vertical)	400 km
dx	0.05 km
dz	0.05 km
grid size	20003 x 8003
dt	3.5 ms
elapsed time	145 sec.
time steps	41488
Source depth	15 km
Type of source	Explosion source

Figure 17 shows wavefield snapshots for the 1D structure Const-Lid w/o EFT out to ranges of 900 km. In this case there is no induced positive velocity gradient from the earth-flattening, so the model is the classic constant velocity layered structure that gives rise to a true head wave with Pn amplitude decay following the solid line in Figure 2. The wavefield behavior is quite different when the EFT is included, as seen in Figure 18. The Pn amplitudes are now significantly higher at large range. This corresponds to the basic behavior described in the previous section, with turning ray behavior of the multiples in the lid modifying the geometric spreading of the first arrival. Increasing the positive gradients beyond the mild gradient from EFT further increases the Pn amplitudes, as shown in the snapshots for model Gradient-0.001 shown in Figure 19 and for model Gradient-0.002 in Figure 20. Figure 21 compares the waveforms for these four models at a time lapse of 120 s. The amplitude normalization is the same for all four models so that amplitudes are directly comparable. Note the strengthening of the Pn amplitudes proportional to velocity gradient and the clear development of underside reflections from the Moho as the gradient increases. These calculations replicate the findings from our earlier project, but extend the frequency band of the finite-difference calculations to about 10 Hz for distances of 1000 km, as had only been achieved with frequency-wavenumber integration previously. This enables exploration of high frequency Pn geometric spreading behavior in 2D models for the first time.

Approved for public release; distribution is unlimited.

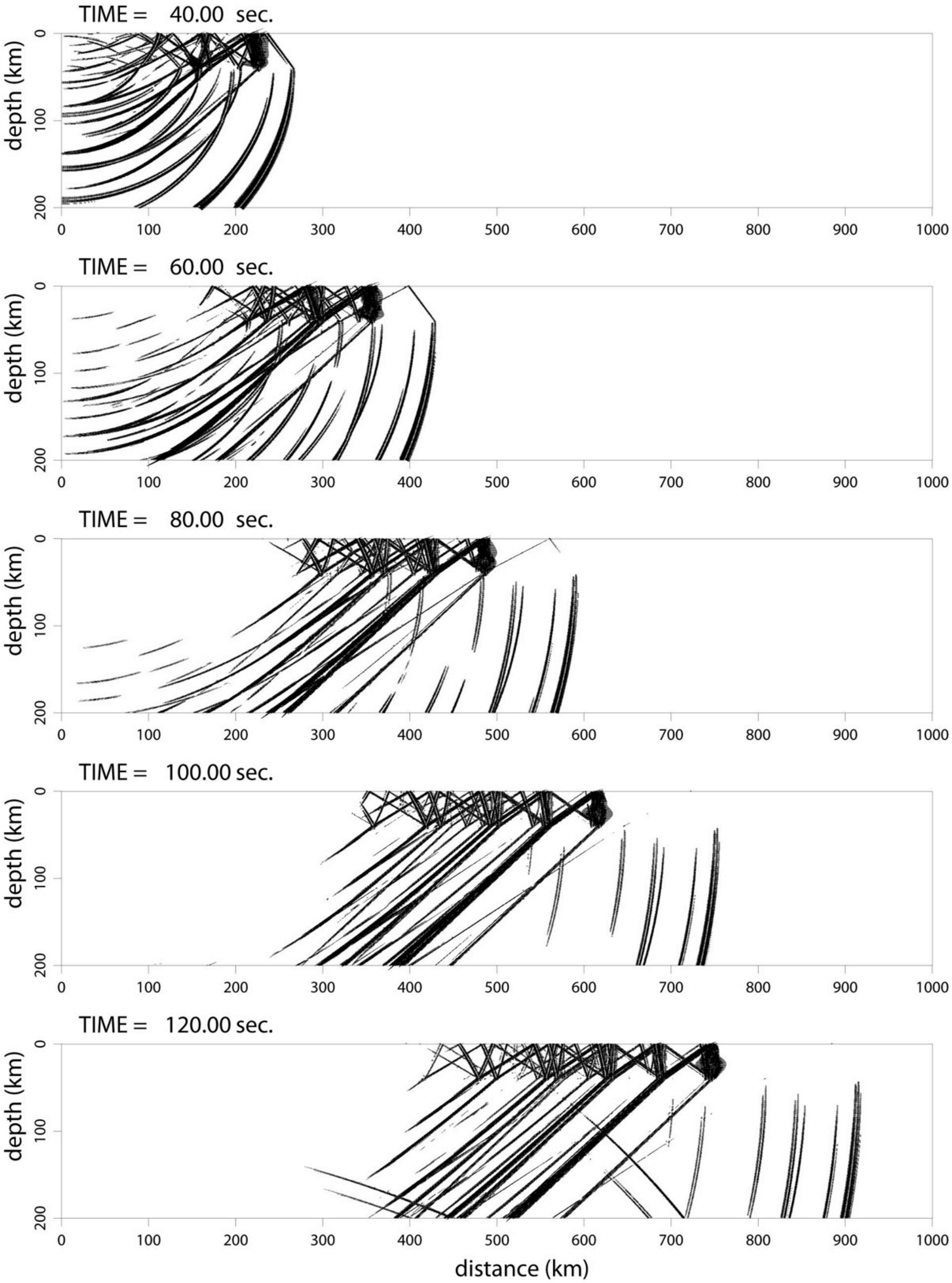

Figure 17. Snapshots of Pn waves propagating in the Const-Lid w/o EFT model using the enhanced 2D finite-difference code implementation.

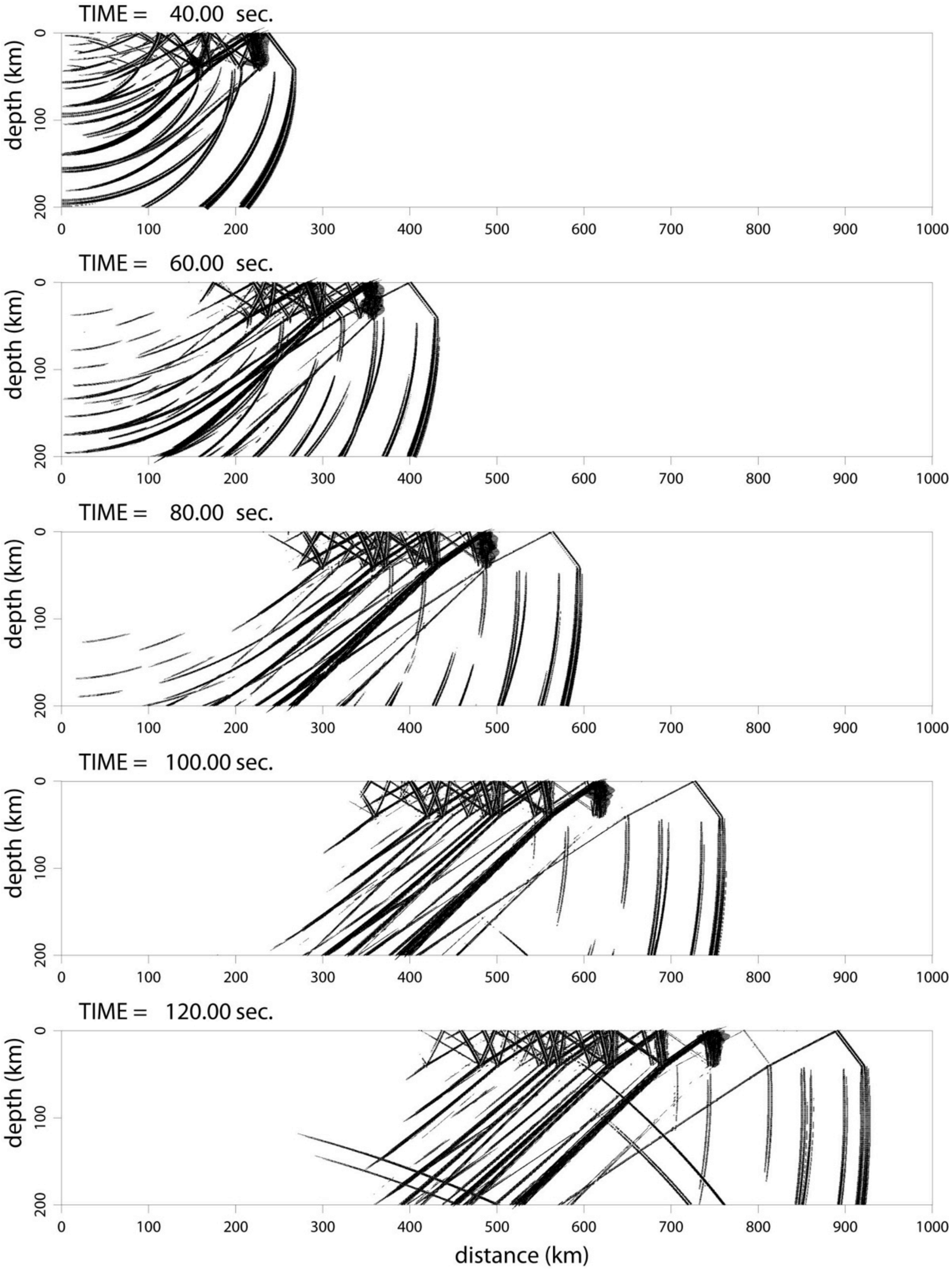

Figure 18. Snapshots of Pn waves propagating in the Const-Lid model. Note the enhanced Pn amplitude resulting from the positive velocity gradients from the EFT (compare to Figure 17).

Approved for public release; distribution is unlimited.

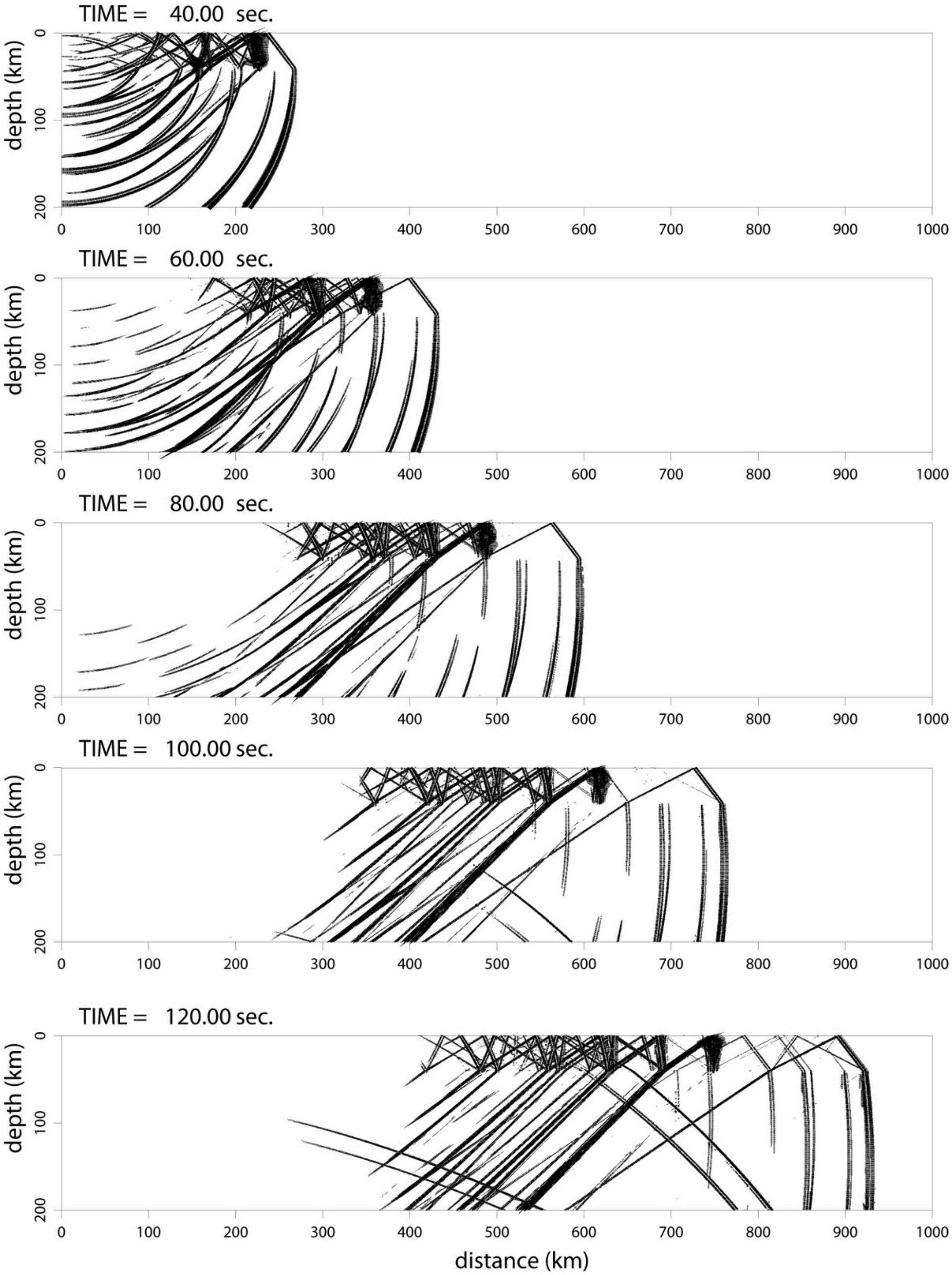

Figure 19. Snapshots of Pn waves propagating in velocity model Gradient-0.001 with $1\times10^{-3}\,\text{sec}^{-1}$ velocity gradient in the upper mantle.

Approved for public release; distribution is unlimited.

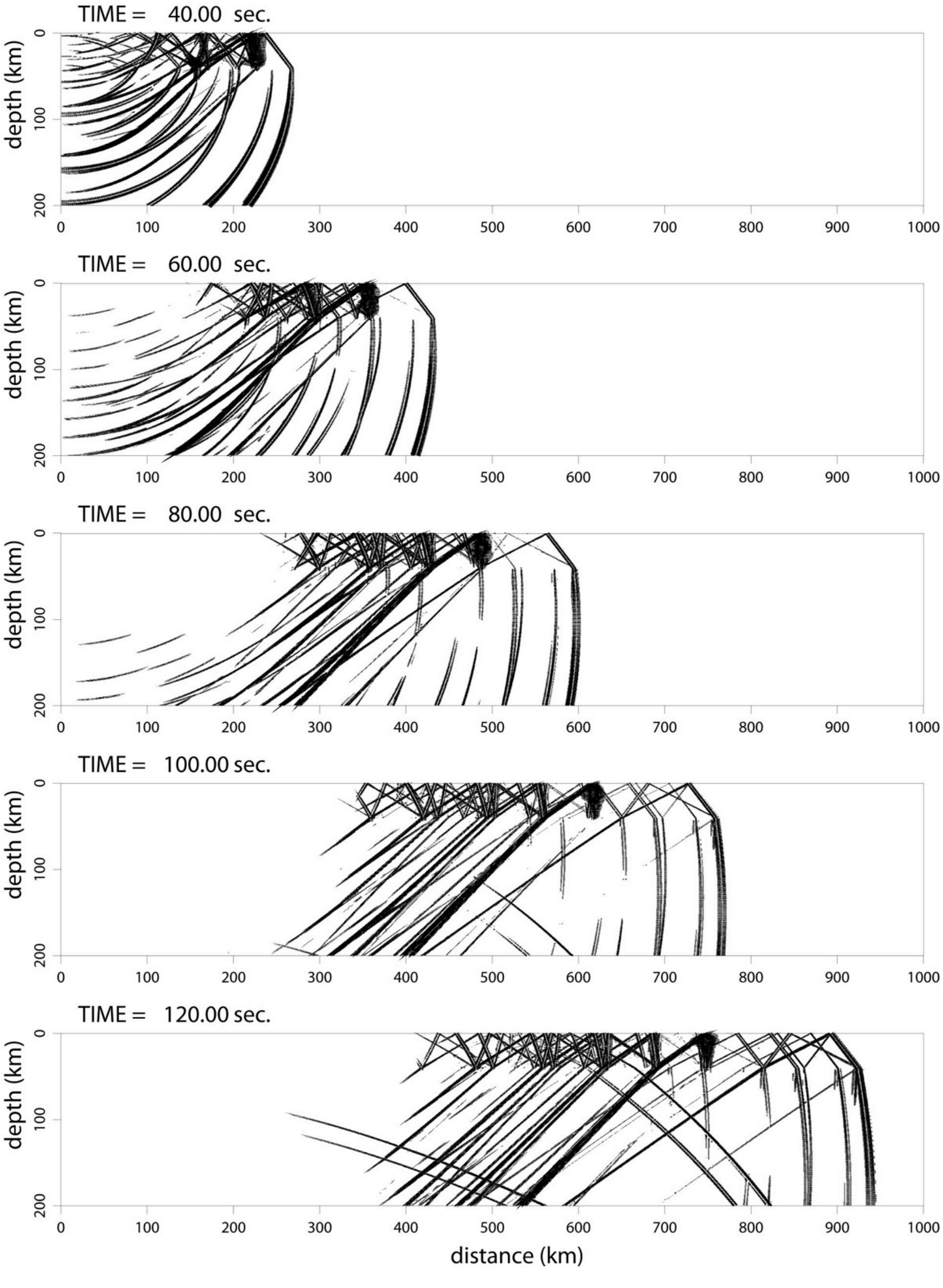

Figure 20. Snapshots of Pn waves propagating in velocity model Gradient-0.002 with $2\times10^{-3}\,\mathrm{sec}^{-1}$ velocity gradient in the upper mantle.

Approved for public release; distribution is unlimited.

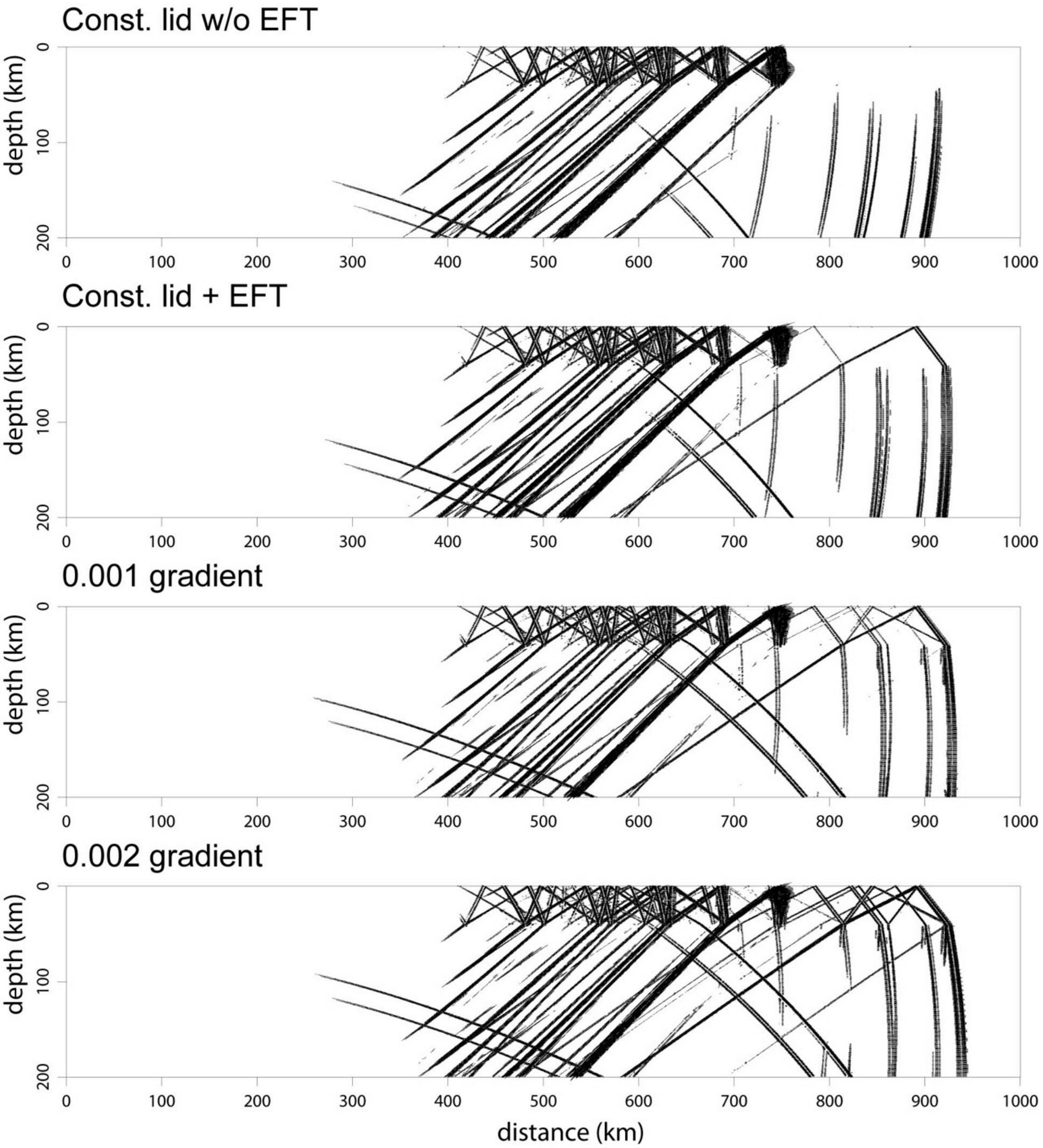

Figure 21. Comparison between snapshots in models with different velocity gradients (t = 120 sec). For easy comparison, the same normalization factors are used for all models. From top to bottom are snapshots in model Const-Lid w/o EFT, Const-Lid, Gradient-0.001 and Gradient-0.002, respectively. Note the different Pn amplitude and different mantle P-wave wavefront expansion. In models with large gradient, the wave front bouncing from the bottom of the Moho can be seen.

Figure 22 shows amplitudes of the Pn arrivals for the same four models in reduced-velocity (8.1 km/s) distance profiles. The amplitudes for the two Const-Lid models are enhanced by a factor of 3 relative to those in Gradient models. The increase in Pn amplitude with increasing range and earlier arrival Pn arrival for the Gradient-0.001 and Gradient-0.002 models demonstrates the curvature of the geometric spreading curve seen in Figure 4.

Approved for public release; distribution is unlimited.

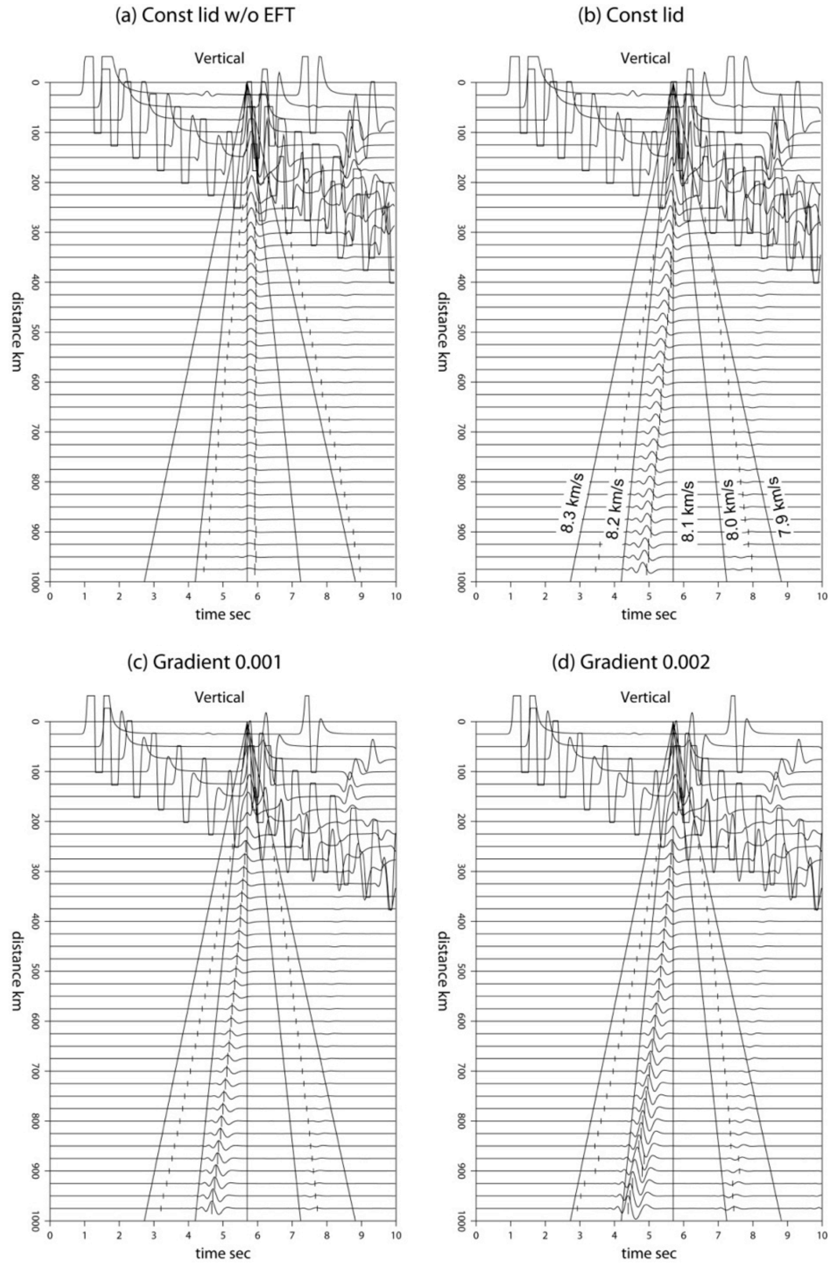

Figure 22. Comparison between Pn waves calculated in various 1D velocity models, with amplification factors used in (a) and (b) being 3 times those used for (c) and (d). As references, the solid lines are group velocities of 8.3, 8.2, 8.1, 8.0 and 7.9 km/s. The center mark indicates the picked arrival time and the two short marks indicate the sampling windows for Pn amplitude calculation. However, the synthetic data are quite different from the real data. The synthetics are more impulsive, while the real data are more like wave trains. A reduced time t-r/8.1 is used for horizontal coordinate.

For even stronger positive gradients, as in models Gradient-0.003 and Gradient-0.004, the Pn amplitude and waveform continue to change and the sub-Moho multiples become increasingly apparent. This is shown by the waveform profiles in Figure 23.

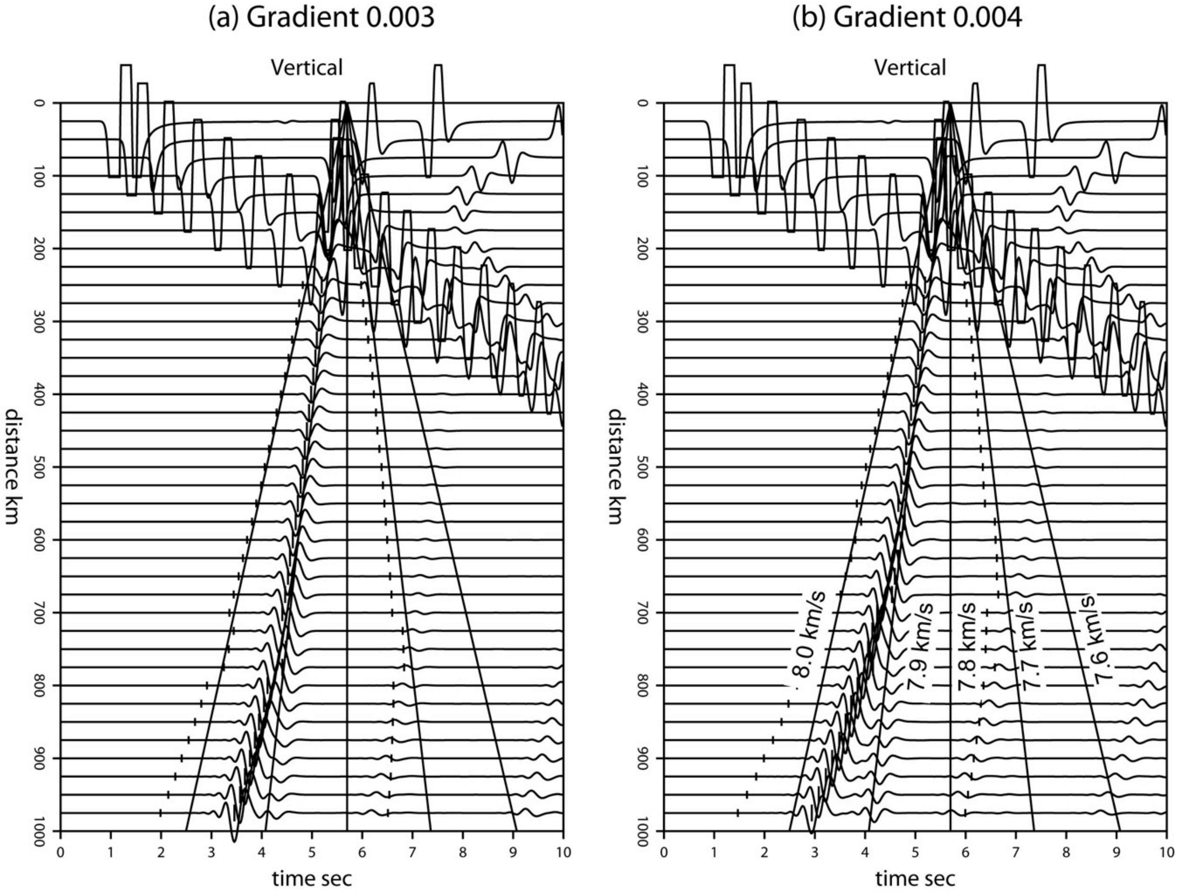

Figure 23. Comparison between Pn waves calculated in velocity models Gradient-0.003 and Gradient-0.004. Note, due to the slow upper mantle P-wave velocity (7.8 km/s below the Moho), the Pn velocity is low. For reference, the solid lines are group velocities of 8.0, 7.9, 7.8, 7.7 and 7.6 km/s. A reduced time t-r/7.8 is used for the horizontal coordinate.

Figure 24 shows Pn arrival time picks for broadband synthetics for 4 of the models. In the Const-Lid w/o EFT, the Pn arrival time has almost constant move-out. For the 3 models with positive gradients, including the contribution from the EFT, Pn arrives with higher apparent velocity at larger distances (also refer to the waveform figures and group velocity lines in Figure 22). These arrival times are picked using a very simple method and no frequency filter is applied. Slightly different arrival time picks will be made for different passbands. The travel times also include a time shift from the source time function in the synthetics. This figure demonstrates that the travel time variations from varying lid velocity gradients can be observed, and if a 1D velocity model with lithospheric positive velocity gradient is appropriate for a given region, it could be

Approved for public release; distribution is unlimited.

constrained by travel times and used to develop self-consistent geometric spreading curves for Pn and Sn.

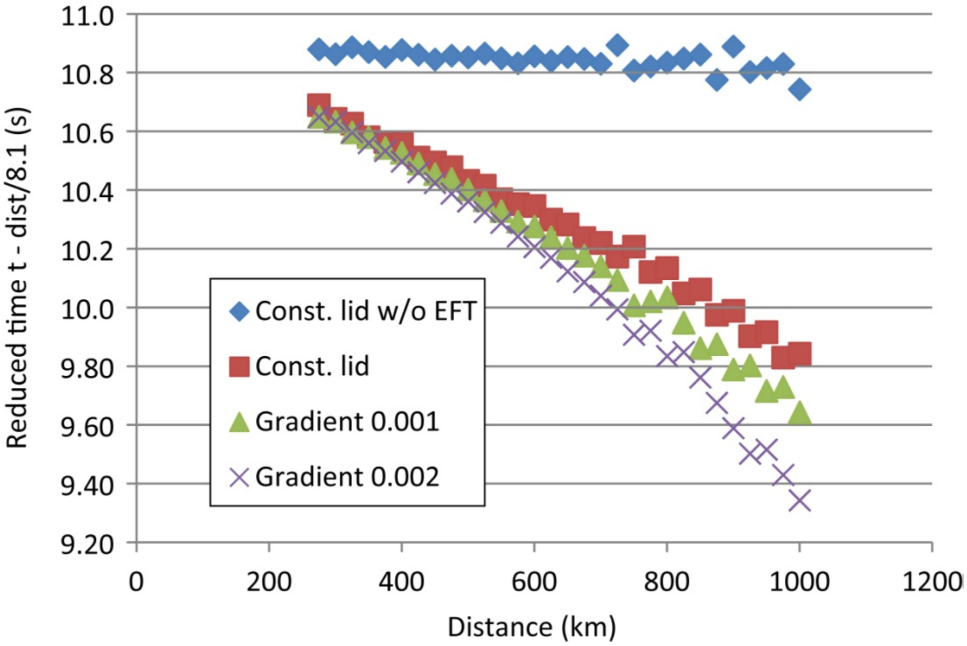

Figure 24. Arrival time picks from profiles of synthetics in Figure 22 displaying the weak curvature introduced by linear mantle lid gradients. While the variations are subtle, given sufficient observations and laterally uniform structure, the mantle gradient can be constrained by Pn arrival time picks, providing velocity models that can be used for self-consistent regional amplitude spreading calculations.

4.4 *Pn Geometric Spreading for 1D and 2D Velocity Models*

For the 1D models in Figures 14 and 15, we computed frequency-dependent geometric spreading amplitude decay out to 1000 km using the finite-different calculations, correcting for excitation of a point-source versus a line-source. This yields the amplitude-distance curves shown in Figure 25. These patterns are very similar to wavenumber-integration calculations (Figure 4) for the 1D velocity models computed in Avants et al. (2011). The complex frequency-dependence of Pn, with minima in the amplitude-distance curves and increasing amplitudes at larger distances, particularly for higher frequencies, being evident for all structures with a positive gradient in the 1D flat earth structure. Comparison of the amplitude behavior for these models for different narrow frequency bands is displayed in Figure 26. For lid gradients in excess of 0.002 sec^{-1}, the distance and frequency dependence are quite dramatic as shown in Figure 27 and Figure 28, with complex plateauing and oscillation of the high frequency components. Some of the large distance, high frequency behavior is not well-resolved, but very similar behavior is found for the completely independent frequency-wavenumber integration synthetics in Figure 4. Overall, these calculations provide a good level of confidence in the broadband Pn synthetics, and we proceed to consider results for 2D models.

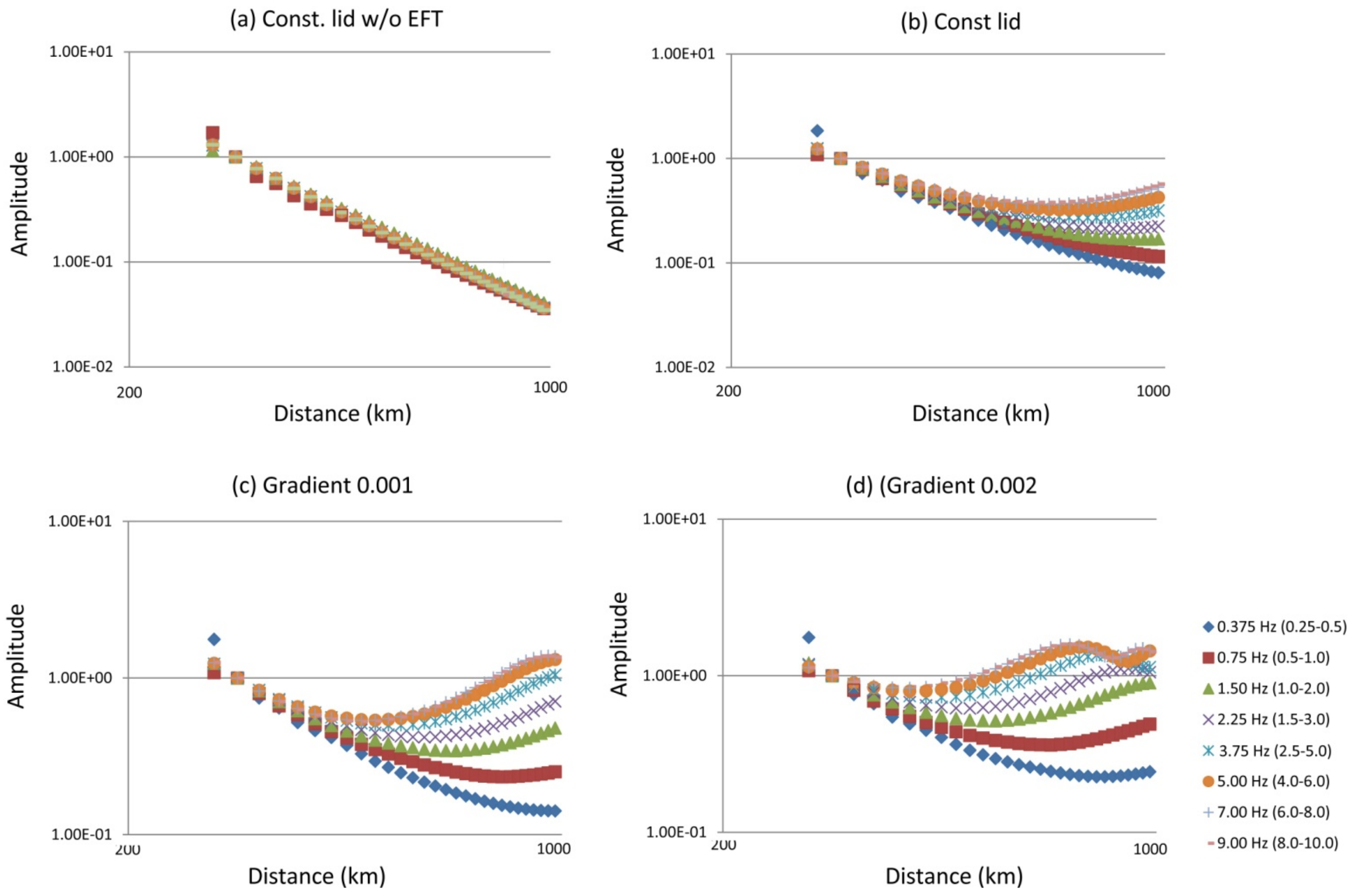

Figure 25. Frequency-dependence of Pn amplitude vs. distance relations on log-log scale. (a) to (d) are for different velocity models. The frequency filters are indicated by the symbols. Rms amplitudes are used in this figure, and all curves are normalized at 300 km. As expected, in the Const.-Lid w/o EFT, the amplitude-distance relation for a true head wave is frequency independent.

The Pn amplitude distance curves for 2D models, with lateral variations in the radial gradients, as displayed in Figure 16 are shown in Figures 29-32. Figure 29 shows the variation between end-member 1D models Gradient-0.000 and Gradient-0.001, with the near source environment and receiver environment interchanging between these two models. All models have positive gradients from the EFT. Note the difference in geometric spreading for sources in different near-source velocity structure. This indicates that it is not straightforward to use a single average model to represent the geometric spreading in a laterally varying model. The lateral averaging of the 2D structures is such that the closer distances have amplitude variations consistent with the 1D end-member structure near the source, while the larger distances have geometric spreading similar to the 1D end-member structure near the receiver. This is emphasized in Figure 30, for the 2.5-5.0 Hz passband, where the 1D and 2D spreading curves are superimposed. The 2D spreading behavior is overall intermediate to the end-members, but does depend on direction of the paths.

(a) 0.75 Hz (0.5-1.0)

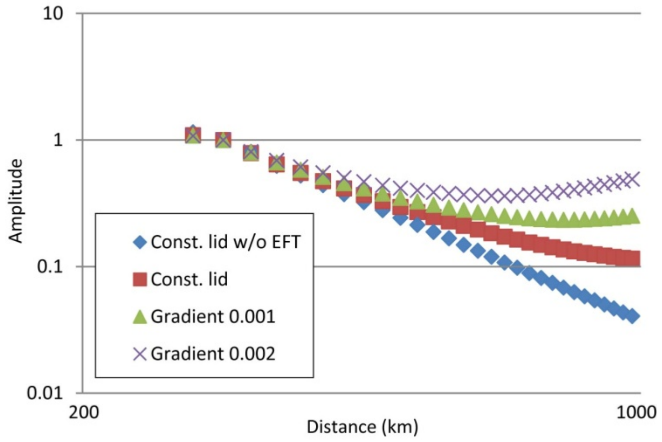

(b) 3.75 Hz (2.5-5.0)

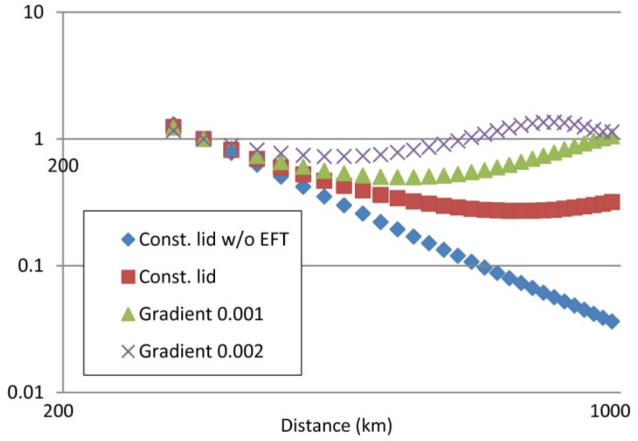

(c) 7.00 Hz (6.0-8.0)

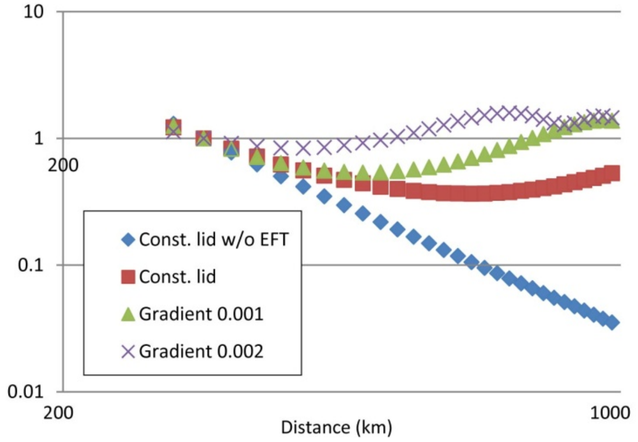

Figure 26. Amplitude vs. distance on log-log scale for different models, for narrow-band filtered signals with central frequencies and passbands of: (a) 0.75 Hz (0.5-1.0 Hz), (b) 3.75 Hz (2.5-5.0 Hz), and (c) 7.0 Hz (6.0-8.0 Hz).

Approved for public release; distribution is unlimited.

(a) Gradient 0.003

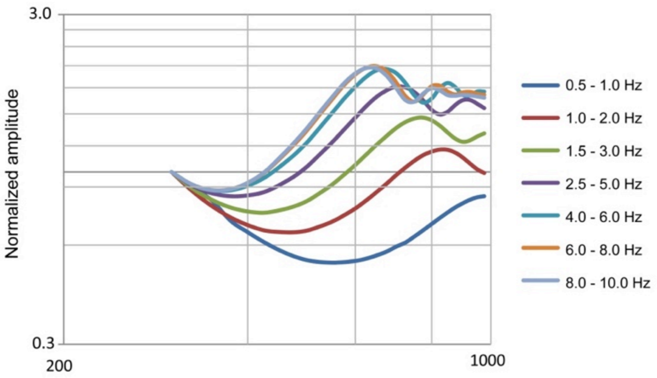

(b) Gradient 0.004

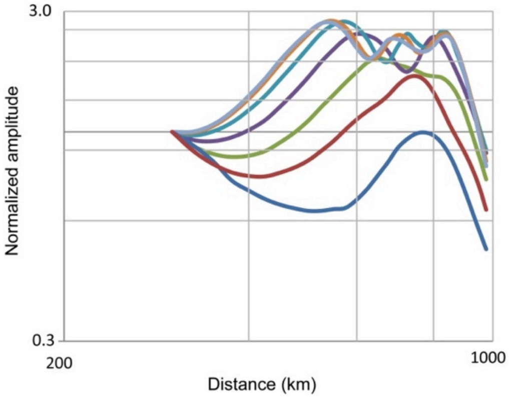

Figure 27. Frequency-dependence of amplitude vs. distance relations in log-log scale. (a) In Gradient-0.003 model, and (b) Gradient-0.004 model. Refer to Figure 15 for velocity models.

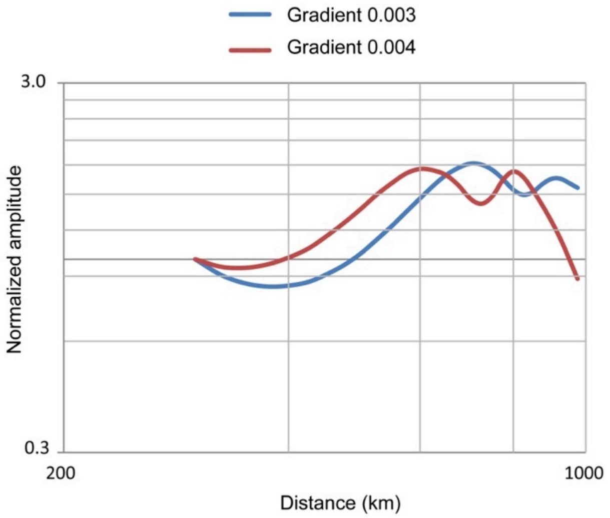

Figure 28. Comparison of amplitude vs. distance relations for Gradient-0.003 and Gradient-0.004 models at frequency 3.7 Hz.

Approved for public release; distribution is unlimited.

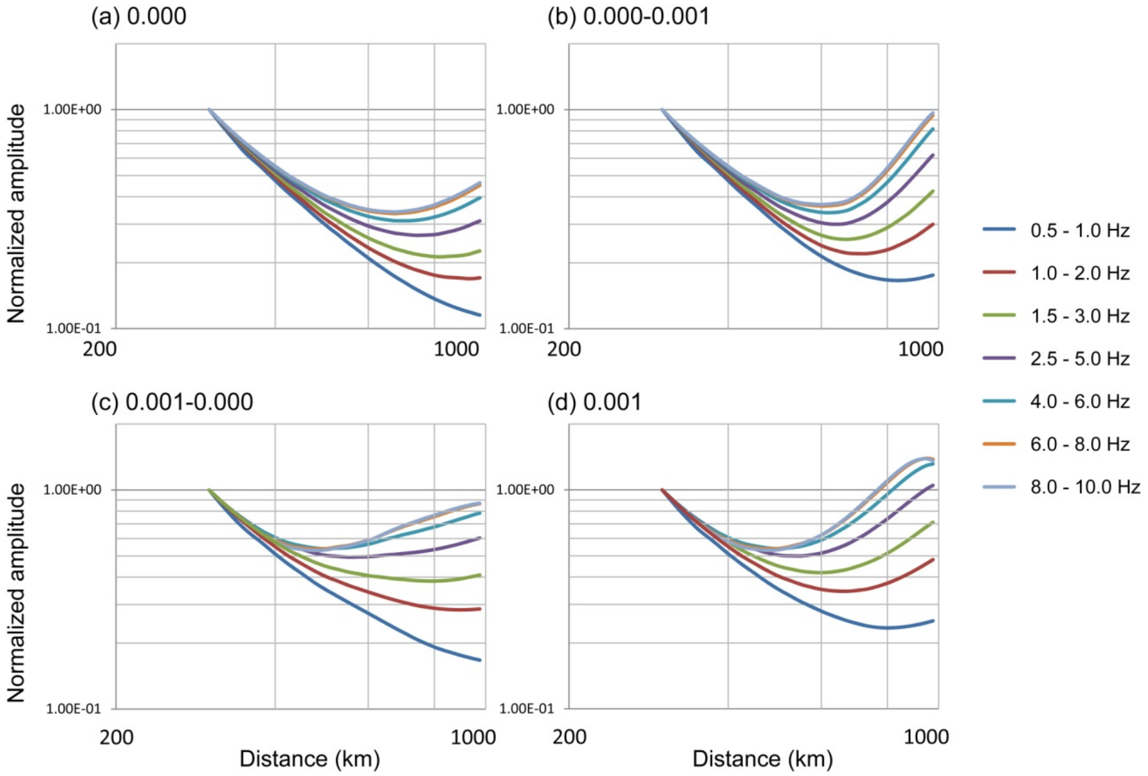

Figure 29. Amplitude-distance relations in different 1D and 2D laterally varying velocity models and frequency bands. The models are: (a) Gradient-0.000, (b) Gradient-0.000-0.001, (c) Gradient model 0.001-0.000, and (d) Gradient-0.001. Note that the amplitudes for 6-8 Hz and 8-10 Hz bands are very close.

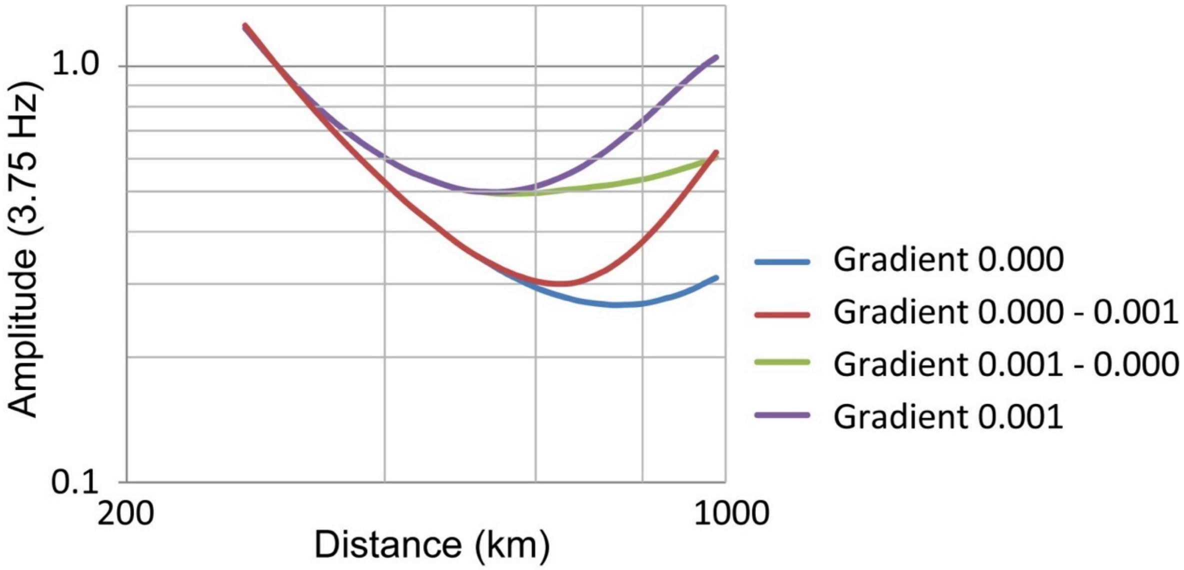

Figure 30. Comparisons for amplitude-distance relations for 1D and 2D laterally varying models. The used frequency band is 2.5-5.0 Hz. Note the transition zone in the 2D structures is between 450 – 550 km.

Approved for public release; distribution is unlimited.

Similar comparisons are shown for the models involving stronger radial gradients in the lid in Figures 31 and 32, ranging from end-member models Gradient-0.000 to Gradient-0.002. The lateral averaging behavior is similar to the Gradient-0.001 models, although the stronger amplitude variations associated with the strong gradient in Gradient-0.002 enhance the variations in the 2D models. The frequency-dependence at large ranges is strong for all models, but the distance variation in the amplitudes is distinct for each model, as emphasized in Figure 30, which compares the amplitude-distance curves for the 2.5-5.0 Hz band. The complexity of the frequency-dependent amplitudes for the laterally varying models and the strong direction-dependence of the amplitude behavior would be mapped into complex frequency-dependence of attenuation and possible anisotropic attenuation if the effects of the elastic velocity structure are not correctly accounted for.

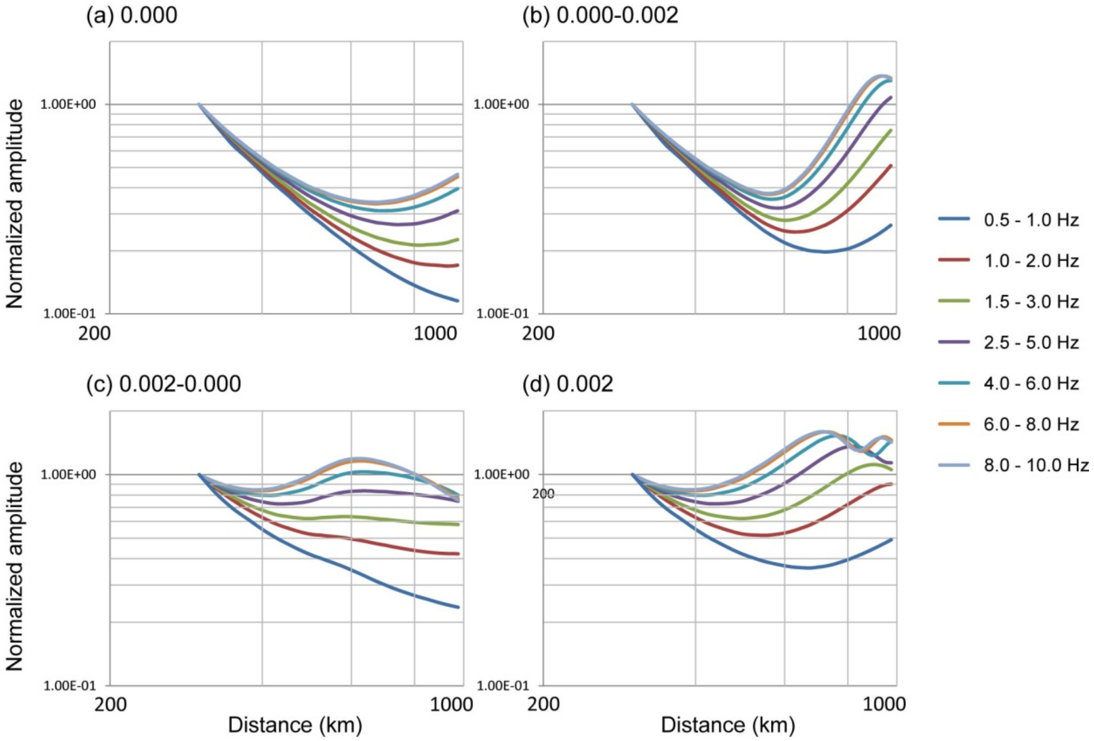

Figure 31. Amplitude-distance relations in different laterally varying velocity models and frequency bands. The models are: (a) Gradient-0.000, (b) Gradient-0.000-0.002, (c) Gradient model 0.002-0.000, and (d) Gradient-0.002. Note that the amplitudes for 6-8 Hz and 8-10 Hz bands are very close.

Approved for public release; distribution is unlimited.

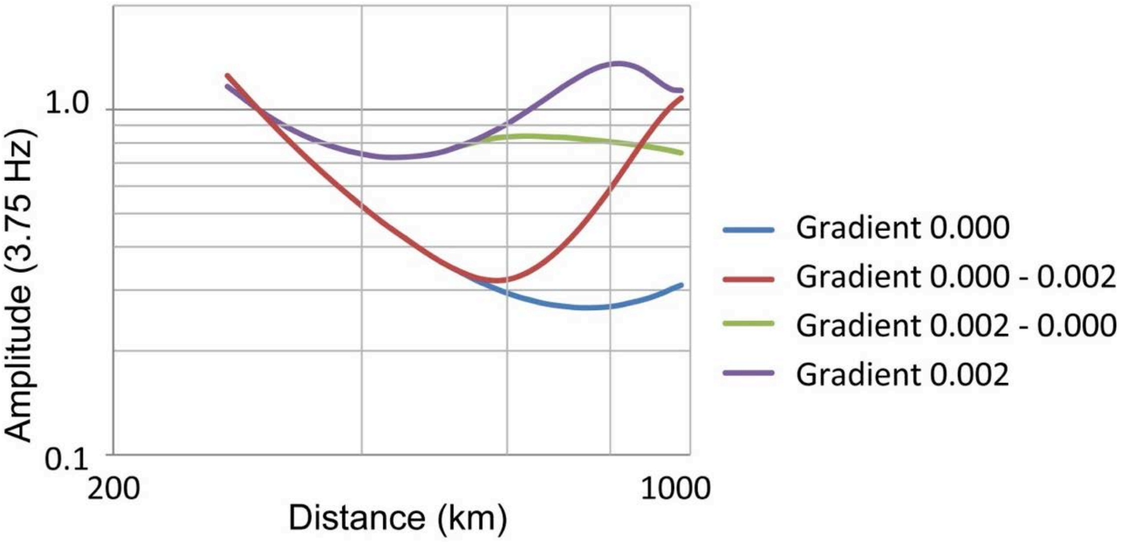

Figure 32. Comparisons of amplitude-distance relations for different laterally-varying velocity models. The frequency band is 2.5-5.0 Hz. Note the transition zone in the 2D models is between 450 – 550 km.

4.5 *Pn Spreading in Models With Fine-Scale Heterogeneity*

It is now well established by the work described above that Pn (and Sn) can not usually be treated as a simple conical headwave developed along a flat Moho discontinuity. Figure 33 schematically depicts the factors that affect the amplitude of Pn. Starting from a conventional headwave case, where a constant low-velocity crust (the upper half-space) is welded to a constant high-velocity mantle (the lower half-space) at a planar Moho discontinuity (Figure 33a), a source located in the crust can excite waves propagating from the source to the refracting point at the Moho, and then propagating horizontally in the mantle immediately below the Moho. The energy of this high-speed mantle wave can leak back to the crust and be observed as the headwave in the upper half space. The upper mantle leg is composed of waves with imaginary vertical wavenumber. In this circumstance, there is no vertically propagating mode. The energy immediately below the Moho is quickly depleted without being recharged from the deeper depth, resulting in rapid decay of the observed headwave amplitude. Actual Pn wave propagation, particularly for Pn amplitude variations in a spherical Earth, is much more complicated. Červený and Ravindra [1971] and Hill [1973] theoretically investigated the behavior of Pn waves in a spherical Earth model and regarded this phase as an interference of multiple-diving waves reflected from the underside of the Moho discontinuity. Sereno and Given [1990] studied Pn waves in flat and spherical earth models and found that Earth's sphericity alone causes a significant complexity in Pn geometrical spreading and this phenomenon is frequency dependent. The sphericity in the Earth is equivalent to a positive velocity gradient in the mantle (Figure 33b), which causes whispering gallery phases reflected from the underside of the Moho. In this way the energy at the great depth can feed the depleted energy below the Moho, making the observed Pn wave much stronger than the headwave. In addition, in a simple two constant velocity half-space

Approved for public release; distribution is unlimited.

system, there is no characteristic length scale. Waves of different wavelengths (or frequencies) behave equally. Therefore, the geometrical spreading function for headwave is frequency independent. However, in a model with upper mantle velocity gradient, the gradient serves as a characteristic scale, and the Pn wave geometric spreading function becomes frequency dependent.

If lateral velocity variations exist in the upper mantle, scattering may affect the Pn wave propagation in a way that is quite different from its effects on other waves (Figure 33c). For most body and surface waves, the scattering process deflects the wave energy away from its main propagation direction, causing the wave to lose energy. This process is known as scattering attenuation. However, the Pn wave is confined by the Moho discontinuity and the upper mantle velocity gradient. In a laterally smooth waveguide, relatively little energy escapes from the main propagation channel to radiate upward to form the observed Pn. The presence of small-scale heterogeneities in the upper mantle can cause scattering and its effect on Pn wave propagation are twofold. First, as for other waves, the scattering can cause attenuation along the upper mantle channel. Second, the scattering makes an efficient mechanism to increase the observed Pn amplitude by deflecting the energy away from the main propagation direction in the upper mantle. Compared to otherwise very weak Pn energy, the scattered energy can be strong, causing prominent enhancement of the Pn amplitudes. This often causes somewhat of a dilemma for the Pn wave, as to whether the scattering should be treated as scattering attenuation, or as geometrical spreading, but both are elastic effects controlled by the velocity structure.

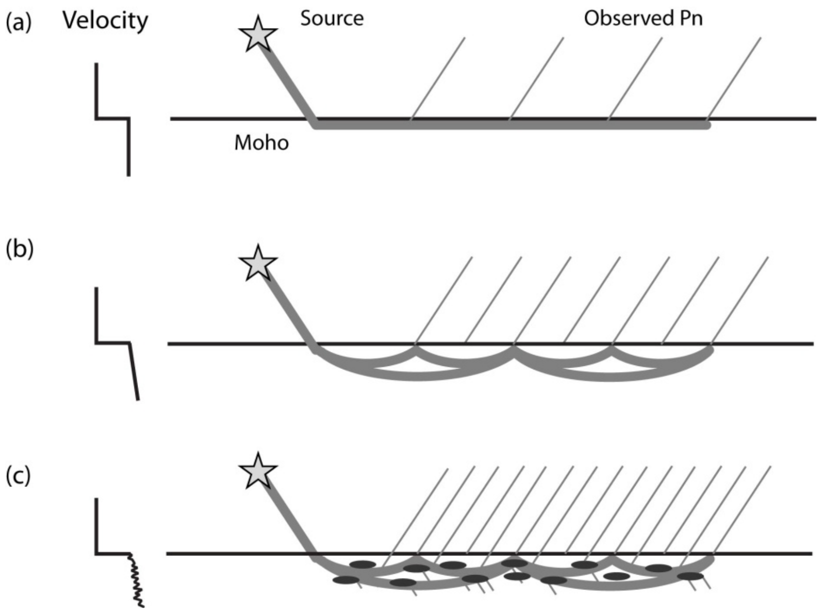

Figure 33. Pn waves in different crust-upper mantle velocity models, with (a) simple constant velocity crust and upper mantle, and a planar Moho, giving rise to a true conical head wave; (b) vertical velocity gradient in the upper mantle, giving rise to the frequency-dependent spreading examined earlier, and (c) laterally varying fine-scale velocity heterogeneity in the upper mantle.

Approved for public release; distribution is unlimited.

In this section we introduce fine-scale heterogeneities to our smoothly varying velocity gradient models to explore the effect on the Pn geometric spreading behavior. The goal is to extend the calculations of Avants et al. (2011) to higher frequency and to thereby evaluate frequency-dependent effects of the fine-scale structure. The random velocity models are generated by adding velocity and density perturbations to the mantle part of 1D velocity models illustrated in Figure 14. These models have a constant velocity crust. Below the Moho discontinuity, the mantle has a given vertical velocity gradient of 0.000, 0.001 or 0.002. Below this gradient layer, the mantle follows the Iasp-91 earth model. The random velocity perturbations have an exponential spectrum, and are characterized by the horizontal and vertical correlation lengths, and the rms velocity perturbation. Both P and S wave velocities have the same percentage perturbation, and the density perturbation is half of the velocity perturbation. The model parameters are listed in Table 4.

Table 4. 2D Velocity Models With Fine Scale Heterogeneity

No	Background model	Type of random function	Correlation length	RMS perturbation	Radom seeds calculated
1	Const lid (0.000)	exponential	20 km x 6 km	0.5%	3,5,7,8,9
2	Const lid (0.000)	exponential	20 km x 6 km	1.0%	3,5,7,8,9
3	Const lid (0.000)	exponential	20 km x 6 km	2.0%	3,5,7,8,9
4	Const lid+0.001 grad.	exponential	20 km x 6 km	0.5%	3,5,7,8,9
5	Const lid+0.001 grad.	exponential	20 km x 6 km	1.0%	3,5,7,8,9
6	Const lid+0.002 grad.	exponential	20 km x 6 km	1.0%	3,5,7,8,9
7	Const lid+0.001 grad.	exponential	40 km x 10 km	0.5%	3,5,7,8,9
8	Const lid+0.001 grad.	exponential	40 km x 10 km	1.0%	3,5,7,8,9
9	Const lid + 0.001 grad.	exponential	10 km x 3 km	1.0%	3,5,7,8,9

For each group of random heterogeneity parameters, we generate 5 velocity realizations using different random seeds, and calculate the wave propagations in these models for up to 1,000 km distance. The source time function is a Gaussian derivative $(t-t_s)\exp\left[-(t-t_s)^2/\tau^2\right]$, with $\tau = 0.2\,\text{sec}$. The earth flattening transform (EFT) is used to convert the spherical earth into a flat earth. A factor of 1/sqrt(r) is used to transfer the geometry from 2D to 3D. Illustrated in Figure 34 are examples of Pn waves propagating in models without and with random velocity fluctuations. Figure 34a and 34b are Pn waves propagating in the background velocity model, and 34c and 34d are Pn wave propagations in a velocity model with 1% rms velocity perturbations. The pervasive generation of scattered waves is readily evident in the snapshots, particularly in the Pn coda.

Approved for public release; distribution is unlimited.

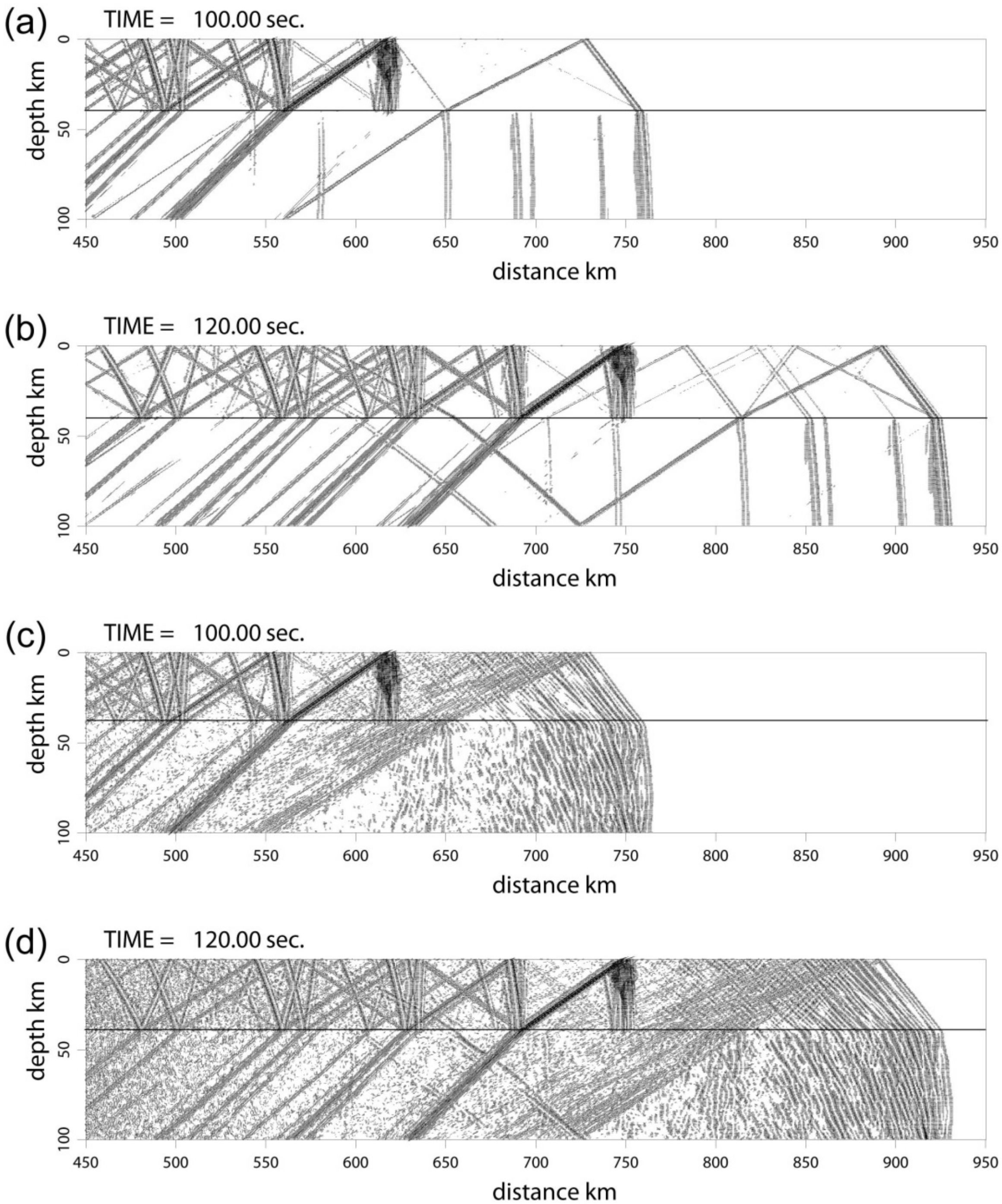

Figure 34. Wavefield snapshots in velocity models without (a), (b) and with (c), (d) random velocity perturbations. The model is composed of a 40 km thick constant velocity crust and an upper mantle with 0.001 vertical velocity gradient. The upper mantle for the calculations in (c) and (d) has 1% rms velocity perturbations and the horizontal and vertical correlations lengths are 20 km and 6 km, respectively.

The synthetic seismograms are processed using the following procedure:

Approved for public release; distribution is unlimited.

(1) Bandpass filter the seismograms with central frequencies 0.4, 0.8, 1.5, 3.0, 6.0 and 10.0 Hz.
(2) Group velocity windowing between 8.2 km/s and 7.6 km/s is used for sampling the Pn signal.
(3) The rms amplitude is calculated within the group velocity window.
(4) All amplitudes are normalized by the spectra from the corresponding 1D velocity model calculations at a reference distance of 300 km.
(5) The mean value from five realizations of the random structure is calculated and used as the result.

Figures 35 to 43 present calculations of the Pn wave spectral amplitudes versus distance for random velocity models number 1 to 9 listed in Table 4. The vertical coordinate is the spectral amplitude, and the horizontal coordinate is the distance. In each figure, panels (a) to (f) are for frequencies 0.4, 0.8, 1.5, 3.0, 6.0 and 10.0 Hz, respectively. Light colored symbols are amplitudes calculated from individual random realizations. Solid squares with error bars are mean values and standard deviations from all five realizations. The solid diamonds are from the background 1D velocity model. As a comparison, shown in panel (g) are decay curves for different frequencies in the 1-D background model. Shown in panel (h) are related decay curves in models with random velocity perturbations in the upper mantle. All amplitudes are normalized by the amplitude in the background model at a reference distance of 300 km. Thus the source spectrum is removed.

For each model, the Pn amplitudes for the heterogeneous structure are enhanced relative to the expected behavior for the 1D reference structure underlying the heterogeneity. This is a direct manifestation of the dominant effect of scattering of strong energy out of the lid waveguide into the crustal Pn phase as depicted in Figure 33c and captured in the snapshot in Figure 34c,d. The effect increases with frequency, noting that the spectral levels are relative to the reference distance of 300 km, where the structural effects and scattering effects are relatively minor. The random models have variability as expected, but the average behavior over the five realizations is quite stable. Some of the small-scale structure in the amplitude curves may begin to average out with a greater number of realizations, but some of it may persist as a function of the specific anisotropy of the heterogeneity. While smooth curvature of the patterns and the increase with distance for the stronger gradient models is suppressed in the scattering calculations, the overall frequency dependence of the models is actually enhanced in all cases relative to the 1D reference case. This emphasizes that the 1Hz calculations of Avants et al. (2011) capture some of the basic effect of the heterogeneous structure, but the frequency dependence is not lost by the scattering. The actual small-scale structure on any given path is not known, but the assertion by some researchers that it will homogenize the signals such that no overall frequency dependence of the Pn spreading would be manifested and a single frequency-independent power-law decay relationship is sufficient is clearly not supported by these calculations (the first systematic treatment that we are aware of for the Pn phase).

Approved for public release; distribution is unlimited.

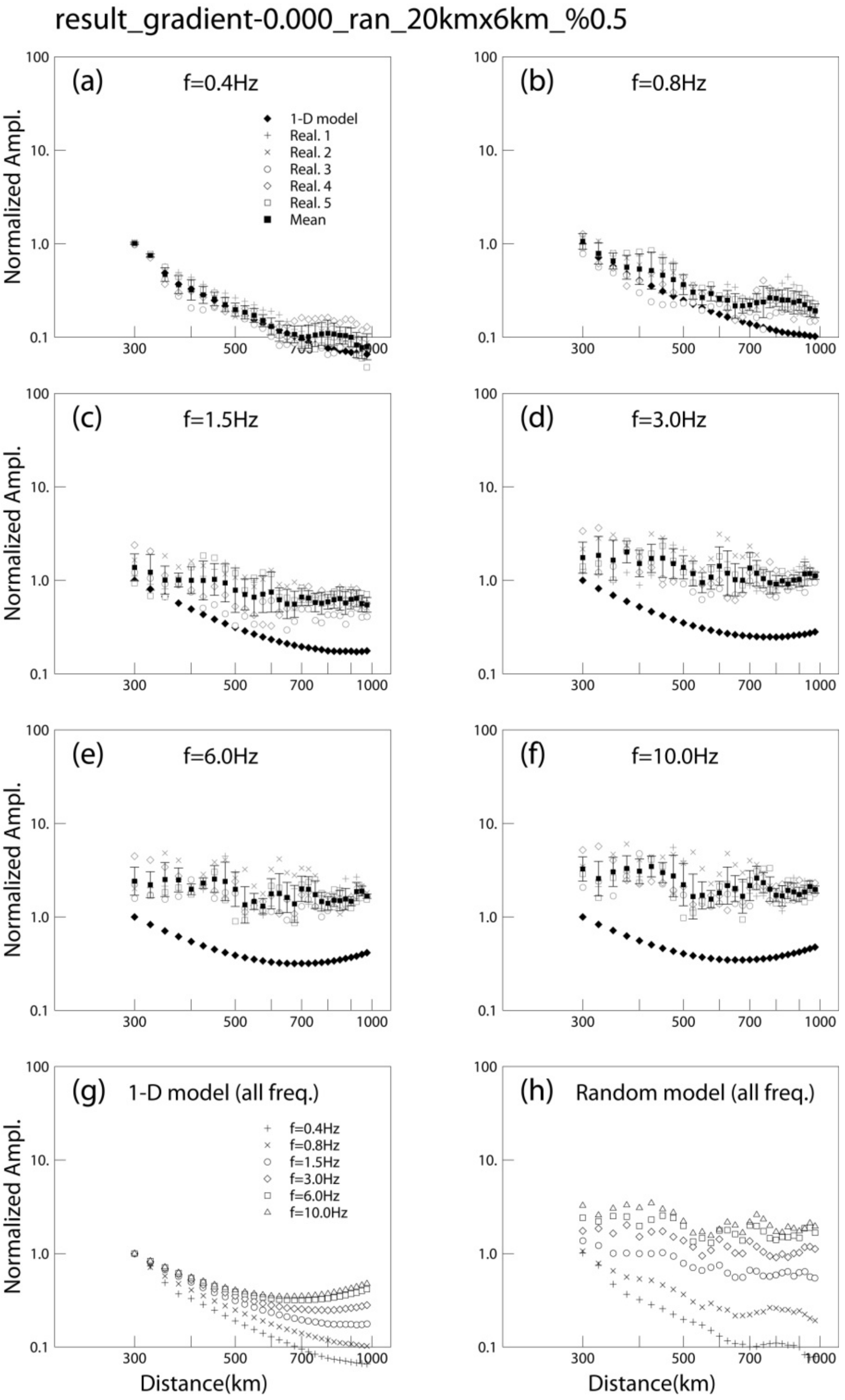

Figure 35. Pn wave spectral amplitude versus distance calculated from random velocity model Grad._0.000_ran_20kmx6km_0.5% (Model No 1 in Table 4). (a) to (f) are spectral amplitudes at frequencies 0.4, 0.8, 1.5, 3.0, 6 and 10 Hz. (g) Amplitudes in the 1D background model. Different symbols are for different frequencies. (h) Mean amplitudes for the random velocity model.

Approved for public release; distribution is unlimited.

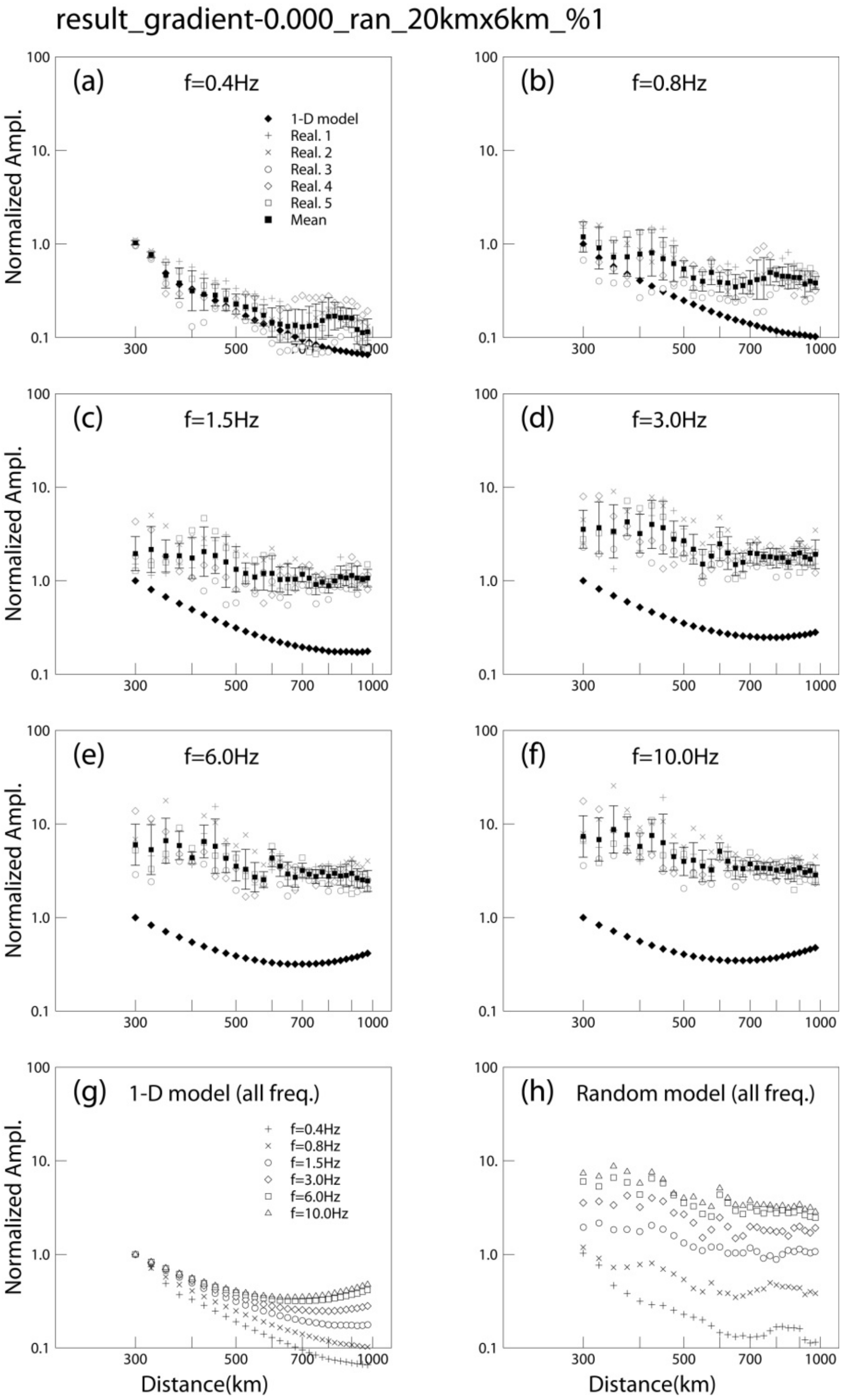

Figure 36. Pn wave spectral amplitude versus distance calculated from random velocity model Grad._0.000_ran_20kmx6km_1.0% (Model No 2 in Table 4). (a) to (f) are spectral amplitudes at 0.4, 0.8, 1.5, 3.0, 6 and 10 Hz. (g) Amplitudes in the 1D background model. Different symbols are for different frequencies. (h) Mean amplitudes for the random velocity model.

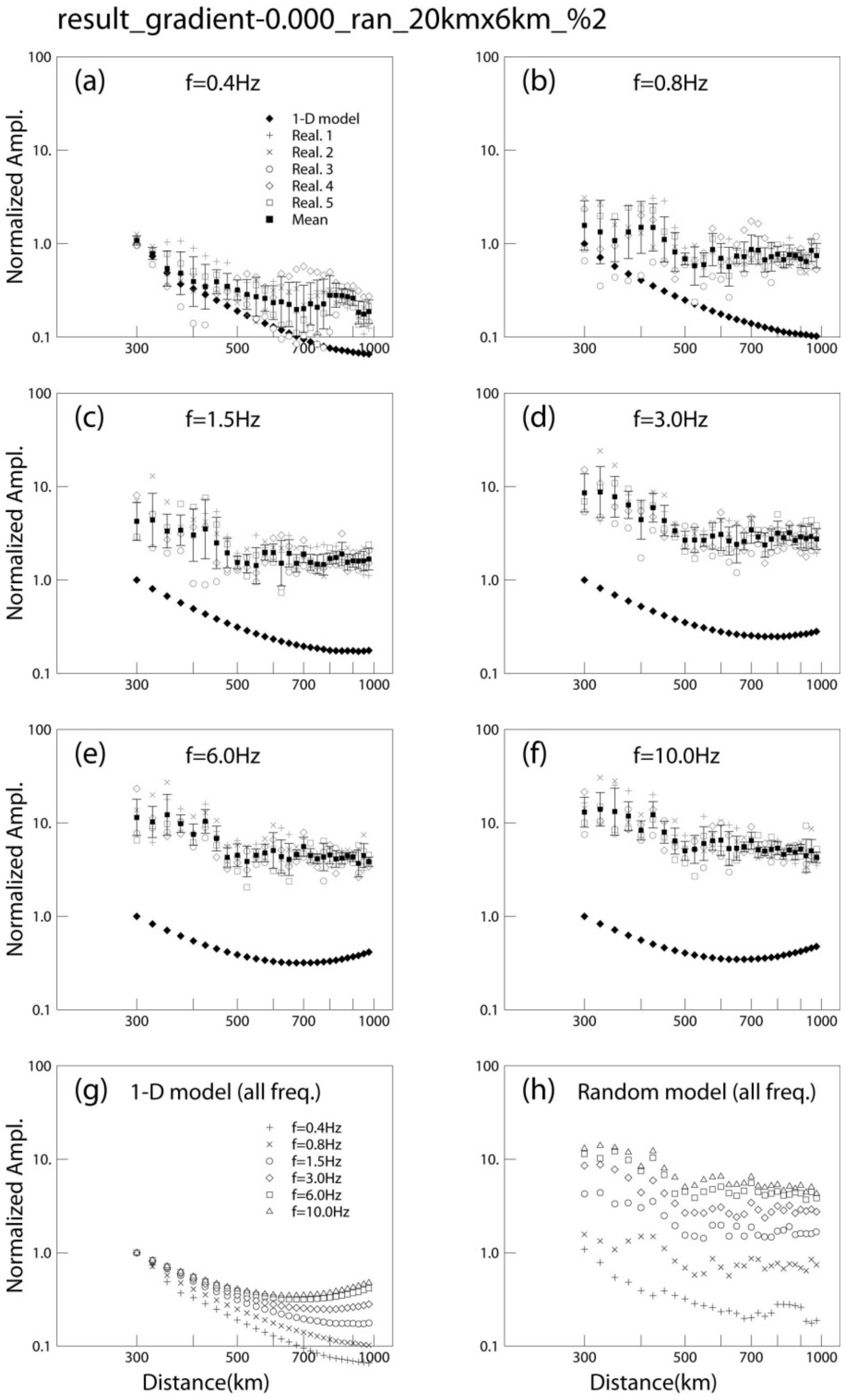

Figure 37. Pn wave spectral amplitude versus distance calculated from random velocity model Grad._0.000_ran_20kmx6km_2.0% (Model No 3 in Table 4). (a) to (f) are spectral amplitudes at 0.4, 0.8, 1.5, 3.0, 6 and 10 Hz. (g) Amplitudes in the 1D background model. Different symbols are for different frequencies. (h) Mean amplitudes for the random velocity model.

Approved for public release; distribution is unlimited.

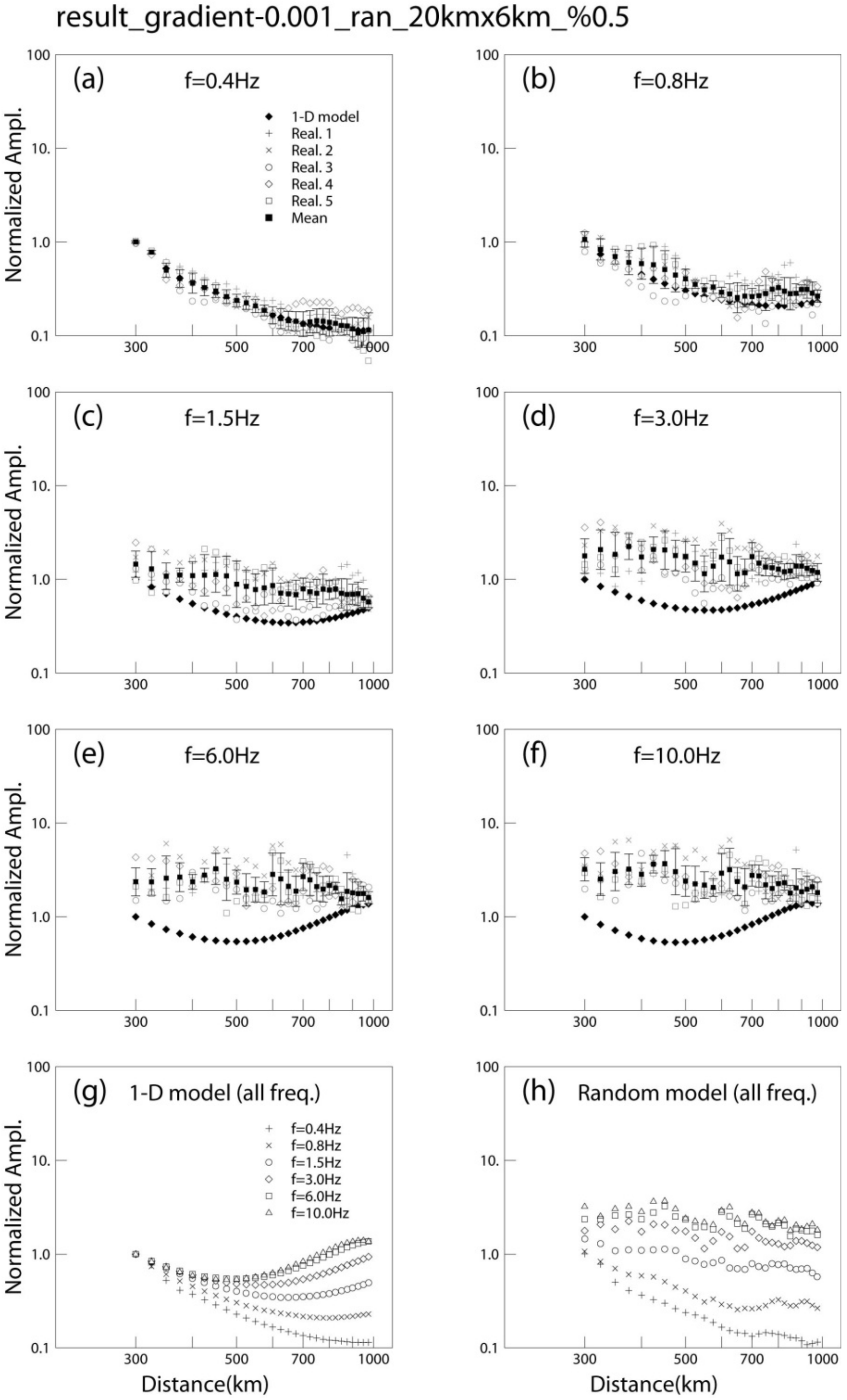

Figure 38. Pn wave spectral amplitude versus distance calculated from random velocity model Grad._0.001_ran_20kmx6km_0.5% (Model No 4 in Table 4). (a) to (f) are spectral amplitudes at 0.4, 0.8, 1.5, 3.0, 6 and 10 Hz. (g) Amplitudes in the 1D background model. Different symbols are for different frequencies. (h) Mean amplitudes for the random velocity model.

Approved for public release; distribution is unlimited.

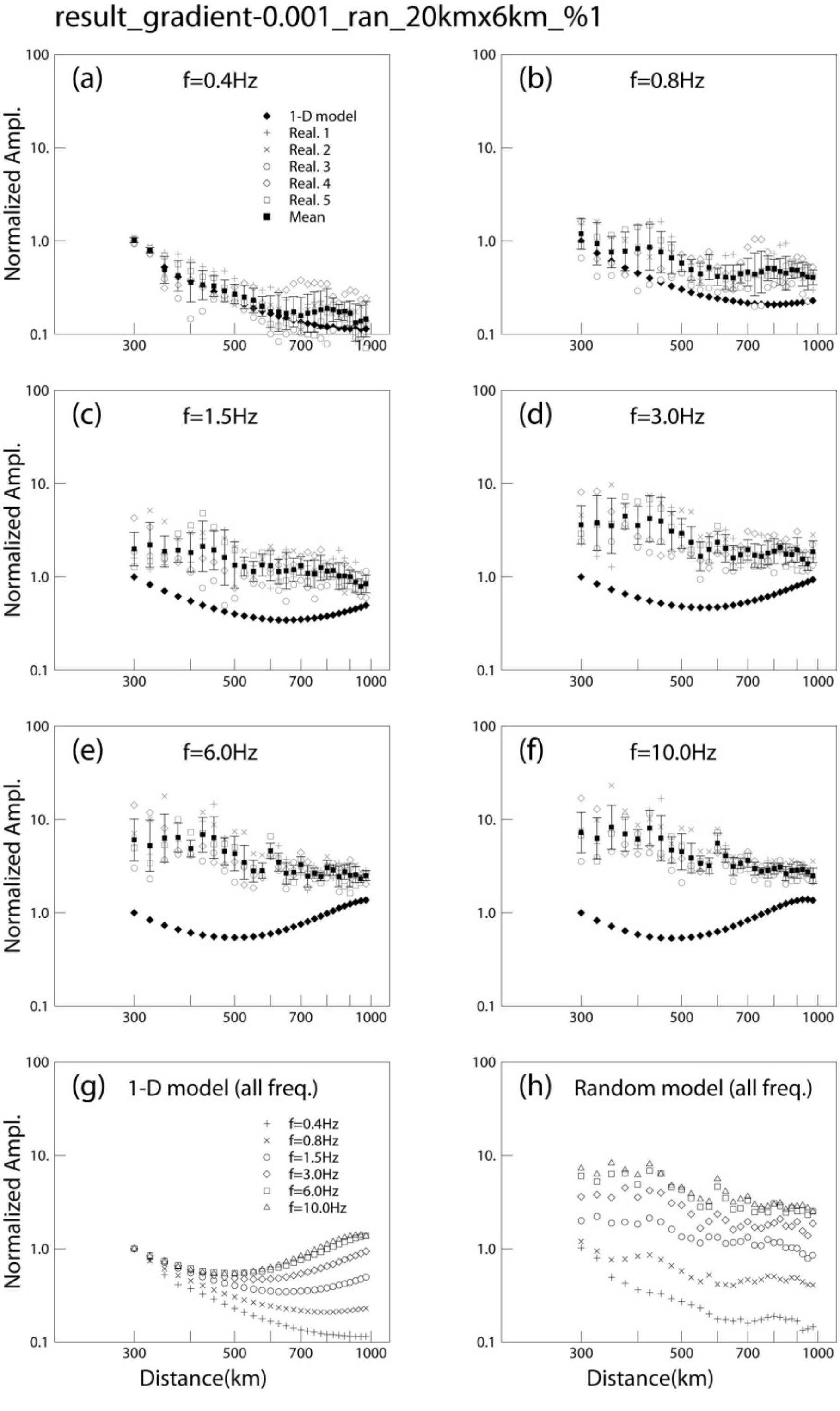

Figure 39. Pn wave spectral amplitude versus distance calculated from random velocity model Grad._0.001_ran_20kmx6km_1.0% (Model No 5 in table 4). (a) to (f) are spectral amplitudes at 0.4, 0.8, 1.5, 3.0, 6 and 10 Hz. (g) Amplitudes in the 1D background model. Different symbols are for different frequencies. (h) Mean amplitudes for the random velocity model.

Approved for public release; distribution is unlimited.

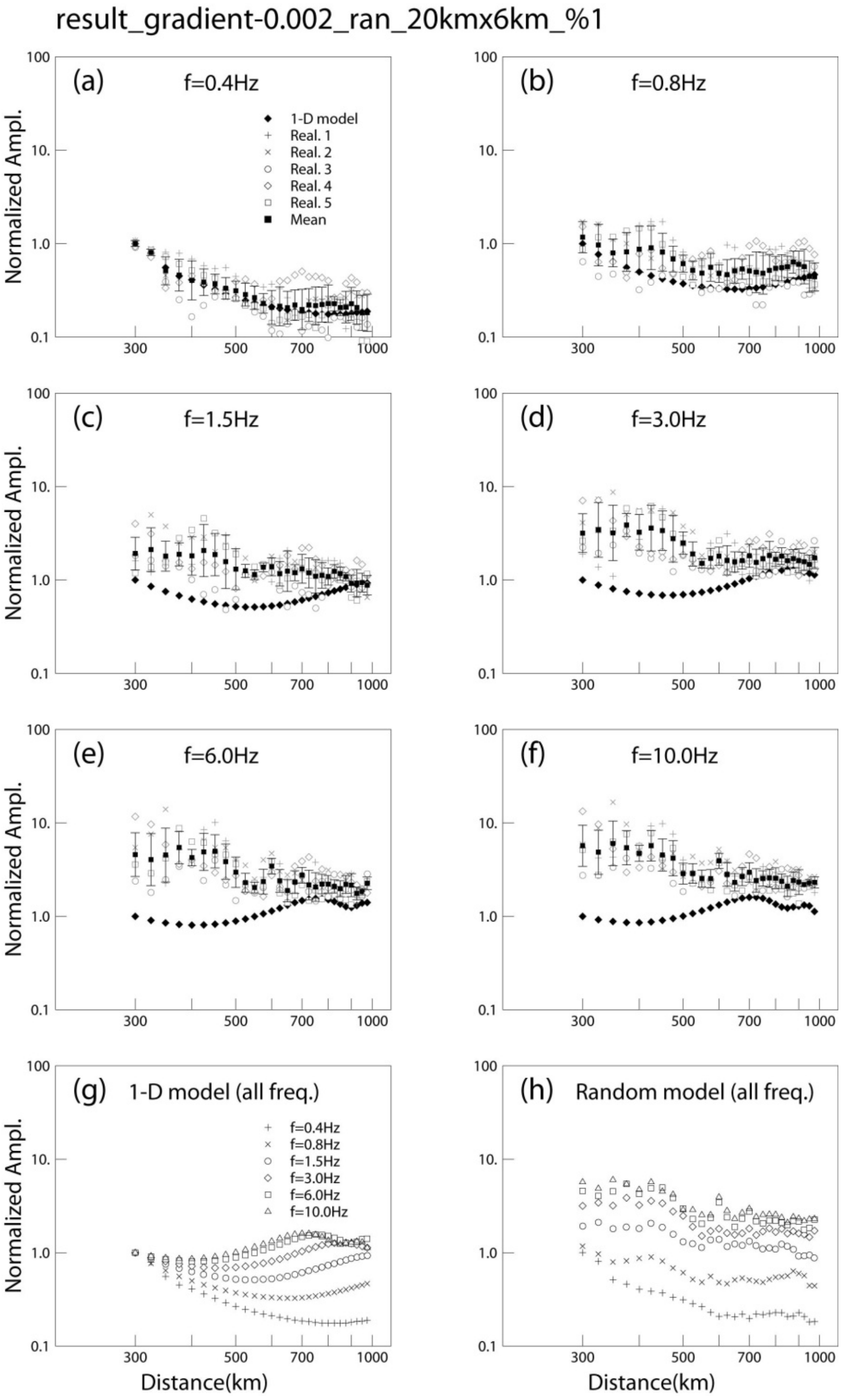

Figure 40. Pn wave spectral amplitude versus distance calculated from random velocity model Grad._0.002_ran_20kmx6km_1.0% (Model No 7 in table 4). (a) to (f) are spectral amplitudes at 0.4, 0.8, 1.5, 3.0, 6 and 10 Hz. (g) Amplitudes in the 1D background model. Different symbols are for different frequencies. (h) Mean amplitudes for the random velocity model.

Approved for public release; distribution is unlimited.

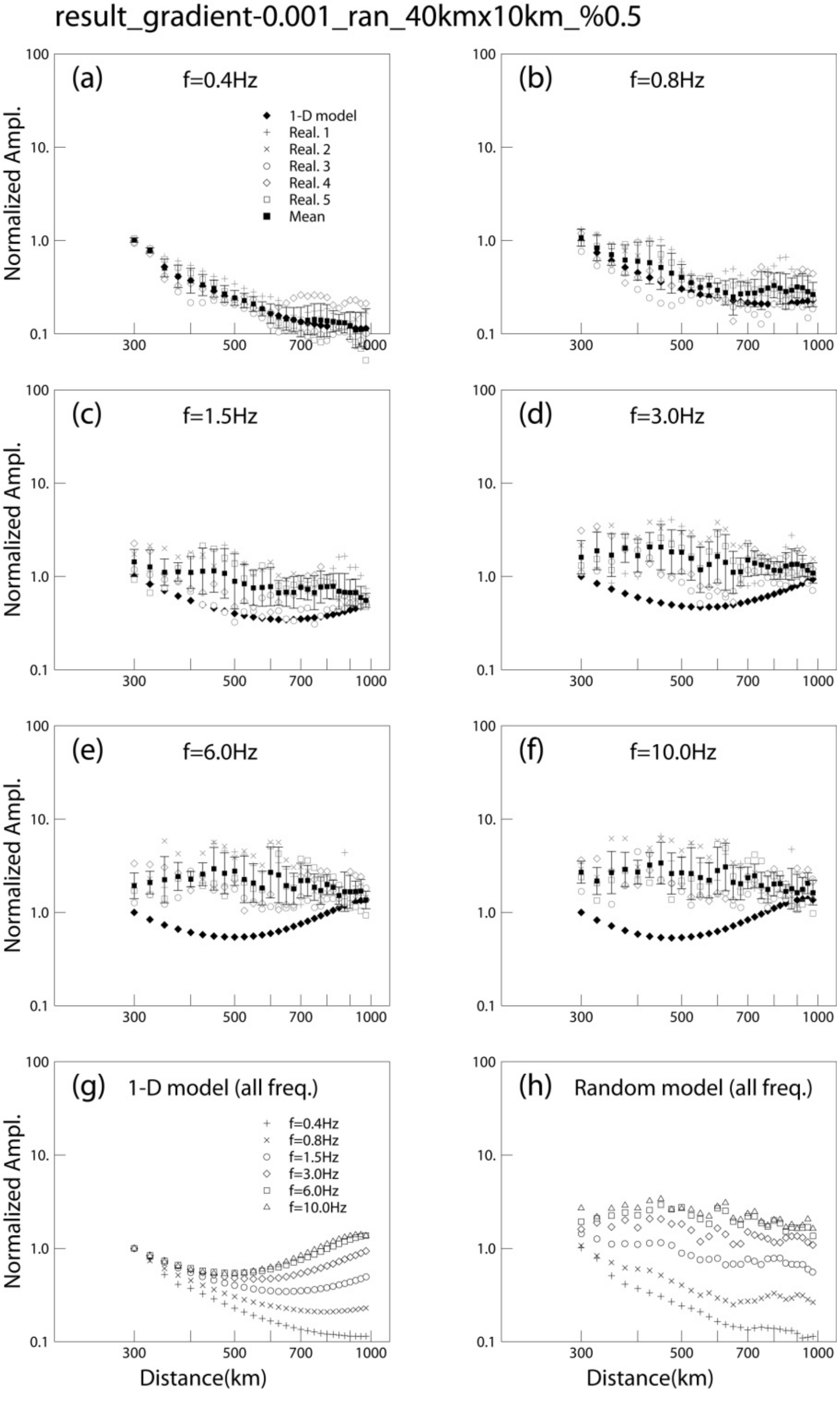

Figure 41. Pn wave spectral amplitude versus distance calculated from random velocity model Grad._0.001_ran_40kmx10km_0.5% (Model No 7 in table 4). (a) to (f) are spectral amplitudes at 0.4, 0.8, 1.5, 3.0, 6 and 10 Hz. (g) Amplitudes in the 1D background model. Different symbols are for different frequencies. (h) Mean amplitudes for the random velocity model.

Approved for public release; distribution is unlimited.

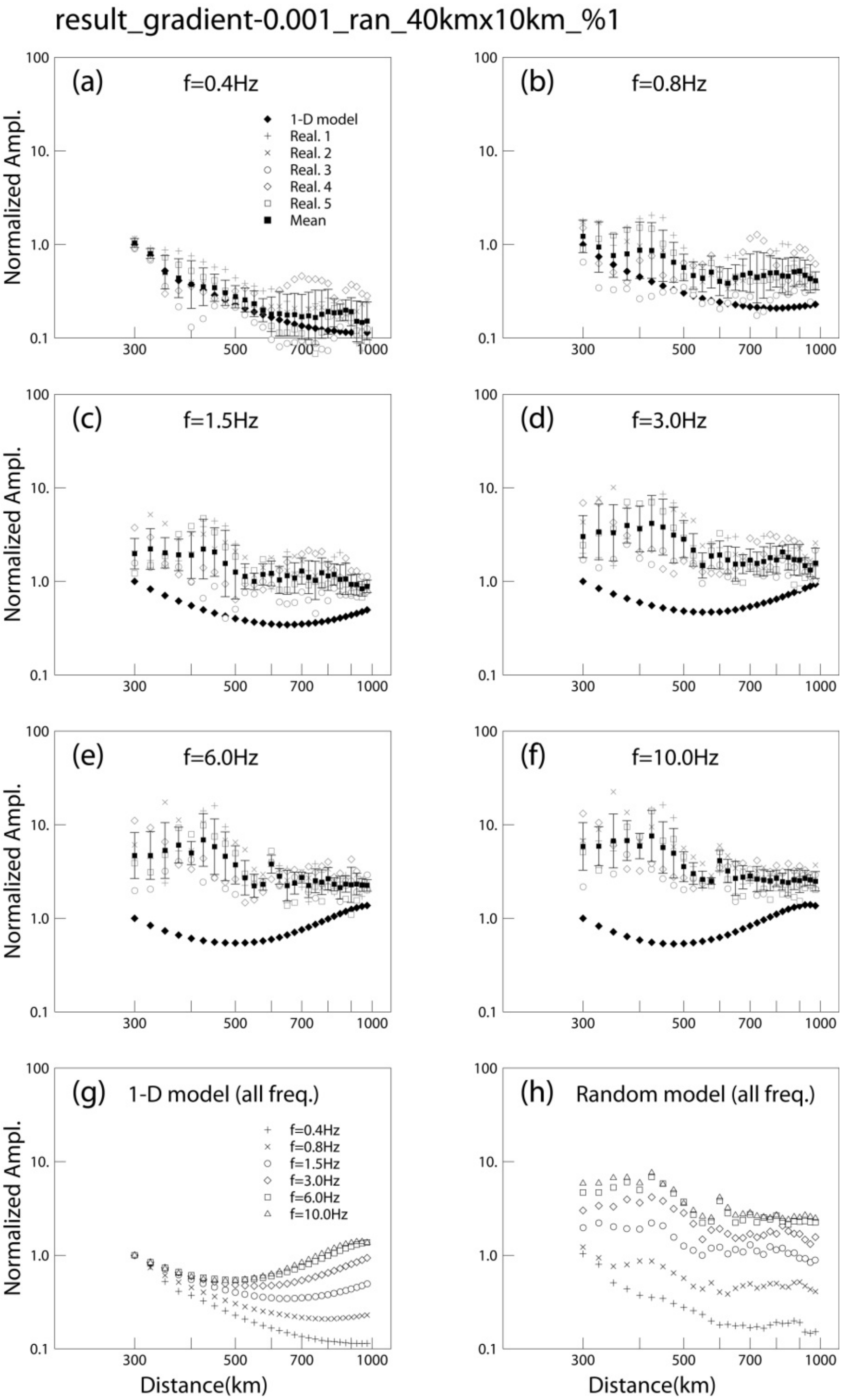

Figure 42. Pn wave spectral amplitude versus distance calculated from random velocity mode Grad._0.001_ran_40kmx10km_1.0% (model No 8 in table 1). (a) to (f) are spectral amplitudes at 0.4, 0.8, 1.5, 3.0, 6 and 10 Hz. (g) Amplitudes in the 1D background model. Different symbols are for different frequencies. (h) Mean amplitudes for the random velocity model.

Approved for public release; distribution is unlimited.

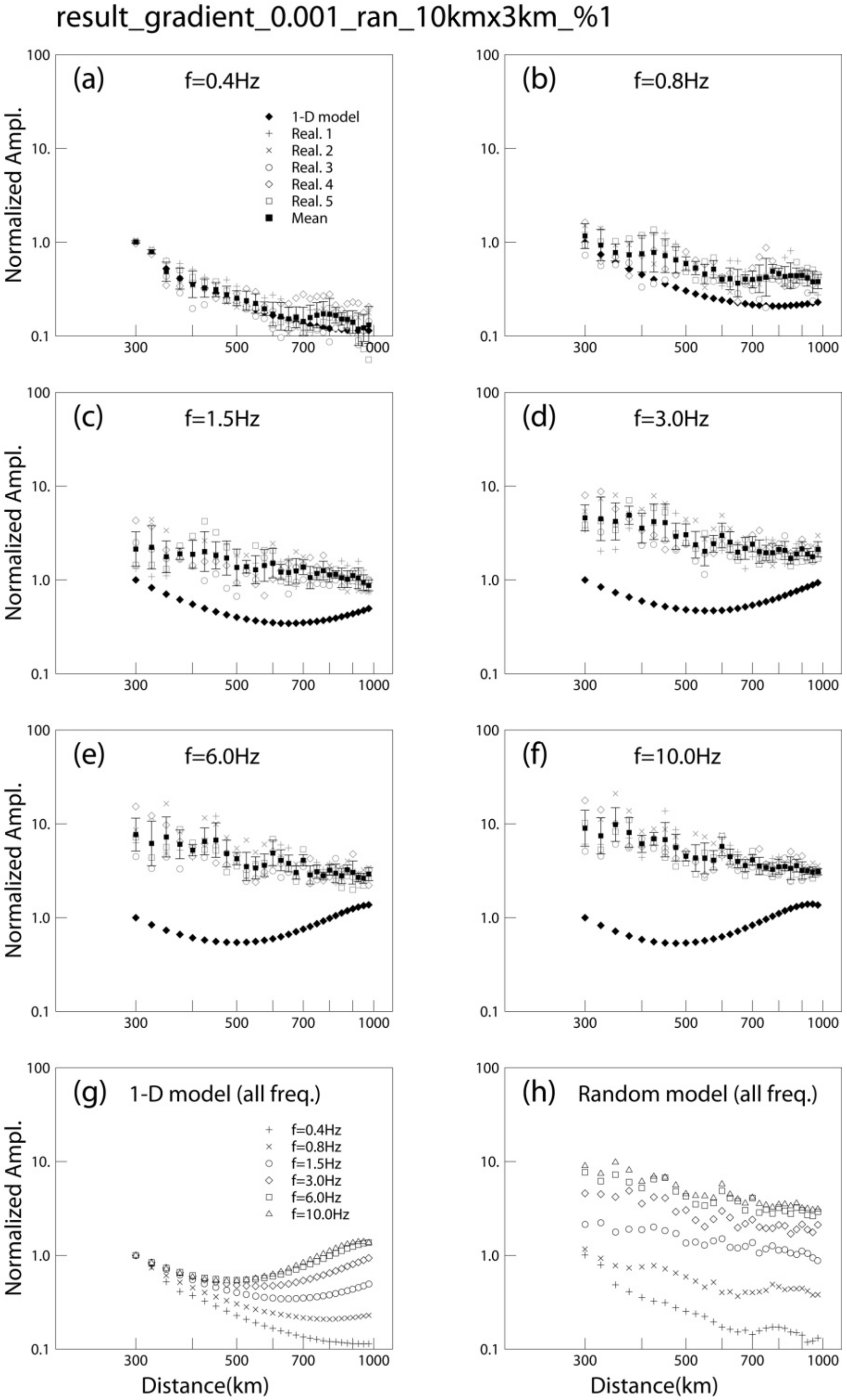

Figure 43. Pn wave spectral amplitude versus distance calculated from random velocity model Grad._0.001_ran_10kmx3km_1.0% (Model No 9 in Table 4). (a) to (f) are spectral amplitudes at 0.4, 0.8, 1.5, 3.0, 6 and 10 Hz. (g) Amplitudes in the 1D background model. Different symbols are for different frequencies. (h) Mean amplitudes for the random velocity model.

Approved for public release; distribution is unlimited.

For a velocity model with zero mantle velocity gradient and horizontal and vertical correlation lengths of 20 km and 6 km, Figure 44 compares the effects of changing rms velocity perturbations on the Pn wave amplitudes. In this figure, panels (a) to (f) are for frequencies 0.4, 0.8, 1.5, 3.0, 6.0 and 10 Hz. The open triangles, circles and squares are for random models with rms velocity perturbations of 0.5%, 1.0% and 2.0%, respectively. As a comparison, the solid squares are for the background velocity model. We see that the scattering process causes prominent amplitude increase. The amplitude increase is proportional to the rms velocity perturbations and is frequency dependent, with high frequency signals being more sensitive to the scattering. Due to the sphericity of the model, the amplitude versus distance curves in the background model curved up at large distance. The scattering effect modifies the decay curves and they show less curvature. Even though the result is calculated from five realizations, there are apparent fluctuations in these decay curves, indicating the randomness of the scattering process.

In Figure 45, comparisons are made for velocity models having the same horizontal and vertical correlation lengths (20km x 6km) and the same rms velocity perturbation of 1%, but different upper mantle velocity gradients of 0.000, 0.001 and 0.002. Panels (a) to (f) are for spectral amplitudes at 0.4, 0.8, 1.5, 3.0, 6.0 and 10.0 Hz. Triangles, squares and circles are for models with mantle velocity gradients 0.000, 0.001 and 0.002, respectively. The open symbols are for random velocity models. As comparisons, the solid symbols give amplitudes in the related background velocity models. A prominent phenomenon is, that in the presence of small-scale heterogeneities in the mantle, the scattering effect will dominate the Pn spreading function. The decay curves become less sensitive to the upper mantle velocity gradient. With scattering, the decay curves tend to approach the “power-law” behavior. A possible explanation is, at moderate distances, scattering deflects more energy from the upper mantle into the crust, raises the concave part of the decay curve. At larger distances, scattering along the upper mantle channel effectively attenuates the Pn energy offseting the upward increase of the decay curve at large distances. The combined effect makes a more uniform rate of decay, but it is not the frequency-independent case as found for a conical head wave.

Figure 46 compares Pn wave spectral amplitudes calculated from random velocity models having the same upper mantle velocity gradients of 0.001, the same rms velocity perturbation of 1%, but different horizontal and vertical correlation lengths. Panels (a) to (f) are for spectral amplitudes at 0.4, 0.8, 1.5, 3.0, 6.0 and 10.0 Hz. The open triangles, squares and circles are for models with correlation lengths 10 km x 3 km, 20 km x 6 km and 40 km x 10 km, respectively. The solid squares are for related background velocity model. Within the investigated frequency band, the Pn wave is weakly dependent on the size and aspect ratios of heterogeneities. The perturbations with horizontal and vertical correlation lengths of 10 km and 3 km cause more scattering.

Approved for public release; distribution is unlimited.

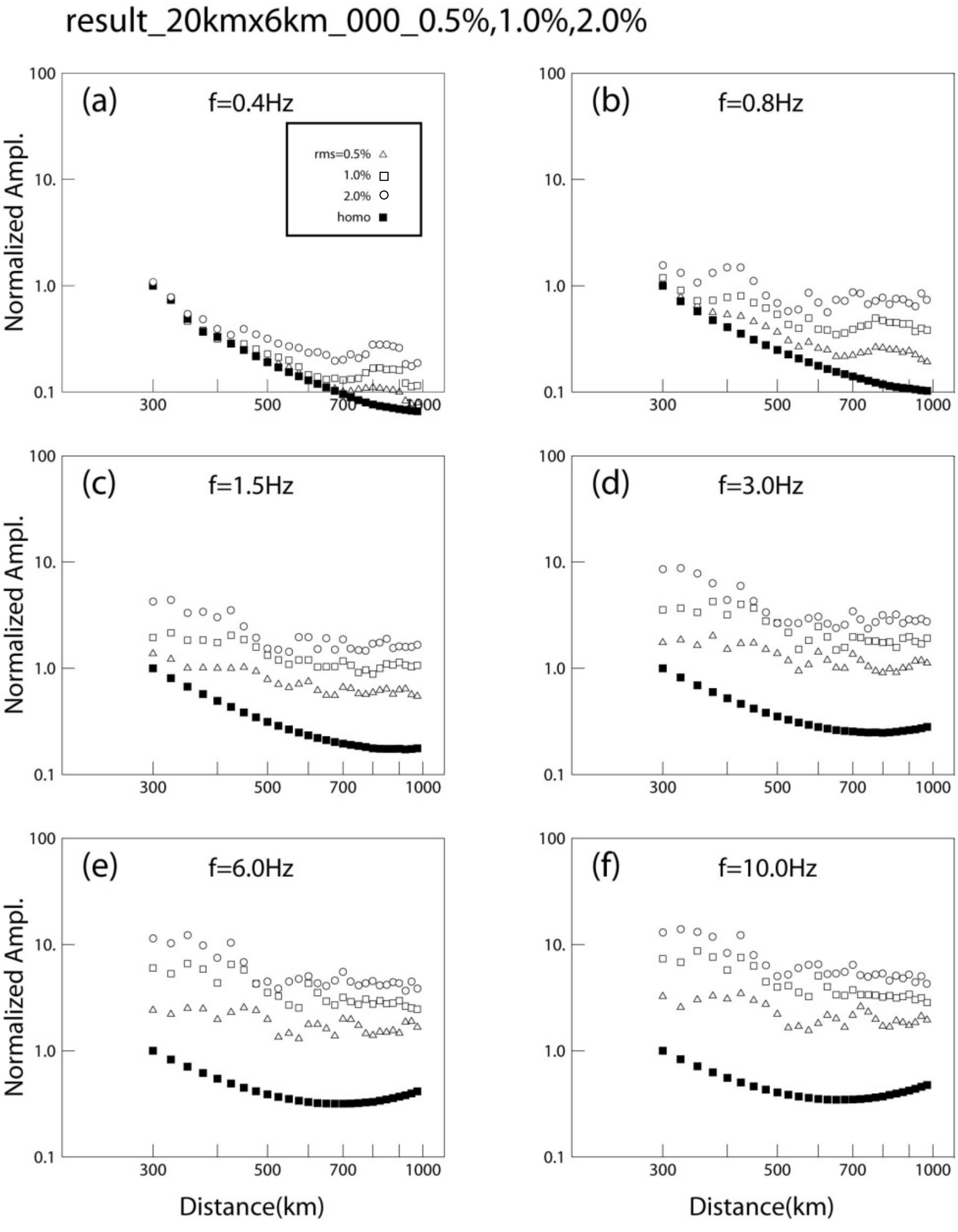

Figure 44. Comparison between Pn wave spectral amplitudes calculated from random velocity models No 1, 2, and 3 in Table 4. These models have the same velocity gradient and random parameters except the rms velocity perturbations are 0.5%, 1.0% and 2.0%. (a) to (f) are for spectral amplitudes at individual frequencies. Open triangles, squares and circles are for models with 0.5%, 1.0% and 2.0% velocity perturbations. The solid squares are for the background model.

Approved for public release; distribution is unlimited.

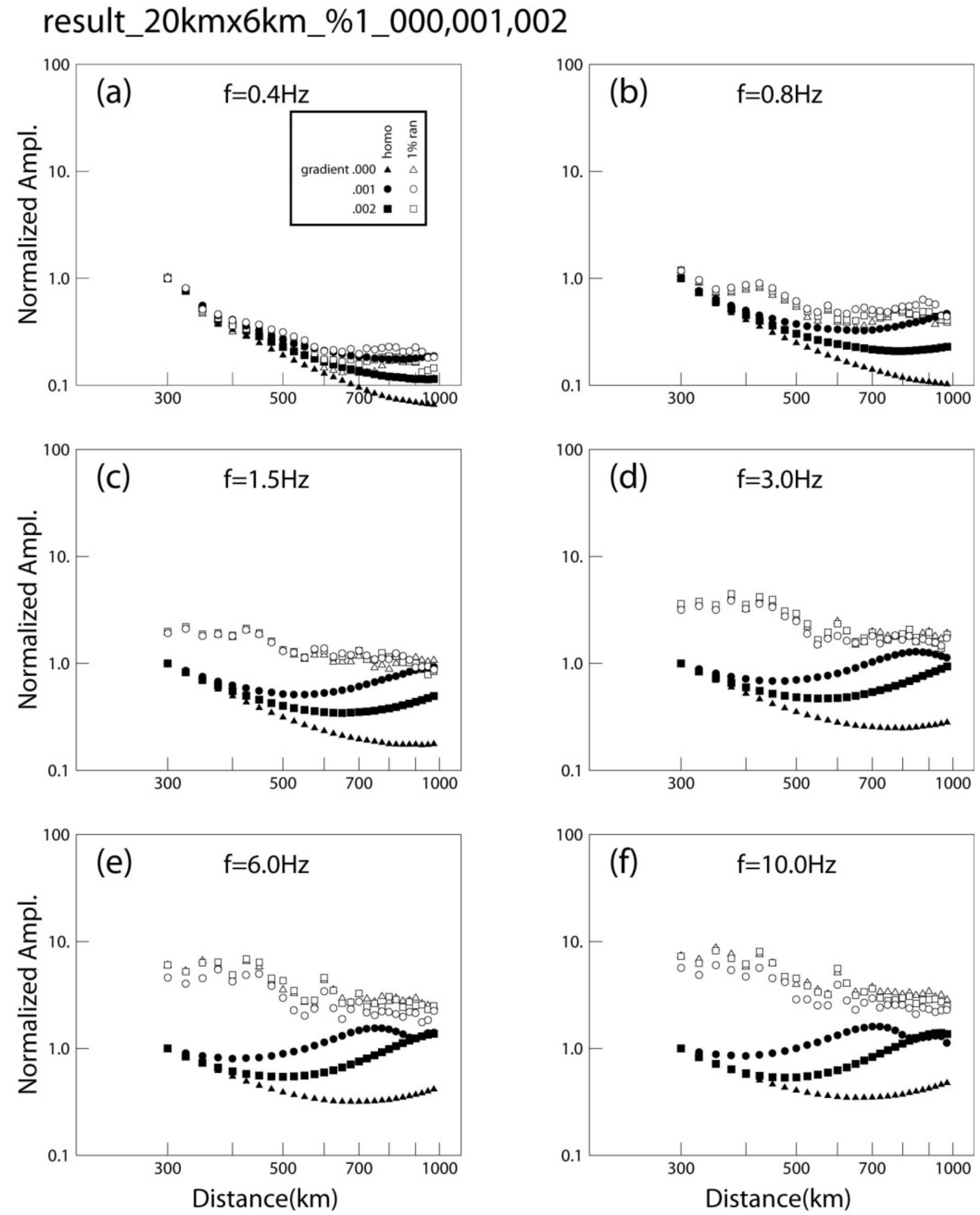

Figure 45. Comparison between Pn wave spectral amplitudes calculated from random velocity model No 2, 5, and 6 in Table 4. These models have the same horizontal and vertical correlation lengths 20 km and 6 km, and rms velocity perturbation of 1%, but the velocity gradients are 0.000, 0.001 and 0.002. Panels (a) to (f) are for spectral amplitudes at individual frequencies. Triangles, squares and circles are for models with velocity gradients 0.000, 0.001 and 0.002. The open symbols are for random velocity models. The solid circles are for the related background velocity models.

Approved for public release; distribution is unlimited.

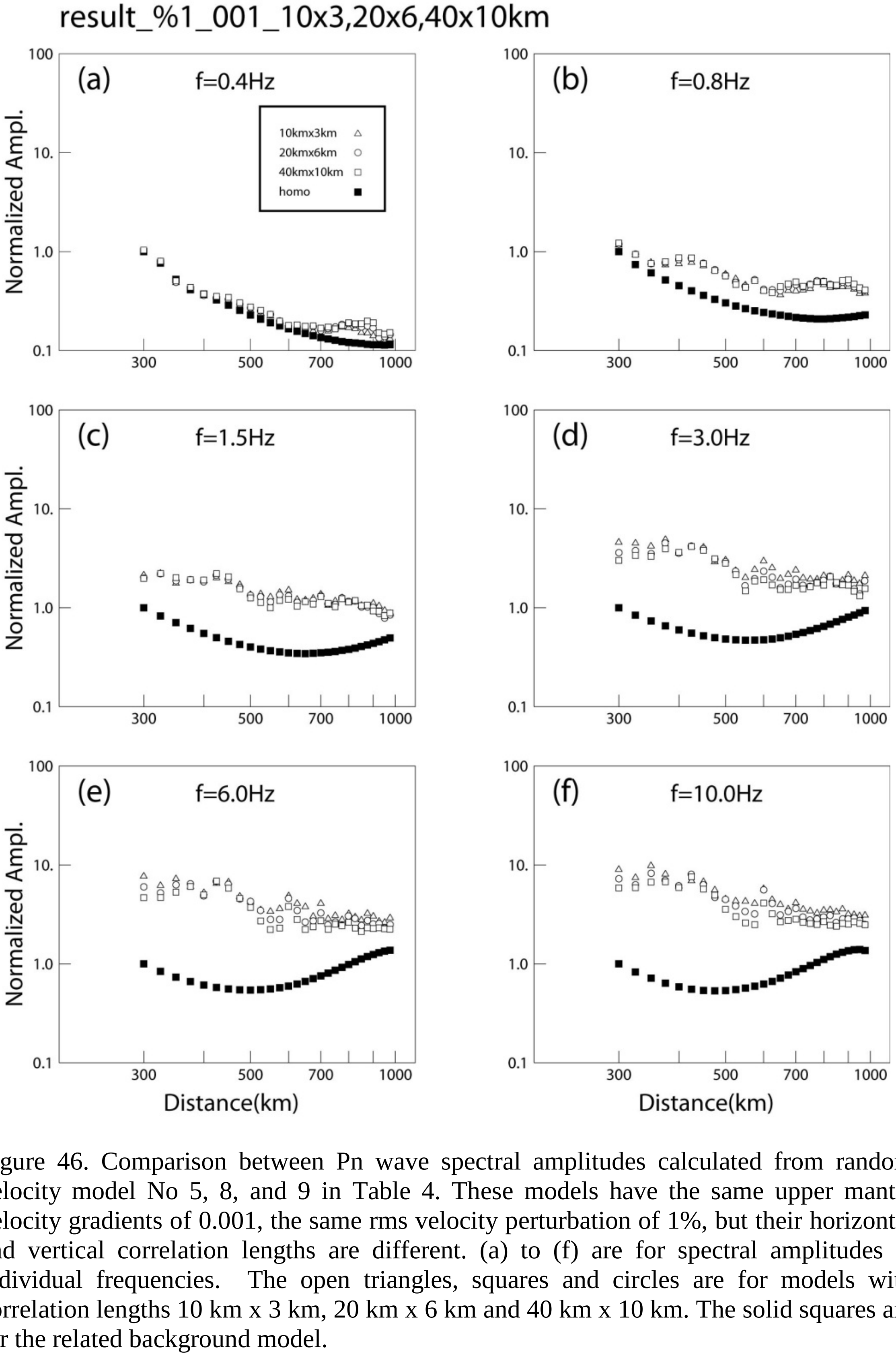

Figure 46. Comparison between Pn wave spectral amplitudes calculated from random velocity model No 5, 8, and 9 in Table 4. These models have the same upper mantle velocity gradients of 0.001, the same rms velocity perturbation of 1%, but their horizontal and vertical correlation lengths are different. (a) to (f) are for spectral amplitudes at individual frequencies. The open triangles, squares and circles are for models with correlation lengths 10 km x 3 km, 20 km x 6 km and 40 km x 10 km. The solid squares are for the related background model.

Approved for public release; distribution is unlimited.

4.6 *Pn Geometric Spreading Functions for Continental and Oceanic Paths*

Pn observations from the North Korean test site and for earthquakes in northeast China have been studied. Appendix 1 reproduces a paper, Zhao et al. (2015), published in *Journal of Geophysical Research*, which was partially supported by this contract. The Pn paths from the North Korean test include continental and oceanic paths that are characterized by very different crust and upper mantle structures, which appear to considerably affect the Pn wave propagation. In this section we present additional modeling of 2D wave propagation along the corresponding paths to supplement the findings given in Appendix 1. There are numerous factors that may contribute to the observed Pn amplitudes, including the crustal thickness, the upper mantle velocity gradient, P-wave attenuation in the uppermost mantle, and scattering along the propagation path, as explored with generic models in the previous sections. When the source and station are located in different environments, the transitional zone between the continental and oceanic structures can also play an important role in Pn-wave propagation efficiency, as suggested by the 2D simulations in section 4.4. We simulate Pn wave propagation along these paths for nuclear tests located in North Korea and compare the model calculations with the observed data.

Shown in Figure 47 are locations of the North Korea nuclear test site (NKTS) and stations providing Pn observations. Pn waves observed in mainland China primarily traverse continental paths, while Pn observations from stations in Japan traverse the Japan Sea, involving primarily oceanic paths. Given that the explosion sources are virtually isotropic and the observations span a large azimuth range, Zhao et al. (2015) compared the Pn spectral amplitudes along the combined continental and oceanic paths at 1000 km epicentral distance (recorded by those stations near the large circle in Figure 47). After removing the Pn-wave source excitation functions, the spectral amplitudes are presented in Figure 48 as a function of azimuth from the source, with different symbols indicating spectral amplitudes from three NKT explosions. The black, blue and red colors indicate 0.8, 7.0 and 10.0 Hz data. Solid circles with error bars indicate their mean values and standard deviations obtained within 30º azimuth windows. Prominent differences can be observed for Pn waves along different paths. For azimuths from 60º to 180º, the Pn signals crossing the oceanic path are strongly frequency dependent, with extremely low high-frequency amplitudes. For azimuths between 230º and 280º, the wave paths are through continental China, and the low-frequency content (0.8 and 7 Hz) is similar to that along the oceanic paths, but the high-frequency (10 Hz) propagation is much more efficient than for the oceanic paths. The geometric spreading function tends to raise the high-frequency signal, whereas attenuation tends to reduce the high-frequency content. The detailed structure of transition zones may also affect the frequency dependence.

Approved for public release; distribution is unlimited.

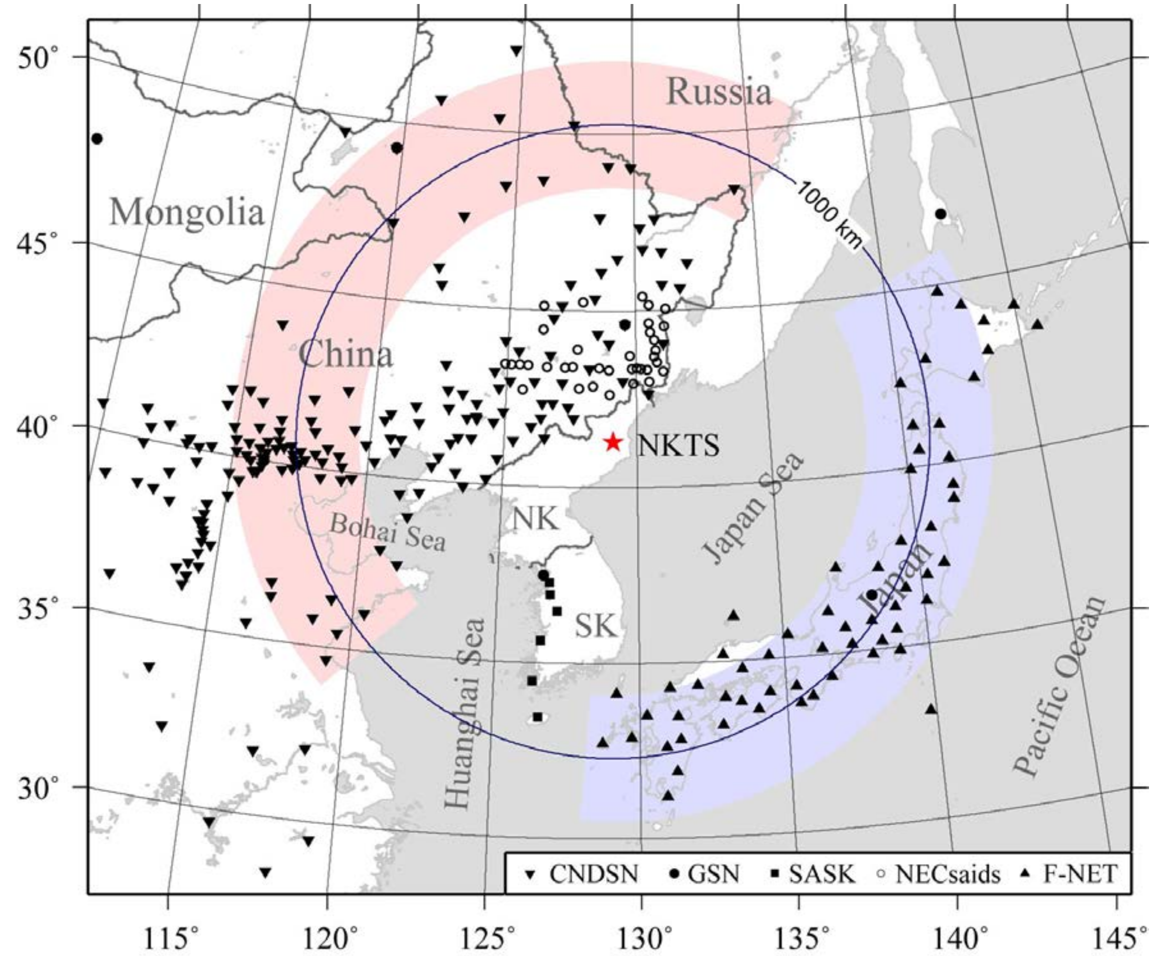

Figure 47. Map depicting locations of the North Korean test site (red star labeled NKTS) and seismic stations at which Pn phase measurements were made. The stations located near the large circle have nominal epicentral distance of 1000 km from the NKTS, with the pink and blue colors indicating the Pn waves that traverse primarily continental or oceanic paths, respectively. (Zhao et al., 2015 – Appendix 1).

To simulate the propagation of Pn waves in oceanic and continental structures, we designed a Japan Sea model as shown in the top panel in Figure 49. The depth of the Moho discontinuity is obtained from CRUST1.0 (Laske, et al., 2013) by using a typical Pn path. In this model, the crust beneath the NKTS is approximately 33 km, and under the Japan Sea is approximately 11 to 15 km. On the NKTS side, the crustal thickness quickly decreases from 33 km to about 10-12 km over approximately 100 km distance, forming a steep reduction in depth of the Moho discontinuity. On the side of the Japan Islands, the crustal thickness increases relatively slowly, forming a broad dip in the Moho discontinuity. For continental path, we use a simple 1-D model with a 30 km flat Moho (bottom panel in Figure 49). In both models, the upper mantle velocity gradient is set to be zero, and the water column is not included in the model.

Approved for public release; distribution is unlimited.

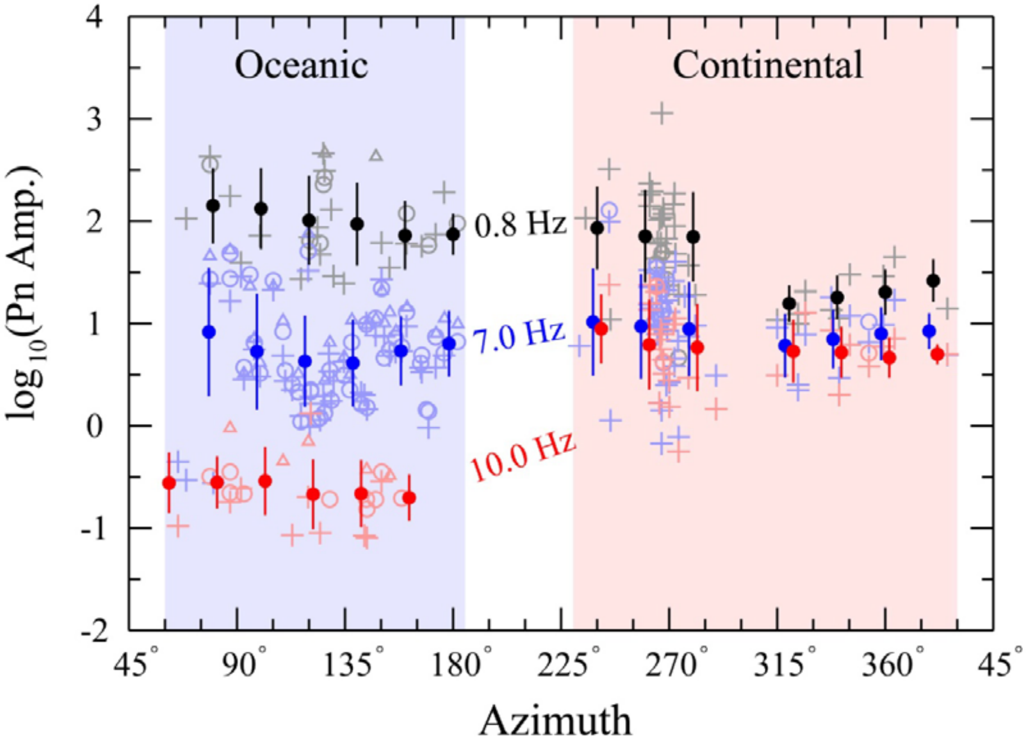

Figure 48. Pn spectral amplitudes measured from stations near a distance of 1000 km versus azimuth (Figure 47). Different symbols are amplitudes from the three North Korea nuclear tests. Black, blue and red colors indicate 0.8, 7.0 and 10.0 Hz measurements. Solid circles with error bars represent their mean values and standard deviations, obtained within 30-degree azimuth windows. The Pn source excitation functions are removed from the data. (Zhao et al., 2015 – Appendix 1).

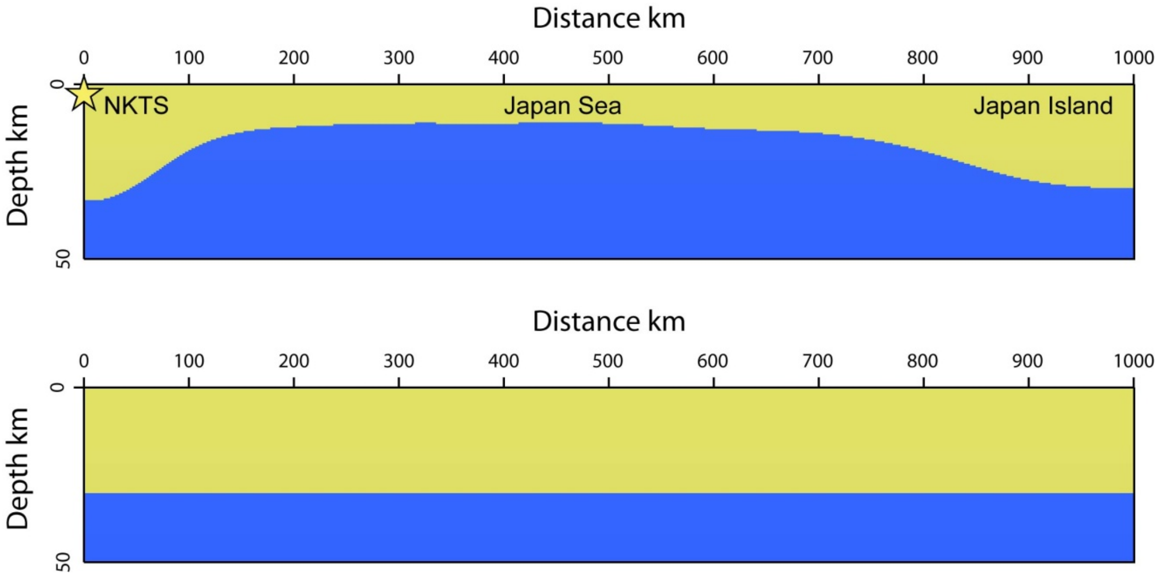

Figure 49. Crust-upper mantle models for Pn-wave simulation. Top: a typical profile from the NKTS to Japan Island passing the Japan Sea. Bottom: a 30 km thick crust model for typical continental path. To show the details, the vertical coordinate is exaggerated.

To calculate the synthetic seismograms, we use the same source time function as used in the previous calculations. However, we set the source depth at 1 km. Shown in Figure 50 are wavefield snapshots for the entrance section near the NKTS (from 50 km to 350 km) of the Japan Sea model. Shown in Figure 51 are wavefield snapshots for the Japan Island side (from 650 km to 950 km). Shown in Figures 52 and 53 are similar snapshots for Pn waves in the continental model which has a 30 km thick crust. A shallowing Moho tends to allow more energy from the source to penetrate into the upper mantle, while a deepening Moho allows more energy to come back from the upper mantle into the crust. Aside from any intrinsic attenuation, these conditions favor Pn wave traversing the Japan Sea model compared to transmission along a flat continental path. This can also be understood by comparing velocity models in Figure 49, where the varying dip of the Japan Sea Moho is equivalent to an additional curvature relative to the 1-D model. Figure 54 compares the Pn waves in both models when they approach 1000 km distance. It is evident that in the Japan Sea model Pn is stronger than in the continental model.

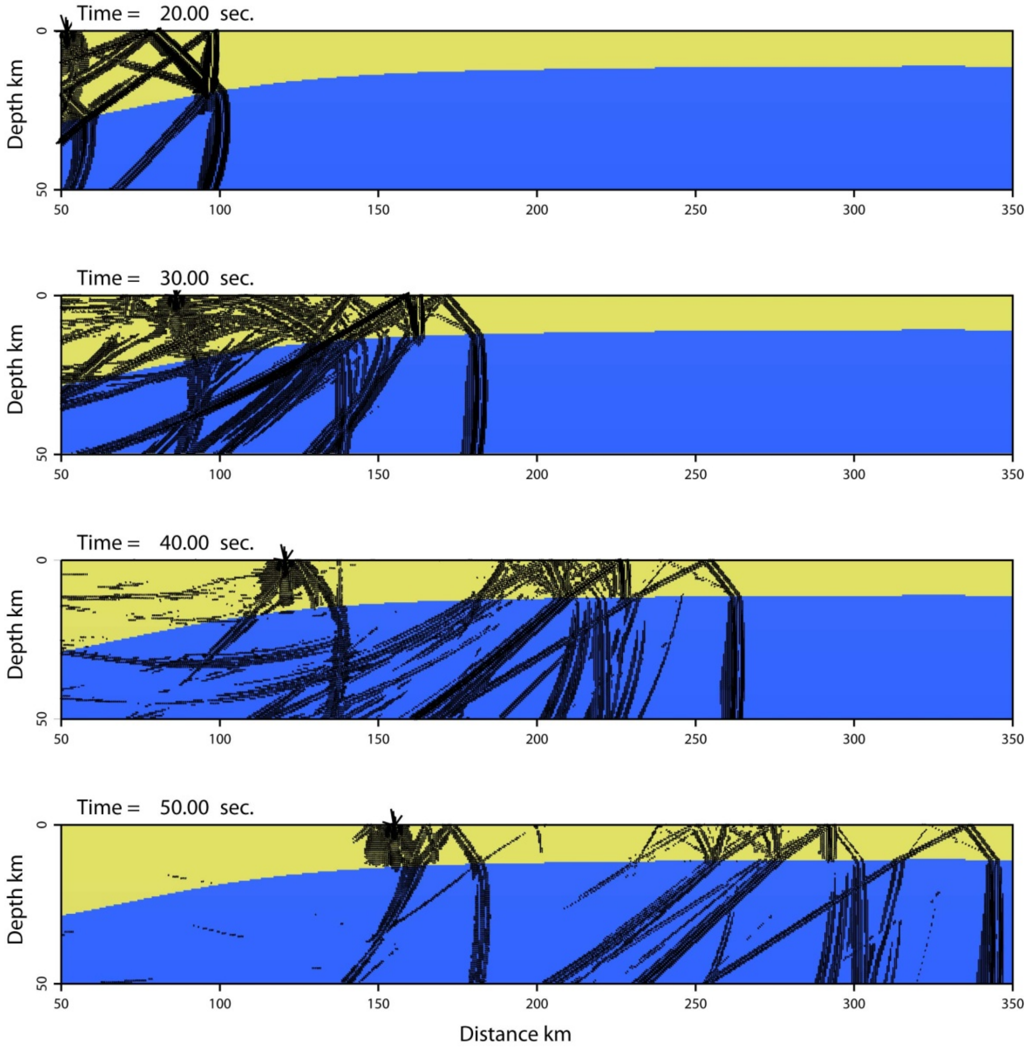

Figure 50. Wavefield snapshots of Pn waves propagating in the entrance section near the NKTS (50 – 350 km) of the Japan Sea model.

Approved for public release; distribution is unlimited.

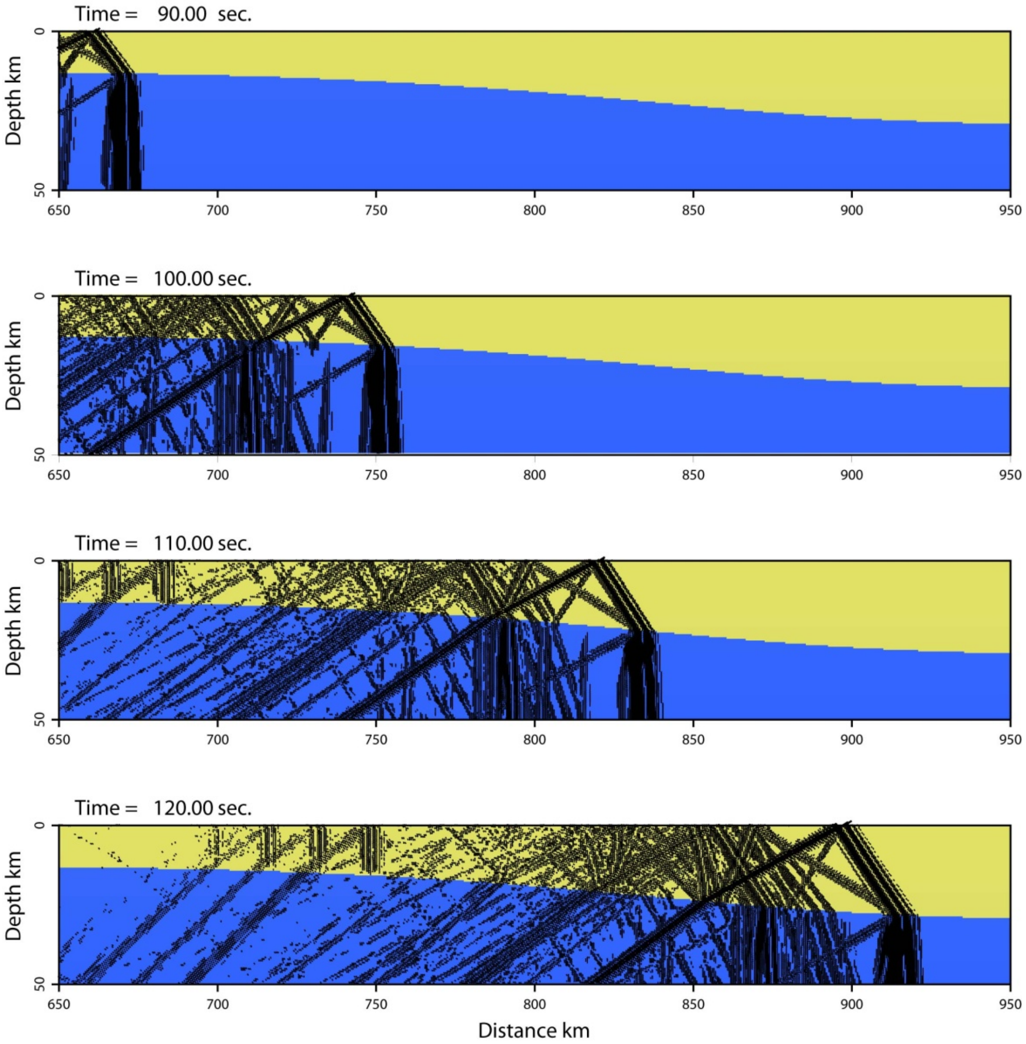

Figure 51. Wavefield snapshots of Pn waves propagating in the exit section approaching the Japan receivers (650 – 950 km) of the Japan Sea model.

Approved for public release; distribution is unlimited.

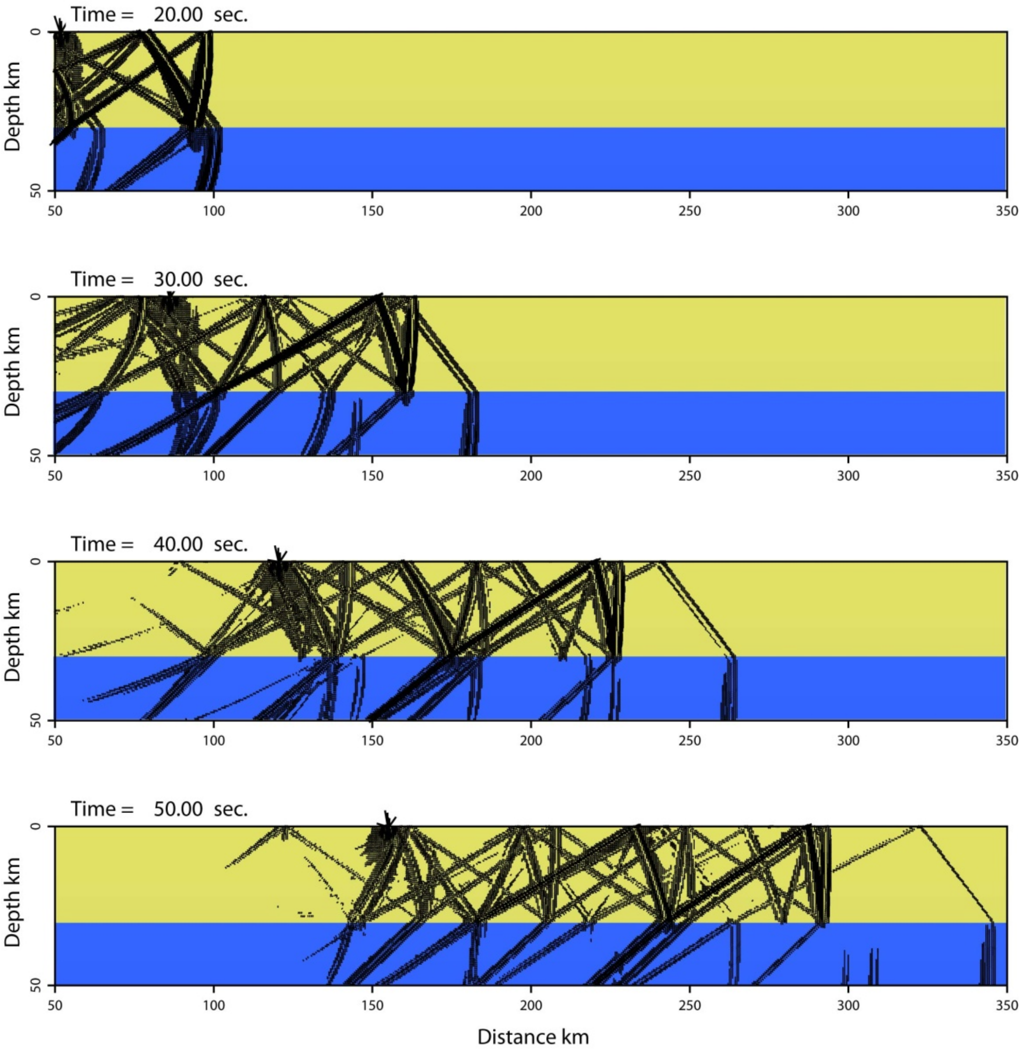

Figure 52. Wavefield snapshots of Pn waves propagating in the entrance section (50 – 350 km) of the 1-D model with a 30 km thick crust.

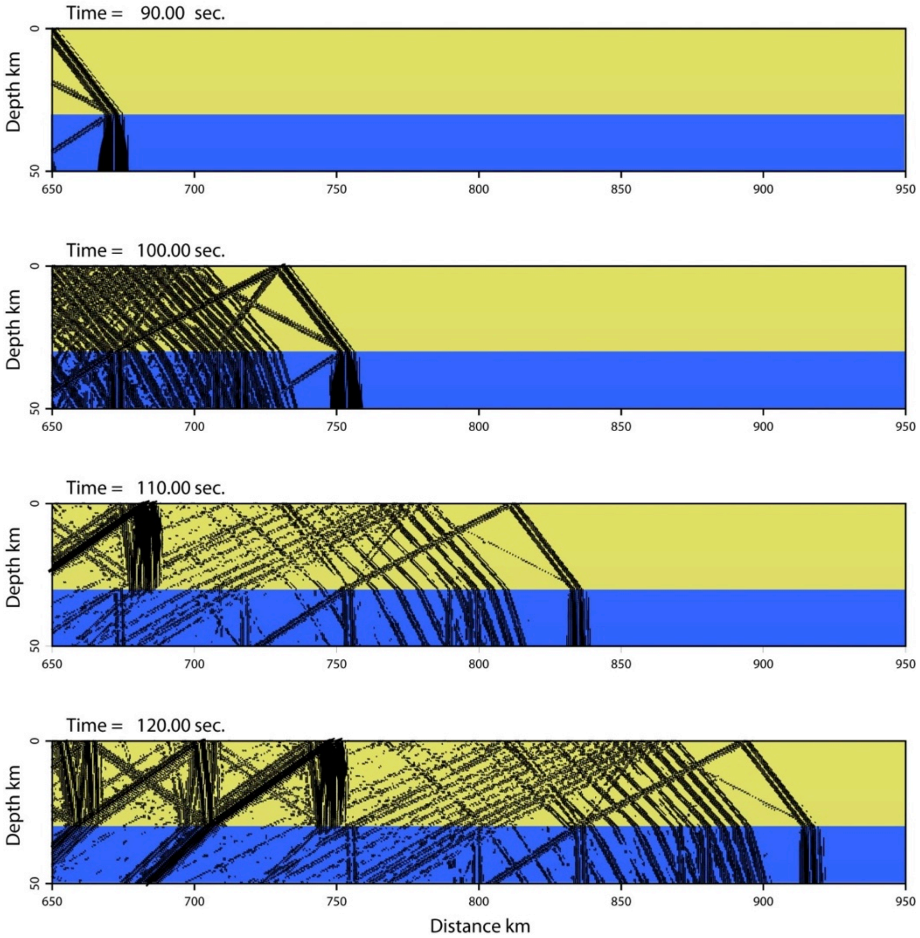

Figure 53. Wavefield snapshots of Pn waves propagating in the exit section (650 – 950 km) of the 30 km thick crust model.

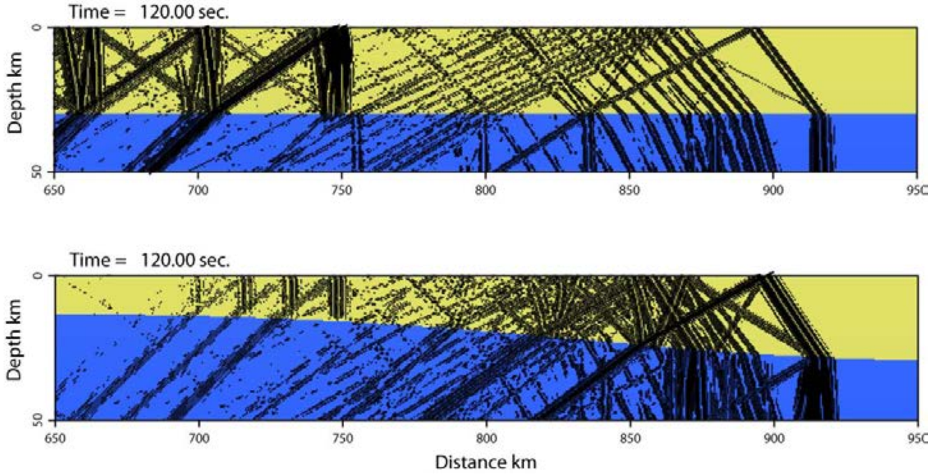

Figure 54. Comparison between Pn waves propagating in the continental and Japan Sea models between 650 and 950 km. Note that the Pn wave amplitude is stronger in the Japan Sea model.

Approved for public release; distribution is unlimited.

Figure 55 shows the synthetic seismograms for both the Japan Sea model and the flat continental model, where from left to right are the Japan Sea velocity model, synthetics for the Japan Sea model and synthetics for the continental model. The Pn wave amplitude is much stronger in the Japan Sea model. Because the Pn wave penetrates the low-velocity crust with laterally varying thickness, its travel time curve deviates from a straight line. The vertical markers on the seismograms indicate the group velocity windows used to measure the rms amplitude. The frequency dependent Pn amplitudes versus distance are illustrated in Figure 56, where the diamonds are for the Japan Sea model, crosses are for a 30 km thick flat crust model, and plus signs are for a 10 km thick flat crust model. It is evident that the crustal thickness does not affect the Pn amplitude much. However, the Pn amplitudes in the Japan Sea model are stronger than those in flat Moho models. These differences are frequency dependent. At lower frequencies, the difference is less than a half order of magnitude, but it increases to about an order of magnitude at higher frequencies. It appears the deepening Moho on the Japan Island side also plays an important role in changing the Pn wave amplitudes. At lower frequencies it raises the Pn amplitudes. For higher frequencies, its effect is complicated.

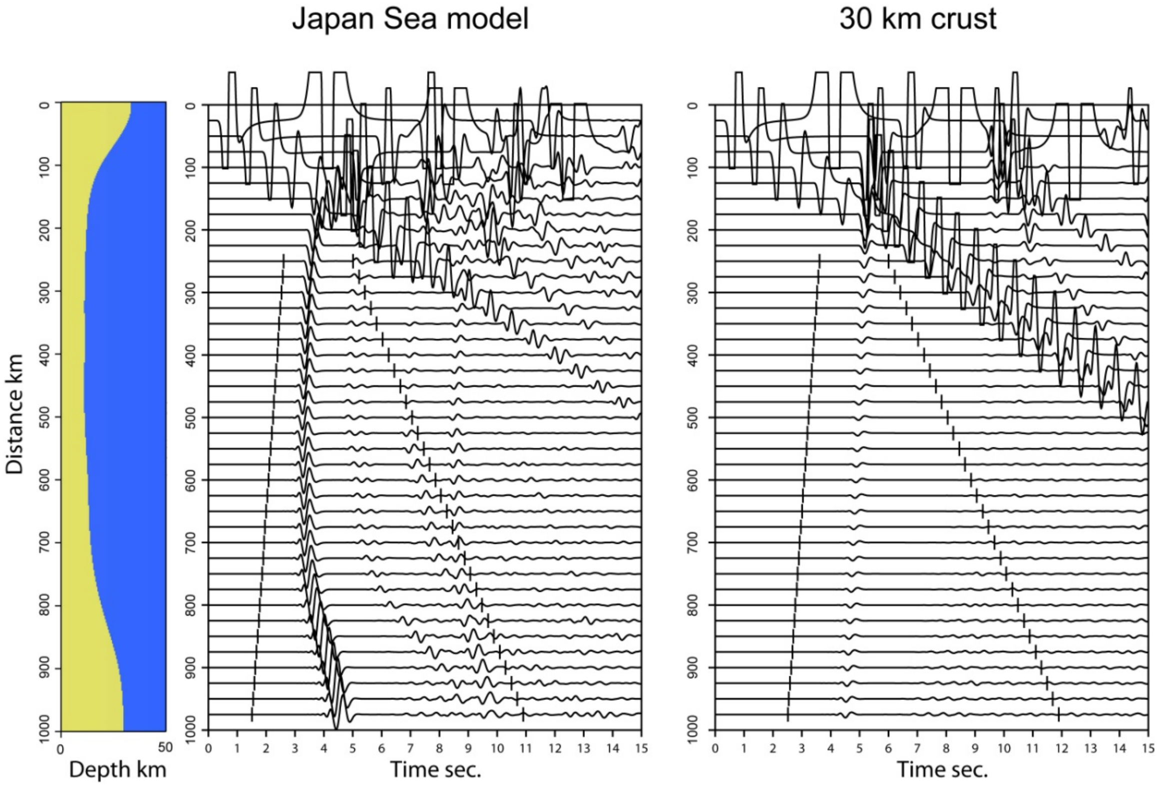

Figure 55. Comparison between synthetic seismograms in the Japan Sea model and a 1-D continental model with a 30 km thick crust. Left: Japan Sea velocity model, middle: synthetic seismograms in Japan Sea model, and right: synthetic seismograms in the model with a 30 km thick crust. The vertical markers indicate the group velocity windows used to measure the rms amplitude.

Approved for public release; distribution is unlimited.

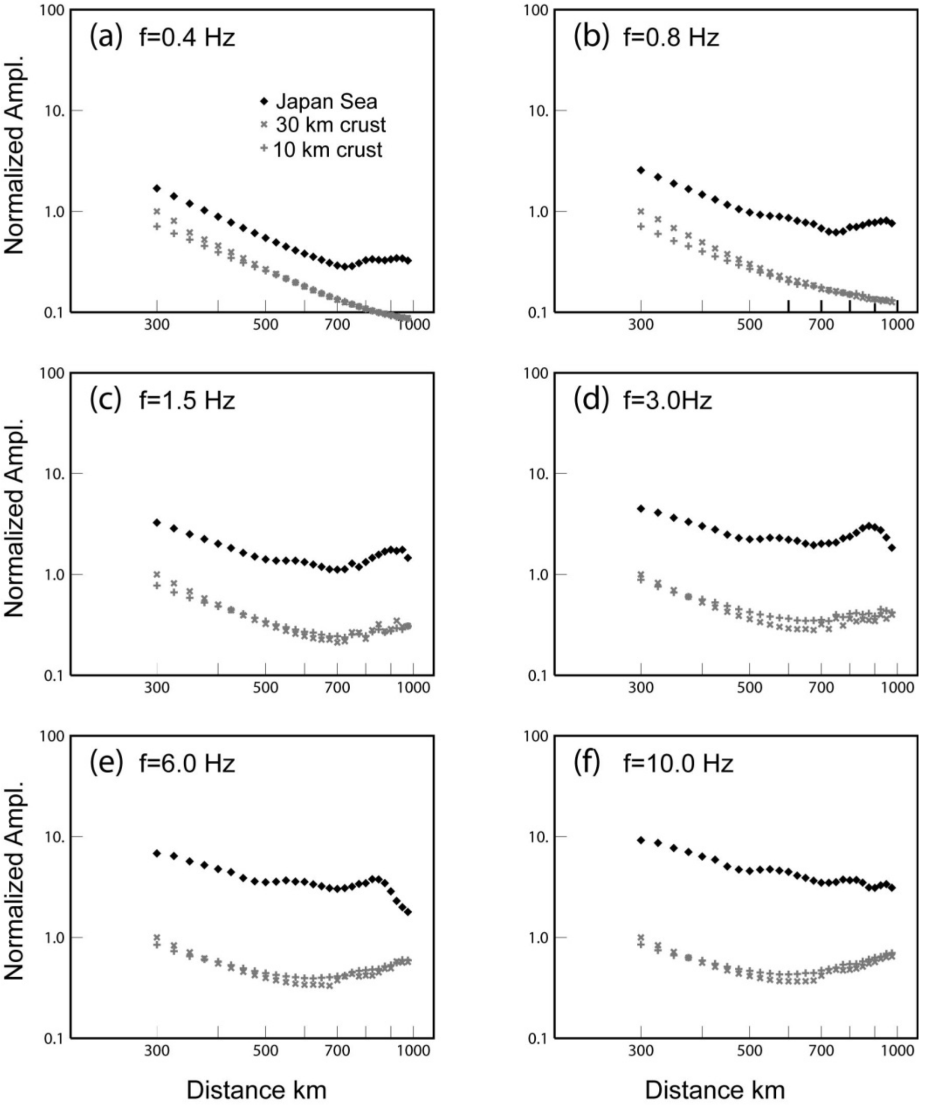

Figure 56. Frequency dependent amplitude versus distance for the Japan Sea model (diamond), 30 km crust (cross) and 10 km crust (plus sign) models.

Given that the oceanic dataset is mostly observed in Japan over a narrow distance range at approximately 1000 km distance, we cannot compare Pn amplitude variations versus distance with our simulations. Instead, we investigate the observed frequency dependence of Pn wave amplitudes at 1000 km. Similar to the measurements shown in Figure 48, we calculate the $A_{Pn-1000km}(f)$ from the NKTS dataset. Figure 57 shows spectral amplitudes for both the oceanic path through the Japan Sea and the continental path through mainland China. At lower frequencies, Pn waves from both paths have similar amplitudes. However, at higher frequencies, the Pn waves traversing the Japan Sea path are much weaker than on continental paths towards mainland China. We know that the geometric spreading tends to raise the high frequency signal while the attenuation tends to decrease the high frequency signal. By comparing the numerical simulations of Pn wave

Approved for public release; distribution is unlimited.

geometrical spreading (Figures 55 and 56) and the observations from the NKTS data (Figure 57), we see that, even though the geometric spreading in the Japan Sea model appears very efficient, the observed Pn amplitudes at high frequency through the Japan Sea is weaker. This suggests that the P wave propagation in the uppermost mantle beneath the Japan Sea must be more attenuating than that under the continental crust. To compare with the observed Pn wave spectra, we combine Pn Q models with the calculated geometrical spreading functions. For Pn waves from the NKTS to continental stations, Zhao et al. (2015) obtained a model of $Q_{Pn} = 237 f^{0.36}$, which will be used for the continental path. For the oceanic model, using a trial and error method, we find a lower Q_0 and a slightly higher η giving a Pn Q model of $Q_{Pn} = 150 f^{0.40}$ for the Japan Sea. The resulting Pn wave amplitudes are shown in Figure 58. The predictions are consistent with the observed data shown in Figure 57. As discussed above, there are many factors affecting the Pn wave amplitude and its frequency dependence. Thus, this result is not unique. However, it provides some constraint on the P wave attenuation beneath the oceanic crust.

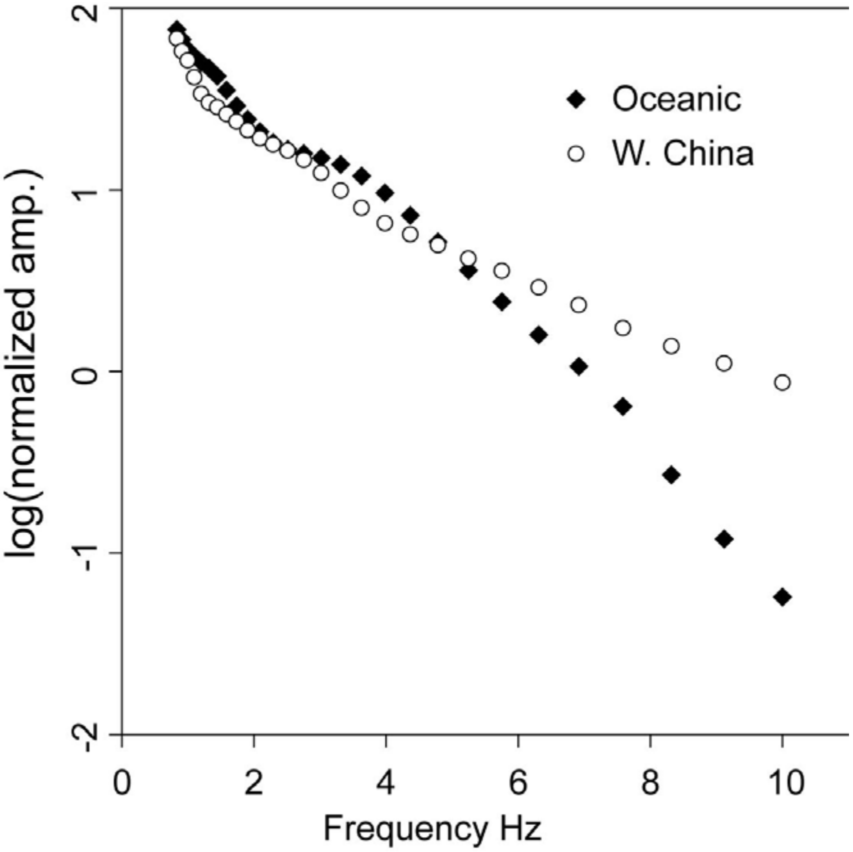

Figure 57. Observed Pn wave amplitudes, at 1000 km distance from the NKTS, versus frequency. Solid diamonds are for paths traversing the Japan Sea, and open circles are for paths traversing continental structure to Northwest China. Pn waves through these two paths show apparently different frequency dependence.

Approved for public release; distribution is unlimited.

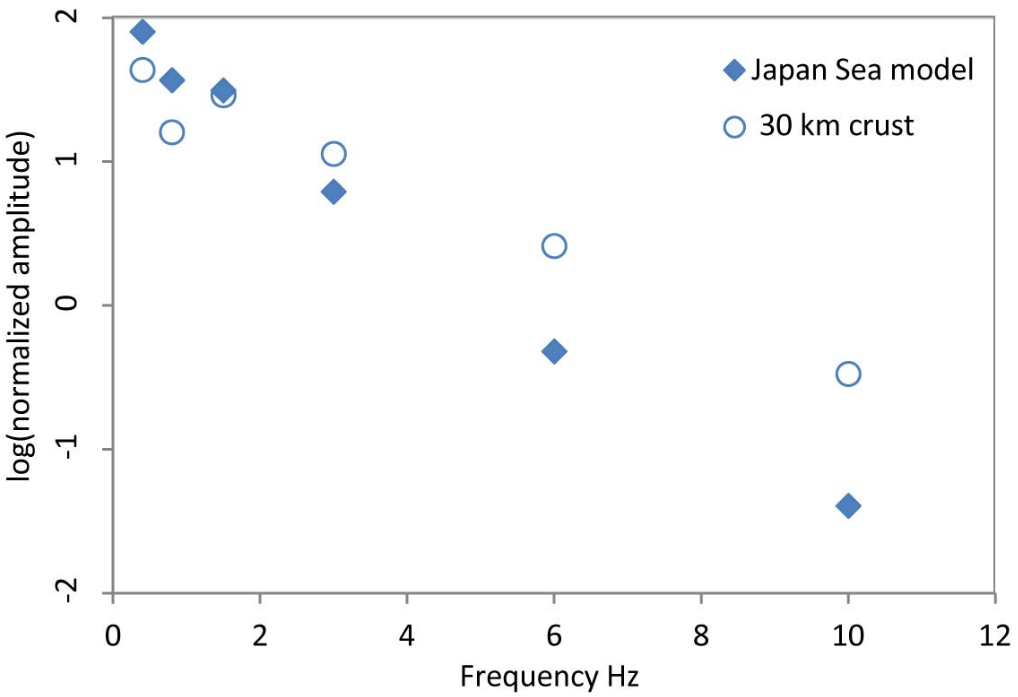

Figure 58. Computed Pn wave amplitudes at 1000 km distance from the NKTS versus frequency. Solid diamonds are for the Japan Sea model, and open circles are calculated in the 30 km thick crustal model for the continental path. The results are obtained by combining the calculated geometrical spreading with Pn Q models. For the continental model, the Pn Q model $Q_{Pn} = 237 f^{0.36}$ (Zhao et al., 2015) is used. For the Japan Sea model, a Pn Q model of $Q_{Pn} = 150 f^{0.40}$ is used.

4.7 *Use of RSTT Models and Empirical Models for Pn Spreading for Eurasian Data*

In working toward self-consistent use of velocity models for predicting regional phase travel times and regional phase geometric spreading, we empirically examined the use of regionalized corrections for Pn amplitudes guided by RSTT regional velocity models and by empirical analysis of Pn data with constraint of realistic spreading behavior as established by Yang (2011). Figure 59 displays the regionalization guided by RSTT models. It would be a major computational effort to compute the fully 3D models for each region to evaluate Pn spreading, and the results of earlier sections have established that laterally varying gradients and crustal thickness produce directionally-dependent path corrections, so comparisons with data are very complex and essentially one would have do to a path-by-path treatment. This is unwieldy, and we adopt a simplified procedure for evaluating whether such an approach is even warranted. The RSTT models are obtained from noisy and limited data sets that provide only limited constraint on mantle velocity gradients (sometimes they may capture true travel time curvature and constrain the gradient, but in most cases the data are too noisy and/or sparse to really resolve actual lid velocity gradient. Our approach is to explore first-order variations in structure inferred from the RSTT model variations.

Approved for public release; distribution is unlimited.

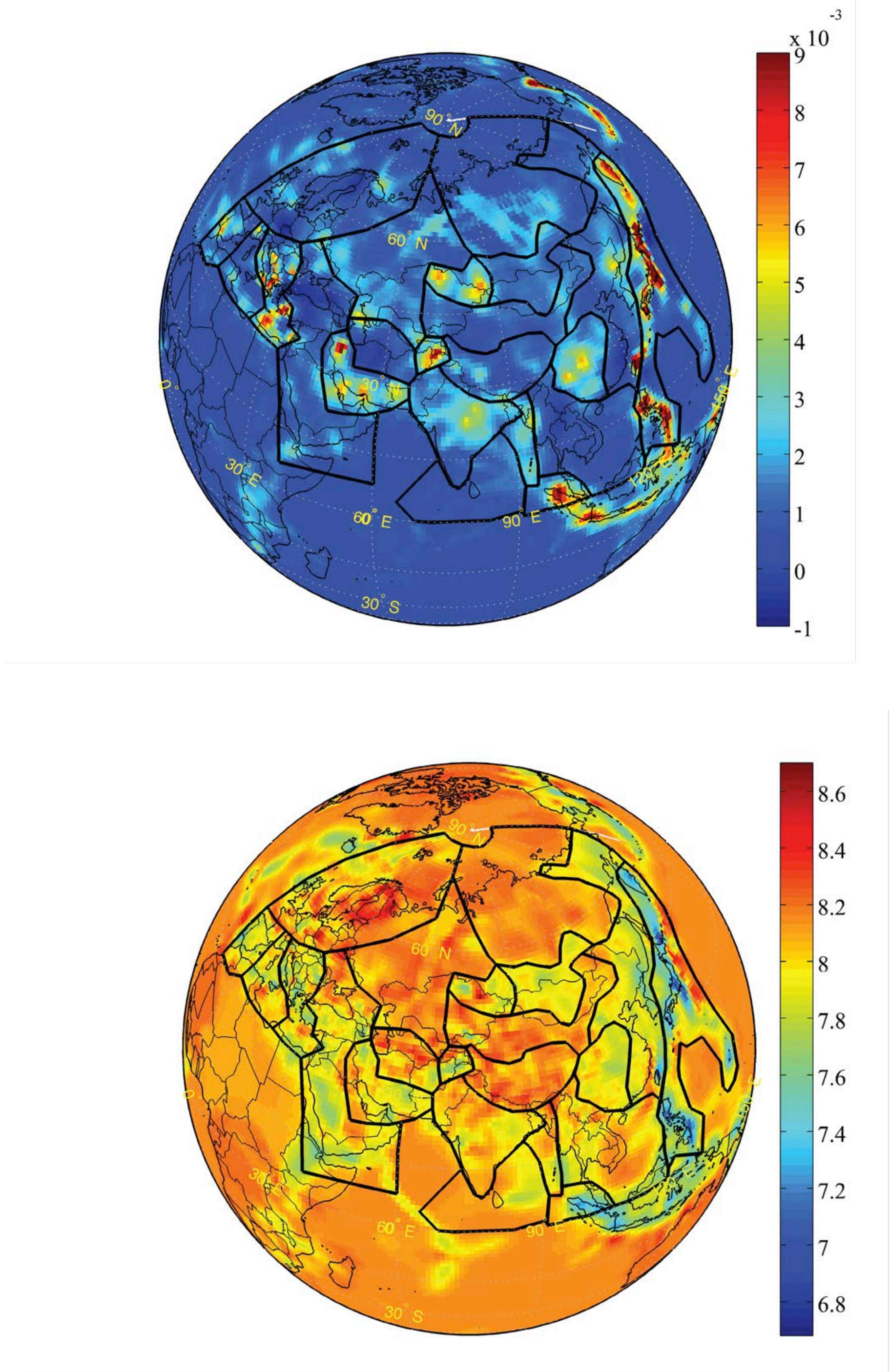

Figure 59. RSTT model lid velocity gradients (top) and average Moho P velocity (bottom) with a superimposed grid developed to define provinces of similar parameters.

The LANL database for Pn measurements (Figure 60) is used to extract signals and measured Pn amplitudes in varying passbands to define the sampling of regions (Figure 61) for which RSTT mantle lid gradient and/or average Moho velocity are relatively uniform, or at least we approximate with a regional 1D structure.

Approved for public release; distribution is unlimited.

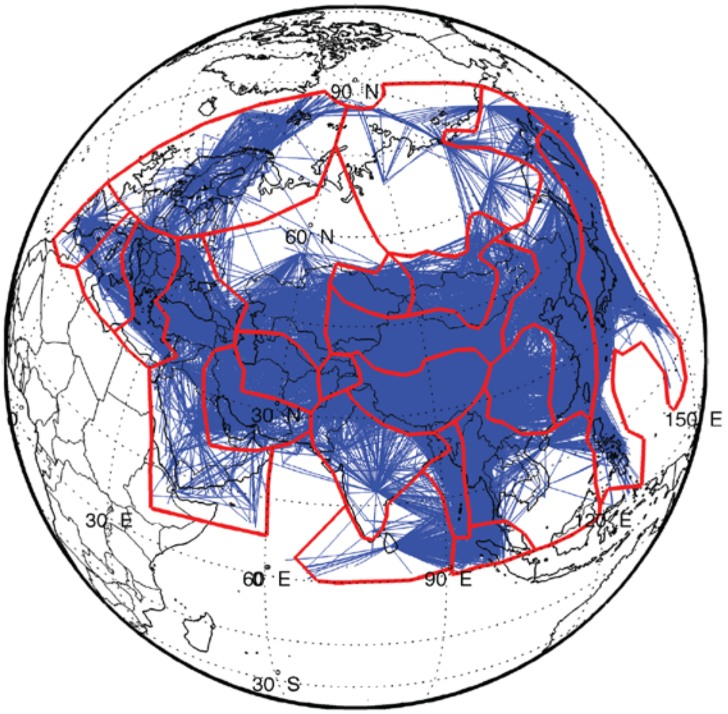

Figure 60. LANL Eurasian Pn data base coverage showing Pn paths sampling the RSTT-based regionalization.

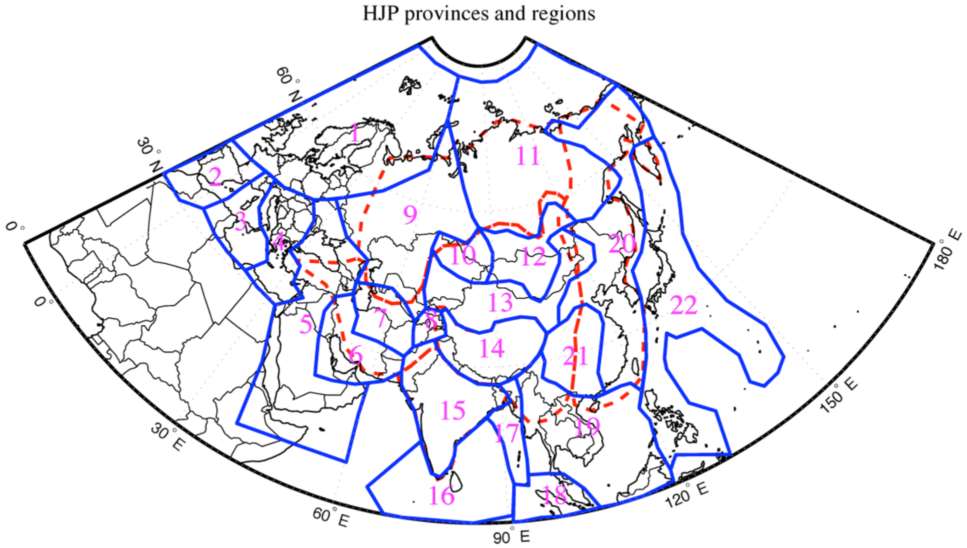

Figure 61. Regional numbering scheme for the RSTT-based subdivision. Pn observations in each region have been evaluated. Model spreading parameters for each RSTT structure have been determined.

For each region identified in Figure 61, we computed spreading behavior for a 1D average of the local RSTT model using wavenumber integration, and applied corresponding frequency-dependent geometric spreading corrections to the MDACcorrected Pn observations for that region. We also applied simple power-law spreading corrections for a power of -1.1, and we determined region-specific spreading corrections following the procedure of Yang (2011). This gave three sets of corrected Pn data for each region. Plotting these sets of corrected Pn amplitudes (log10) as functions of distance, allows an estimation of the average Q for that region for each frequency. We display results for regions 4 and 13 (Figure 61) in Figures 63a,b and 64a,b, respectively.

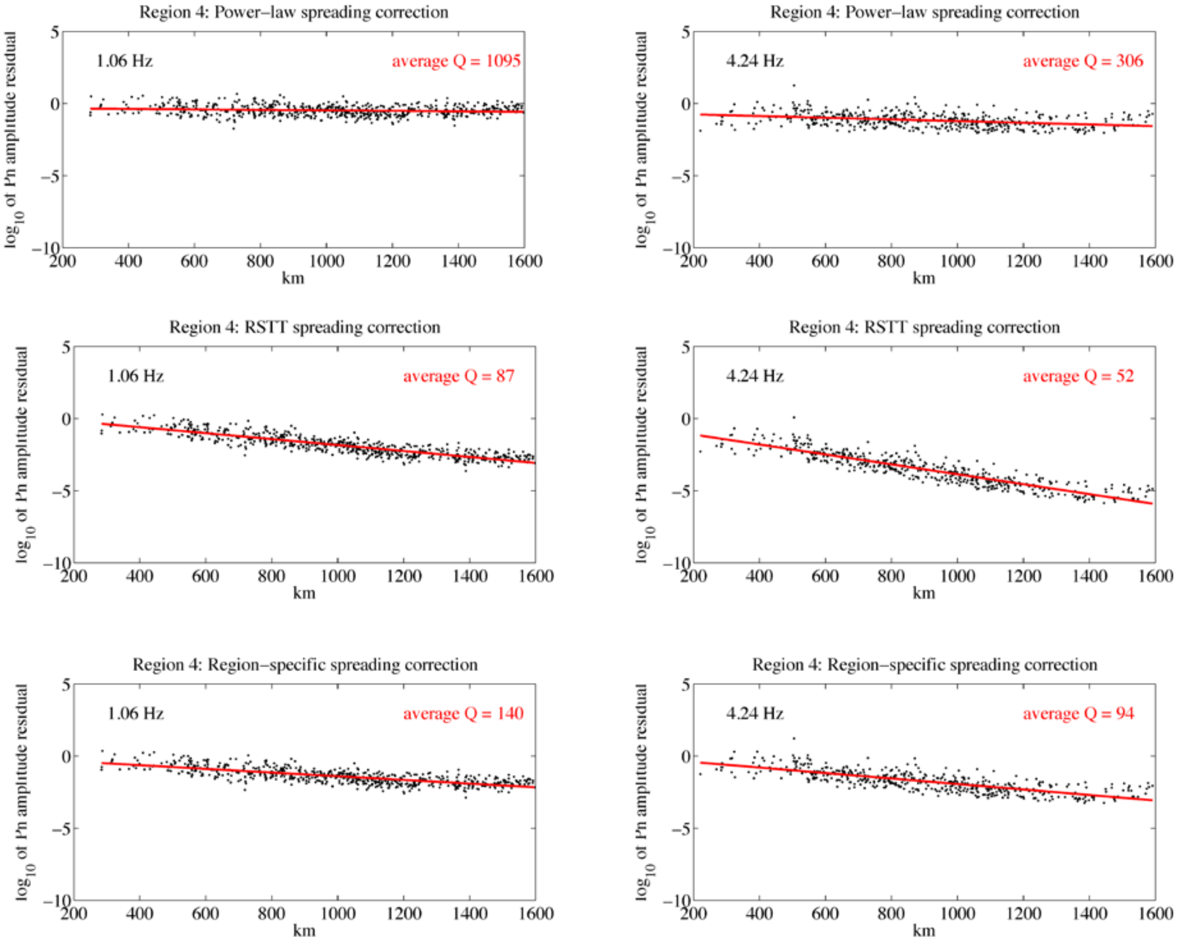

Figure 62a. Pn amplitudes versus distance for Region 4 with corrections using a power-law (top row), RSTT-based synthetic computations (middle row) or empirical region-specific corrections following the procedure of Yang (2011) (bottom row) for passband center frequencies of 1.06 Hz (left) and 4.24 Hz (right). The measured average Q for each case obtained from the regression curve is indicated in the upper right.

Each set of geometric spreading corrections results in relatively smooth linear amplitude versus distance trend that suggests a corresponding average Q for that frequency. However, the Q values that are inferred vary dramatically, depending on the geometric spreading used.

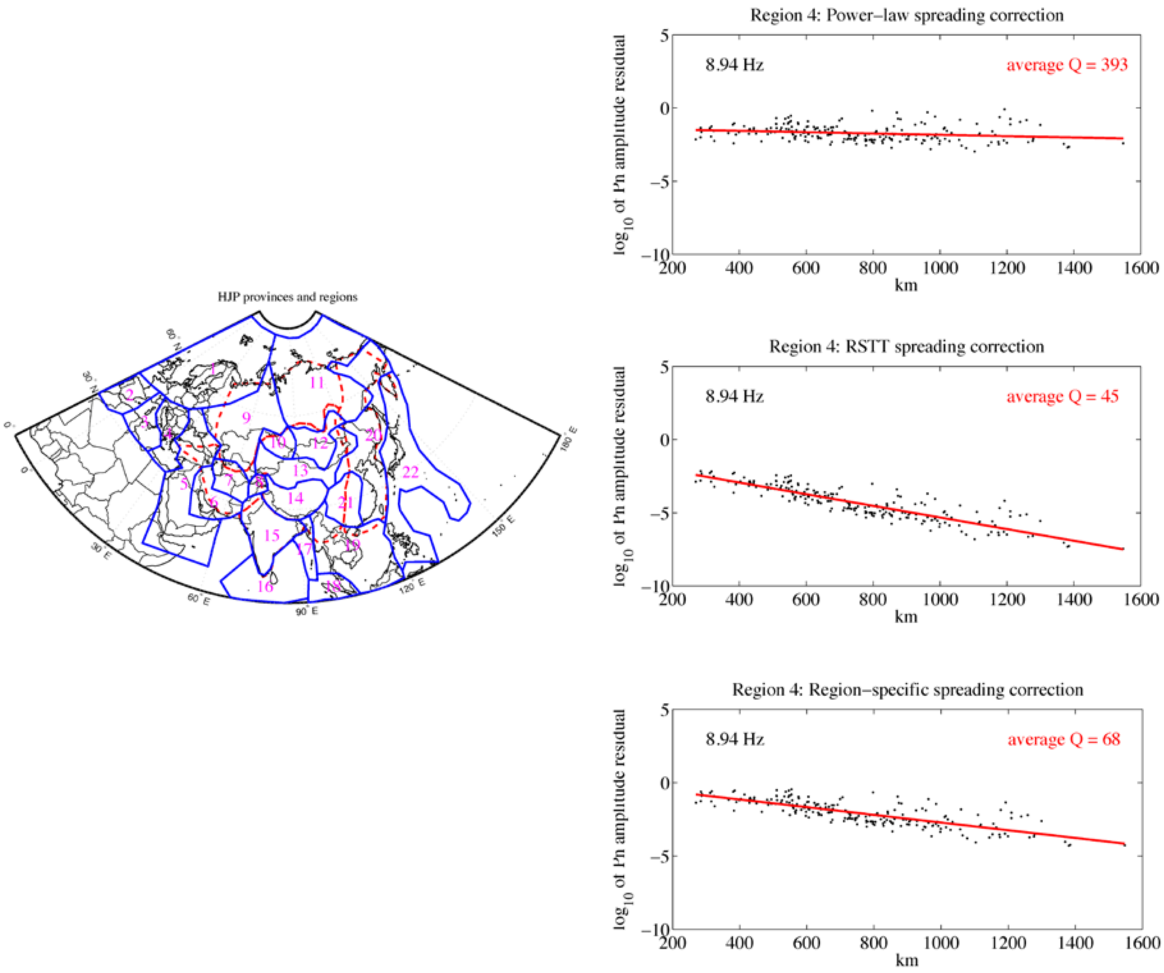

Figure 62b. Pn amplitudes versus distance for Region 4 (map inset) with corrections using a power-law (top row), RSTT-based synthetic computations (middle row) or empirical region-specific corrections following the procedure of Yang (2011) (bottom row) for passband center frequency of 8.94 Hz (right). The measured average Q for each case obtained from the regression curve is indicated in the upper right.

In general, as found by Yang et al. (2007) and Yang (2011), use of a 'standard' power-law spreading correction with an exponent of -1.1 that does not vary with frequency (and for which there is no specific known structure) gives high Q values in every case, and even negative Q value for Region 13 at 1.06 Hz. For Region 4, the RSTT velocity gradient is relatively high (0.0026 s^{-1}) while for Region 13 it is average value (0.0012 s^{-1}). In both cases, the addition of the EFT gradient of 0.0013 s^{-1} gives positive velocity gradients that produce strong frequency-dependent Pn amplitude corrections. The data have somewhat less scatter and systematically lower Q values are inferred for each region using the RSTT based corrections. Q values that are 1.6-1.8 times higher than the RSTT-based results are found for corrections based on the region-specific spreading corrections following Yang (2011). The absolute values and the frequency-dependence of the attenuation parameters are more similar for the RSTT- and regional-based spreading corrections. For these regions there is no clear reduction in scatter to favor a specific spreading model, but the Q

Approved for public release; distribution is unlimited.

values appear to be more reasonable for either of the frequency-dependent spreading corrections results. As long as the Q model for a given spreading model is used, total amplitude calculations will be reasonably similar. The main advantages of using a more appropriate local velocity model to process the amplitudes is that a more reliable Q model may be estimated and that could be valuable for application to full waveform modeling, for extrapolation to poorly sampled paths, and for overall self-consistency of event locations and amplitudes.

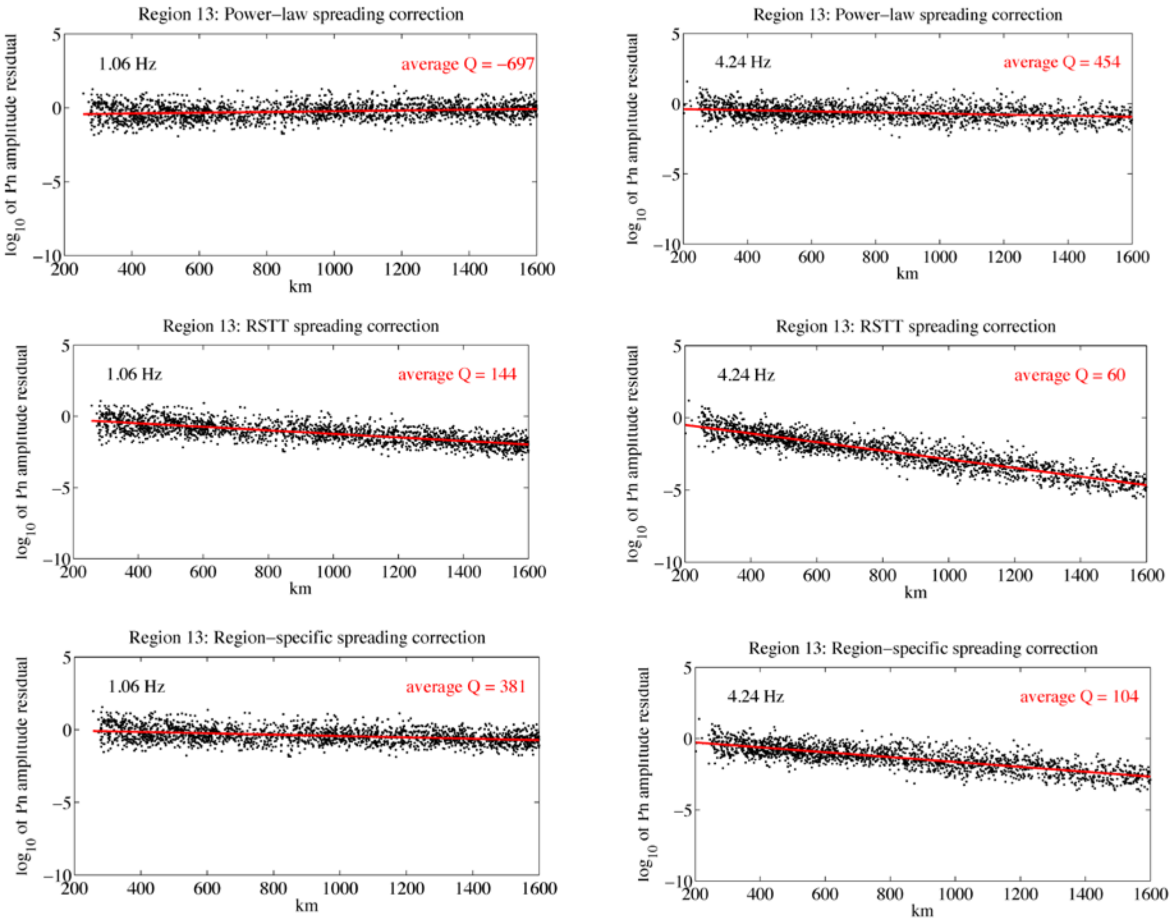

Figure 63a. Pn amplitudes versus distance for Region 13 with corrections using a power-law (top row), RSTT-based synthetic computations (middle row) or empirical region-specific corrections following the procedure of Yang (2011) (bottom row) for passband center frequencies of 1.06 Hz (left) and 4.24 Hz (right). The measured average Q for each case obtained from the regression curve is indicated in the upper right.

Approved for public release; distribution is unlimited.

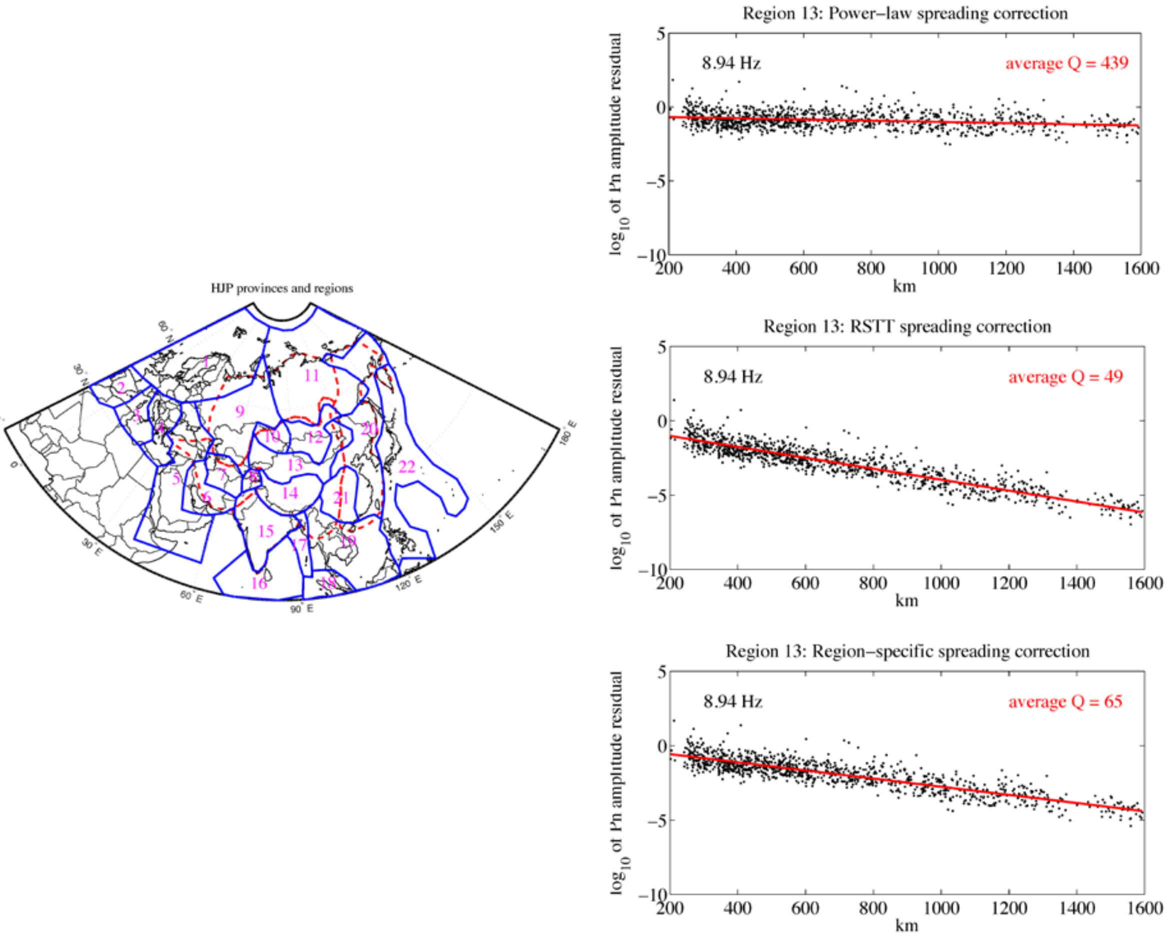

Figure 63b. Pn amplitudes versus distance for Region 13 (map inset) with corrections using a power-law (top row), RSTT-based synthetic computations (middle row) or empirical region-specific corrections following the procedure of Yang (2011) (bottom row) for passband center frequency of 8.94 Hz (right). The measured average Q for each case obtained from the regression curve is indicated in the upper right.

These comparisons support the premise that using regionally varying velocity models can enable self-consistent travel time and geometric spreading for the same regional phases. The scatter is large though, and one cannot demonstrate that a specific regional model and its associated prediction of geometric spreading performs most reliably in terms of reducing variance. This is not unexpected given the results of the earlier sections demonstrating that in the presence of laterally varying lid structure the actual path direction in the medium has a significant effect on both the absolute spreading correction and the frequency-dependent trends in the spreading with distance. It is pretty clear that if the structure is well-determined by travel time branch curvature and/or modeling of waveforms, use of that structure for regional phase spreading is the most sensible approach (compared to a frequency-independent power law correction with an attendant, biased frequency-dependent attenuation model). But, the reality is that neither RSTT nor other regional studies provide strong constraints on actual lid velocity models at this time.

Approved for public release; distribution is unlimited.

4.8 *A 2D Pn Velocity Gradient Model for Eurasia*

P-wave velocities in the uppermost mantle change with depth. The rate of this velocity change, or the radial *P*-wave velocity gradient, plays an important role in shaping the P_n propagation behavior both in terms of its travel time and its amplitude as demonstrated in the previous sections. The velocity gradient also varies laterally due to different uppermost-mantle conditions. It may reflect lateral variations of temperature, composition, and dynamics of the uppermost mantle.

Zhao (1993) mathematically formulated P_n travel time as the summation of crustal-leg travel time, head-wave travel time and the contribution from P_n velocity gradient. Using this formulation, Zhao (1993) and Zhao and Xie (1993) estimated the average P_n velocity gradient for the Basin and Range province in the United States and for the Tibetan Plateau in China. Phillips *et al.* (2007) and Myers *et al.* (2010) extended Zhao's (1993) formulation to account for the lateral variation of P_n velocity gradient and created two-dimensional (2D) P_n velocity-gradient models for Eurasia and North Africa that are merged with locally determined regional velocity structures in the RSTT formulation.

In this section, we adopted the formulation of Zhao (1993) to estimate path-specific P_n velocity gradients from observed P_n travel times. We assumed that each path-specific velocity gradient is the mean of laterally varying velocity gradients along the path. Using this assumption, we inverted the path-specific P_n velocity gradients for a 2D P_n velocity-gradient model for Eurasia. This model framework is helpful for extracting models to be used in Pn geometric spreading calculations for specific paths, as an alternative to the subregion averaging of RSTT models used in the previous section. Our development of a 2D Pn velocity gradient model for Eurasia utilizes different path averaging that was used in RSTT, and we show that our approach may provide a better averaging of the data behavior, although the models are still data-limited with respect to robust determination of radial velocity structure.

We selected data from an updated P_n travel-time dataset of Myers *et al.* (2010) (Begnaud, person. comm.). It contains P_n travel times from more than 5,000 earthquakes and explosions recorded by about 4,500 stations throughout Eurasia. Epicentral distances of the dataset are between 2° and 15°. We required that events for which we include Pn data should have estimated depths (not fixed depths) and they should not be in the mantle (depth < 40 km). The total number of selected measurements is about 85,000.

Figure 64 plots the path density of the dataset that we used to invert for the velocity-gradient model. In general, P_n path density is high in tectonically active regions due to large numbers of earthquakes and stations in those regions. This is particularly true for southern Europe, where the P_n path density is the highest. The large number of paths provides relatively uniform, albeit sparse sampling of all of Eurasia as indicated in Figure 64.

Approved for public release; distribution is unlimited.

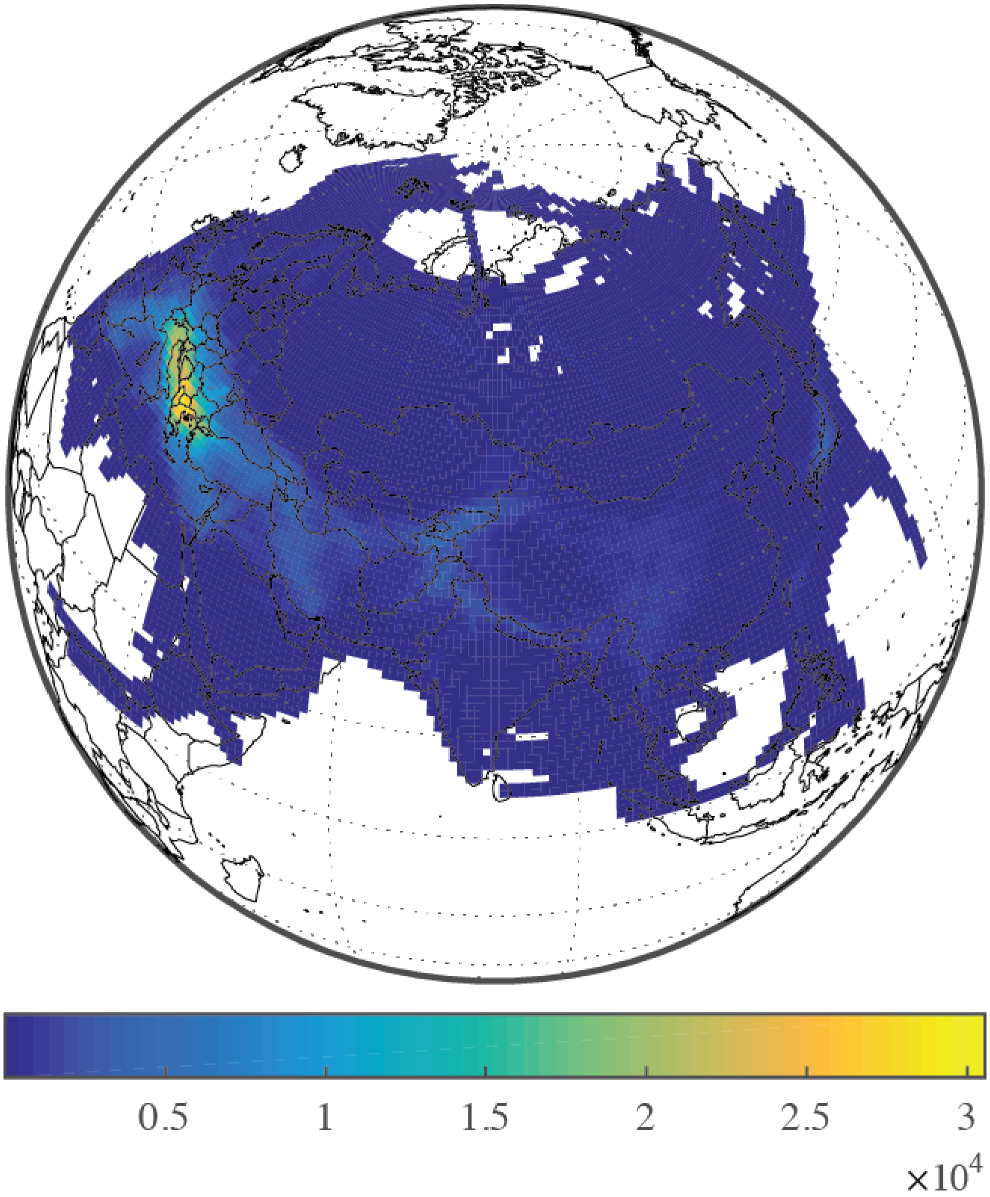

Figure 64. Path density of Pn travel-time measurements used in the tomography.

Zhao (1993) formulated P_n travel time from event *i* to station *j* as

$$t_{ij} = t_i + t_j + t_h + \gamma , \tag{4}$$

where t_{ij} is the total P_n travel time, t_i is the vertical P_n travel time in the crust below the source and t_j is the vertical P_n travel time in the crust below the station. Zhao (1993) decomposed the rest of the P_n travel time into t_h and γ, where t_h was termed “horizontal travel time” by Zhao (1993) and is composed of horizontal P_n travel times in the crust below the source and the station, and the P_n travel time along the Moho between Moho piercing points of the P_n path. γ is the contribution of P_n velocity gradient to the travel

Approved for public release; distribution is unlimited.

time. Myers *et al.* (2010) modified Eq. (4) and redistributed P_n horizontal travel times in the crust from t_h to t_i and t_j such that t_h contained only P_n horizontal travel time along the Moho between P_n piercing points. Under the assumption that P_n velocity gradient was constant for a particular region and the gradient g was much smaller than the average P-wave velocity v_0 beneath the Moho, Zhao (1993) derived the following expression for γ:

$$\gamma \approx -\frac{c^2 X^3}{24 v_0} , \tag{5}$$

where $c = g/v_0$ and X is the horizontal distance between P_n Moho piercing points. For a spherical Earth, $c = (g/v_0 + 1/r)$ where r is the distance from the center of the Earth to Moho. $1/r$ is an Earth flattening correction.

To obtain a 2D P_n velocity-gradient map as well as a 2D P_n velocity map using Eq. (4), Phillips *et al.* (2007) and Myers *et al.* (2010) assumed that c^2 in Eq. (5) could be represented as

$$c^2 = \frac{1}{X}\sum_{n=1}^{N} c_n^2 x_n , \tag{6}$$

where c_n^2 are discretized, laterally-varying c^2 values for the region and x_n is the length of the nth path segment . As a result, Eq. (4) was linearized and a linear-inversion method could be used for the tomography.

In this study, we made a different assumption. Instead of representing the path-specific c^2 as the mean of laterally-varying c^2, we assumed that the path-specific velocity gradient g itself was the mean of the laterally-varying velocity gradient along the P_n path. That is,

$$g = \frac{1}{X}\sum_{n=1}^{N} g_n x_n . \tag{7}$$

To make use of Eqs. (4) and (7) in a linear inversion to obtain a 2D P_n velocity-gradient model, we need to subtract the first three terms on the right-hand side of Eq. (4) from the left-hand side. The velocity gradient g for a particular path can then be calculated with Eq. (5) and used in Eq. (7) for the inversion. We achieved this by tracing the P_n path through the Regional Seismic Travel Time (RSTT) model (Myers *et al.*, 2010) and calculating the travel times t_i, t_j and t_h. Because RSTT was obtained from an inversion that incorporated both P_n slowness and P_n velocity gradient as model parameters, and these two parameters depend on the path in similar ways (Myers *et al.*, 2010, Eq. 7), there might be certain degree of tradeoffs between the resulting velocity map and the velocity-gradient map. To avoid the potential error of the RSTT P_n velocity map due to the tradeoff, we replaced the Moho P_n velocity in RSTT with that from the independent Sandia-Los Alamos 3D P-wave velocity model (SALSA3D) (Ballard *et al.*, 2010; Begnaud *et al.*, 2011) and constructed a hybrid model for the ray tracing.

Approved for public release; distribution is unlimited.

Figure 65 shows the calculated γ by subtracting t_i, t_j and t_h, obtained from the ray tracing, from measured P_n travel times (Eq. 4). According to Eq. (5), γ should always be negative and decreases with increasing distance. A smaller γ corresponds to a higher velocity gradient in the uppermost mantle.

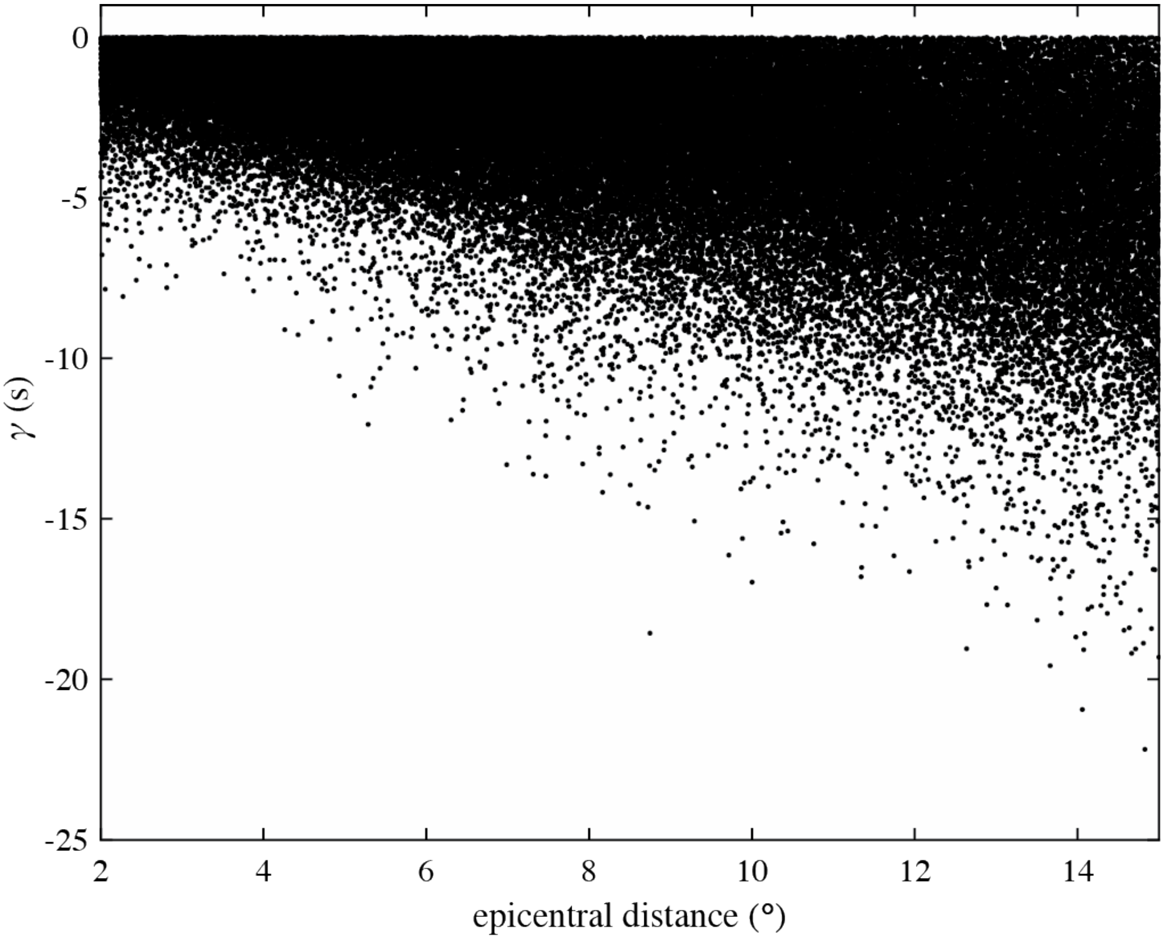

Figure 65. Path-specific γ from measured P_n travel times.

To see which assumption, either the Phillips *et al.* (2007) and Myers *et al.* (2010) assumption of path-specific c^2 as the mean of location-dependent c^2 or our assumption of path-specific gradient as the mean of location-dependent gradient, is more reasonable, we conducted two-dimensional Monte Carlo simulations to simulate P_n waves traveling in a mantle with laterally heterogeneous velocity gradient.

The 2D model that we used for the simulation was composed of 10 equal-width regions with the same velocity of 8.1 km/s at the top and different vertical velocity gradients. The model is 500 km in depth, which guarantees that all P_n rays bottom within the model. In the simulation, travel times between a source and a receiver 1200-km apart at the two top corners of the model were calculated repeatedly. For each calculation, the order of the regions was changed in a random fashion from the previous calculation. Figure 66 shows two realizations of the model as examples.

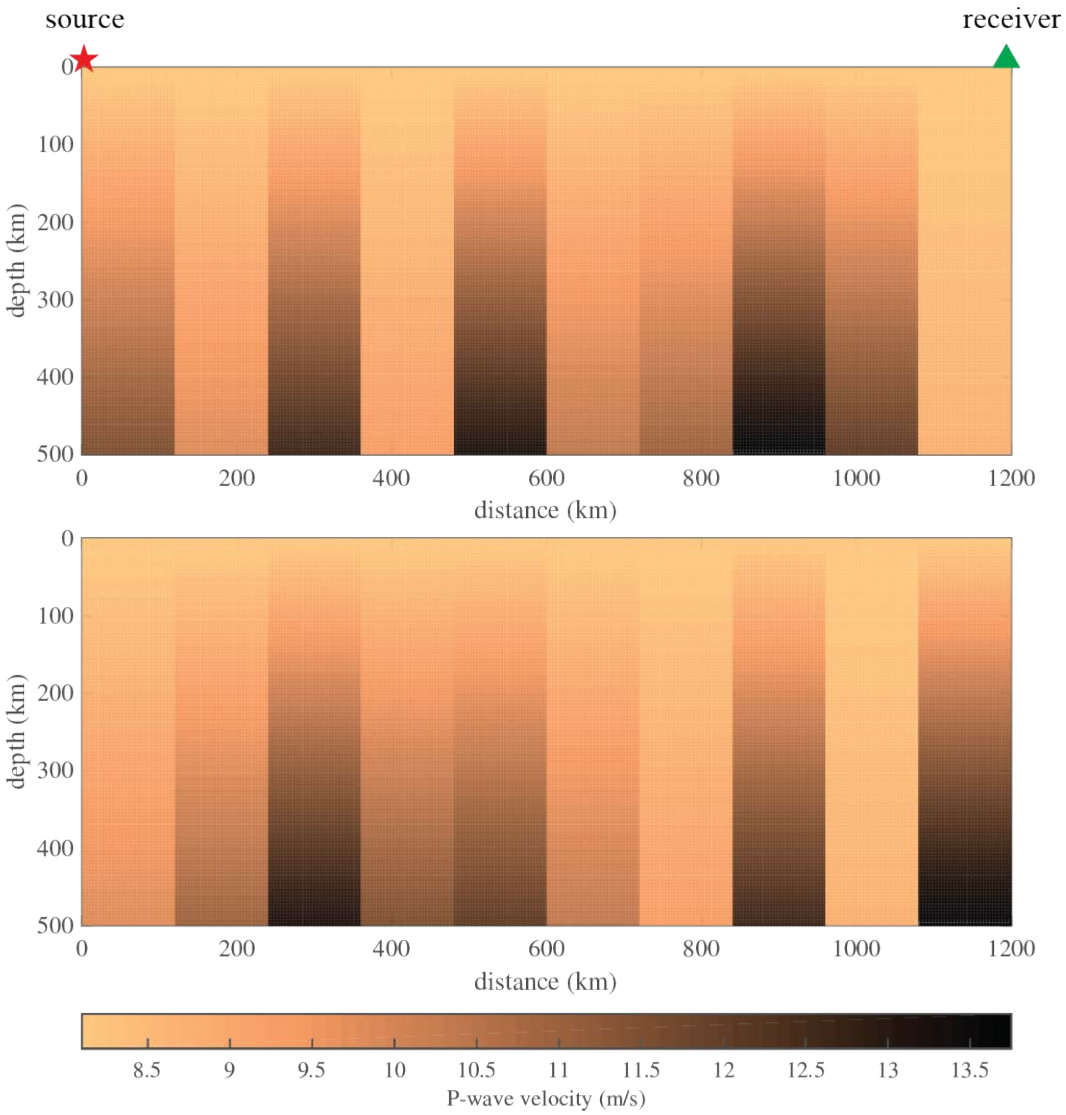

Figure 66. Two realizations of the velocity-gradient model for the Monte Carlo simulation.

We used the Multistencils Fast Marching (MSFM) method (Hassouna and Farag, 2007) to calculate P_n travel times through the model. Figure 67 plots the P_n travel times calculated from 10,000 iterations as a histogram. The red line in the figure marks the travel time calculated from a model with a single velocity gradient that is the mean of the gradients of the model used in the simulation. The dashed green line is the travel time from a model constructed using the assumption of Phillips *et al*. (2007) and Myers *et al*. (2010). The travel time calculated using our assumption is very close to the mean of the travel times from the Monte Carlo simulation (0.07% difference). The travel time calculated from Phillips *et al*. (2007) and Myers *et al*.' (2010) assumption, on the other hand, is much more biased (0.7% difference). The simulation indicates that the cumulative velocity-gradient effect on the P_n travel time is better modeled by averaging the laterally-varying velocity gradient along the P_n path than by averaging the square of the gradient.

Approved for public release; distribution is unlimited.

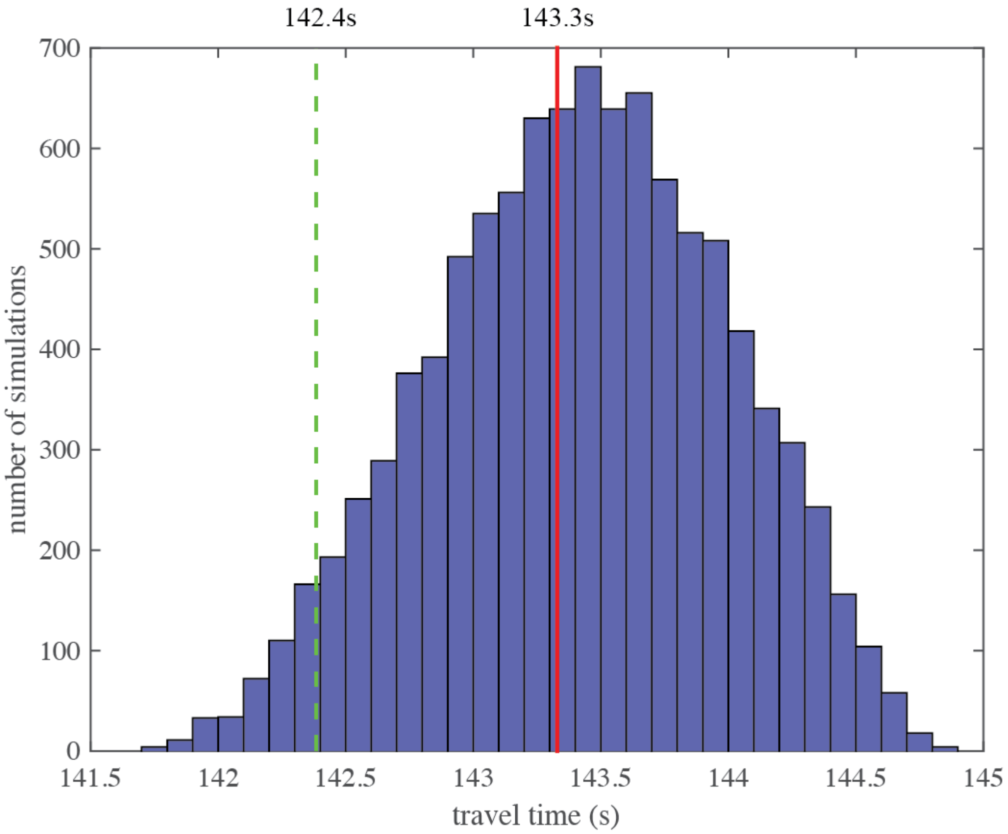

Figure 67. Distribution of P_n travel times from the Monte Carlo simulation. The mean of the distribution is 143.4s. The red line marks the travel time for a model with a single velocity gradient calculated as the mean of the laterally varying gradients. The green line marks the travel time for a model where the gradient is calculated as the square root of the mean of the square of the laterally varying gradients.

We took a Bayesian approach in a damped and weighted least-squares inversion to invert for the 2D P_n velocity-gradient model. We discretized Eurasia using the software GeoTess (Ballard *et al*., 2009; Ballard *et al.*, 2012), which employs a triangular tessellation method. For such a node-based model, Eq. (7) becomes

$$g = \frac{1}{X}\sum_{n=1}^{N}\sum_{p=1}^{3} g_p c_{pn} x_n \ , \tag{8}$$

where g_p are velocity gradients at model nodes surrounding the nth path segment and c_{pn} are weighting coefficients based on the distances from the center of the path segment to the surrounding model nodes. With calculated path-specific P_n velocity gradients and Eq. (8), we built a system of linear equations for the tomographic inversion to construct the 2D velocity-gradient model.

Figure 68 illustrates the model tessellation. To construct the tessellation, we first defined the region where we had data coverage. We then constructed the mesh using

Approved for public release; distribution is unlimited.

variable-resolution discretization. Within the region with data coverage, the node spacing is 1°. Away from the region, the spacing progressively increases. During the inversion, only nodes that contributed to the calculation of path-specific velocity gradients were included.

Figure 68. Tessellation of the model.

We used the right-hand side of Eq. (5) to derive an *a priori* model for the inversion. We first summed c_{pn} for each node over all paths. We then replaced g_p on the right-hand side of the equation with g on the left-hand side for each measurement and summed gc_{pn} for each node over all paths. The *a priori* model was obtained by dividing the second summation by the first summation. The *a priori* model is shown in the Figure 69. The gradients range from -0.001 s^{-1} to 0.074 s^{-1}.

Approved for public release; distribution is unlimited.

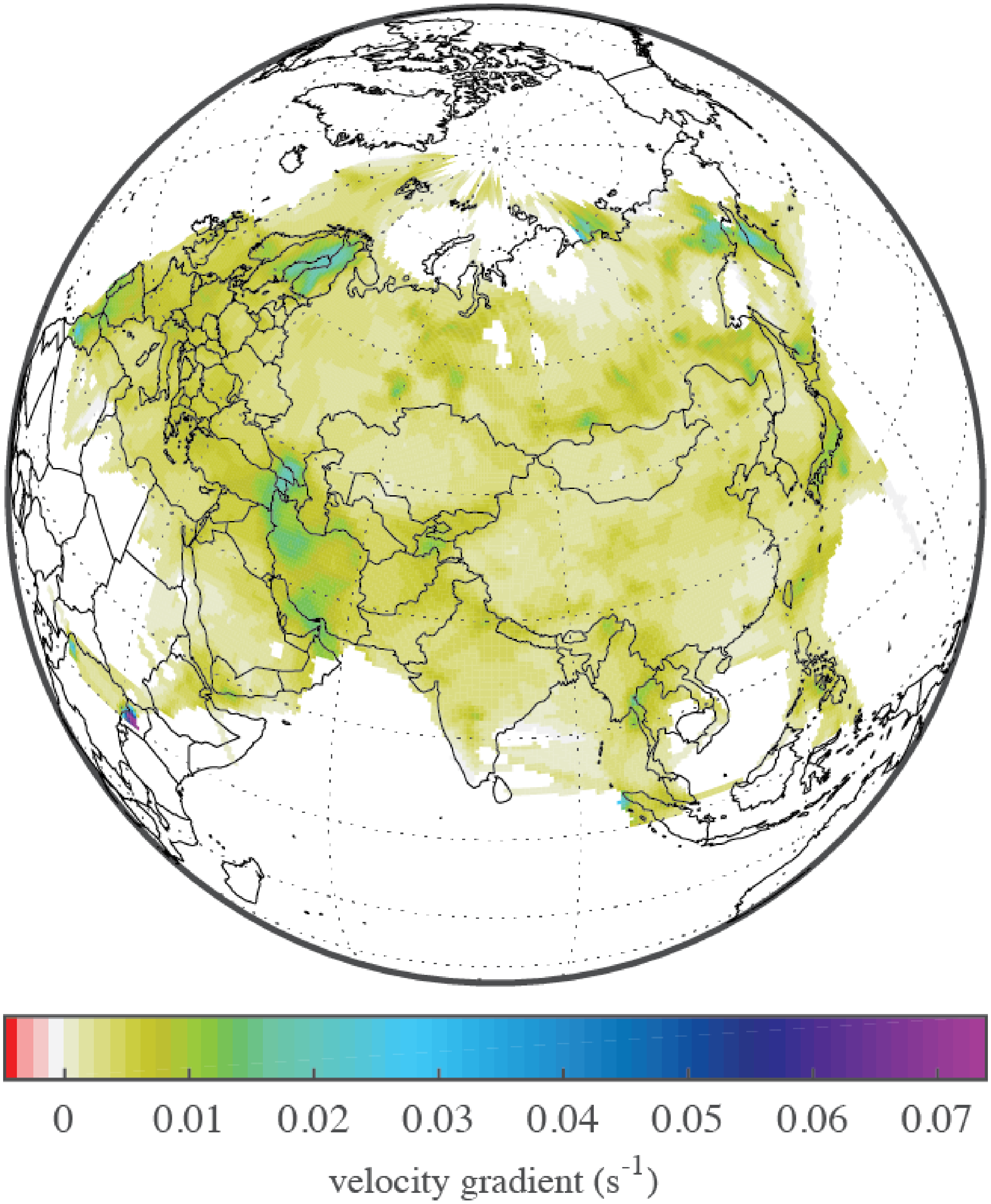

Figure 69. The *a priori* model used in the inversion.

Figure 70 shows the P_n velocity-gradient model for Eurasia from the tomographic inversion along with constant model-resolution contours. A model node is perfectly resolved if its resolution is one. The best-resolved node in the model has a resolution of 0.73. The model is reasonably resolved along the Alpine-Himalayan orogenic belt, in Scandinavia, and along the western Pacific in Japan and Taiwan. Northern Eurasia, Arabian Peninsula, southeast China and much of India are not very well resolved due to poor path coverage.

Approved for public release; distribution is unlimited.

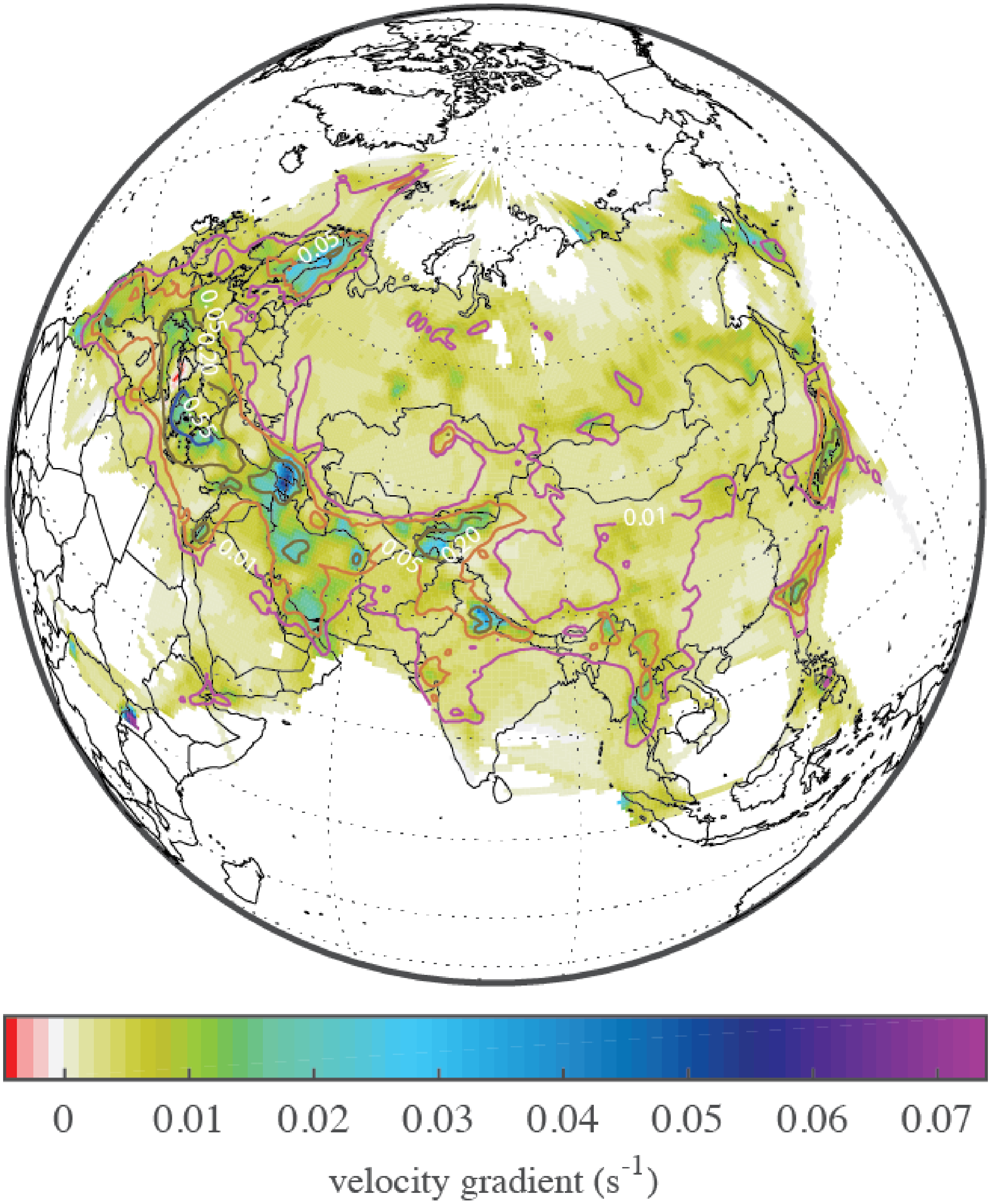

Figure 70. P_n velocity-gradient model from the tomographic inversion. Purple lines are constant model-resolution contours. Corresponding values of some of the contours are marked.

To better visualize the resolution power of the data used in the inversion, Figure 71 shows the result of a checkerboard test. A checkerboard model with 5° cells and alternating gradient values between -0.0006 s^{-1} and 0.0042 s^{-1} was used to generate the synthetic data. Similar to what the model-resolution values indicate, the checkerboard-test result shows that the model is well resolved for an elongated region bounded on the south

Approved for public release; distribution is unlimited.

by the Alpine-Himalayan orogenic belt, for the North-South seismic belt in China and for Japan. The best-resolved region both in terms of the pattern and in terms of the gradient values is along the western portion of the Tethys collision belt in southern Europe, where the path density is also the highest (Figure 64). Again, regions under northern Eurasia, southeast China, eastern portion of India and the Arabian Peninsula are not well resolved.

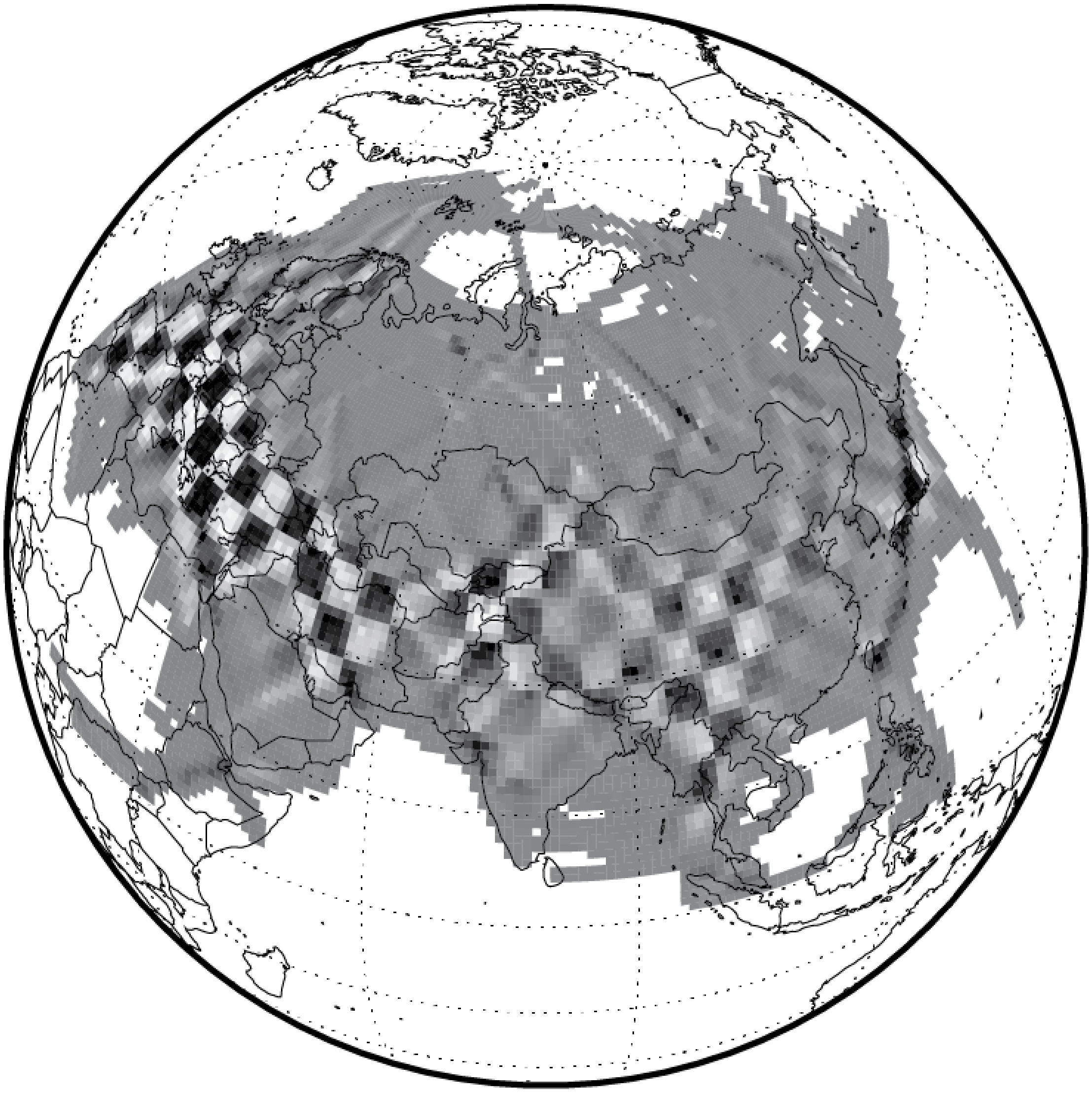

Figure 71. Checkerboard-test result indicating the resolution power of the data used in the inversion.

Figure 72 compares data residuals using model predictions from the *a priori* model and those from the final model. The distribution of residuals from the final model is closer to a normal distribution and less skewed than the distribution of residuals from the *a priori* model.

Approved for public release; distribution is unlimited.

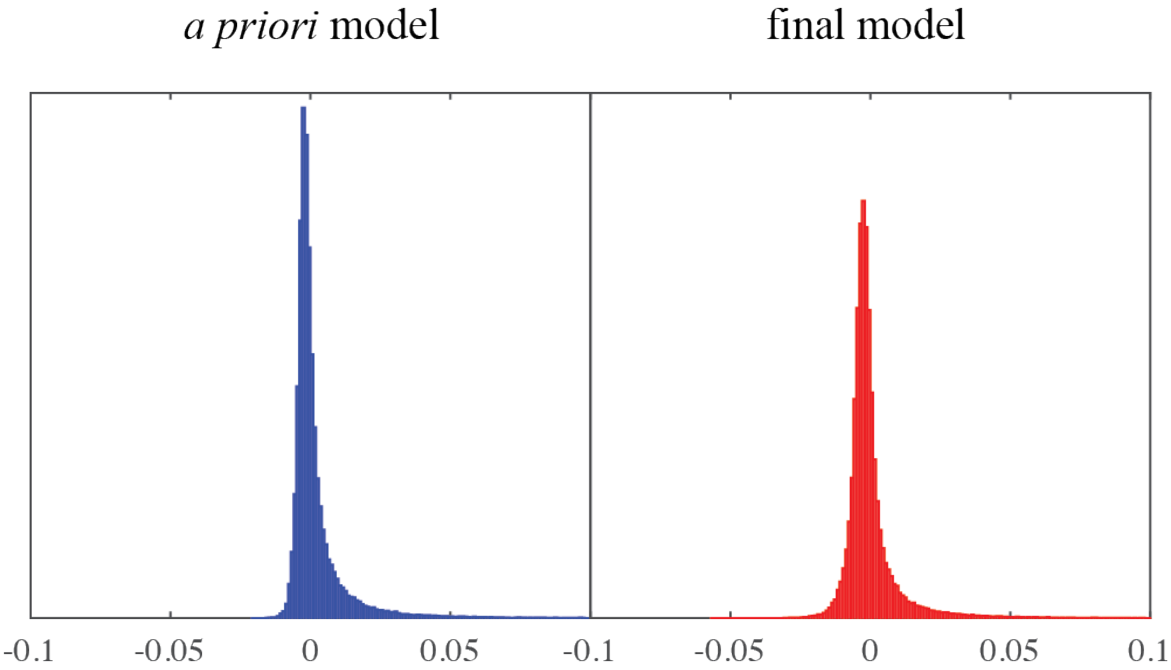

Figure 72. Histograms of prediction residuals from both the *a priori* model and from the final model.

Figure 73 again shows the tomographic P_n velocity-gradient model. Also plotted are tectonic plate boundaries (Bird, 2003). The velocity gradient is almost universally positive for the whole of Eurasia. Much of the gradient variations occur along collisional plate boundaries under overriding plates. This indicates that strong velocity-gradient variations and the presence of complex tectonic processes involved in plate collisions may be related. The highest gradient is observed in the Caucasus region between the Black Sea and the Caspian Sea. Other regions of higher gradient include the Scandinavia region, western and southern Iran, the Hindu Kush and western part of the Himalayas. Except the Scandinavia region, all other regions of high velocity gradient are tectonically active regions.

Approved for public release; distribution is unlimited.

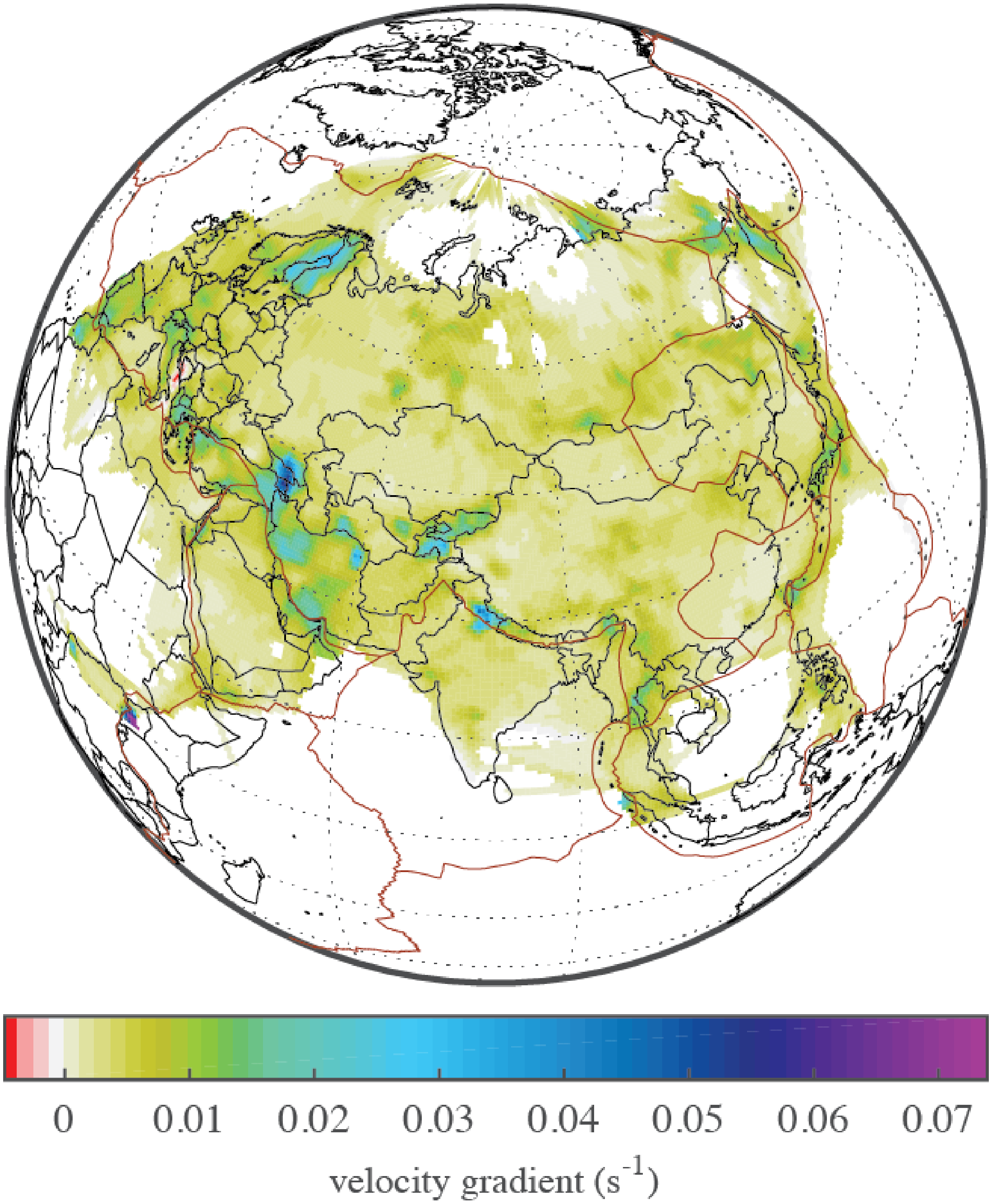

Figure 73. The tomographic P_n velocity-gradient model and tectonic-plate boundaries.

Figure 74 plots the RSTT P_n velocity-gradient model for a comparison. As is indicated by the Monte Carlo simulation discussed above, velocity gradients in the RSTT model are generally lower. The mean gradient of RSTT is 0.0012 s^{-1} whereas the mean of the model from this study is 0.0044 s^{-1}. The maximum gradient of RSTT is 0.0189 s^{-1} whereas that of our model is 0.0739 s^{-1}. There are also much less variations in RSTT than in our model. The difference between the maximum and minimum velocity gradients in RSTT is 0.0198 s^{-1}. The difference is 0.0779 s^{-1} in our model. The highest gradients in RSTT concentrate

Approved for public release; distribution is unlimited.

in subduction zones in the western Pacific. There are also significantly more negative-gradient areas in RSTT.

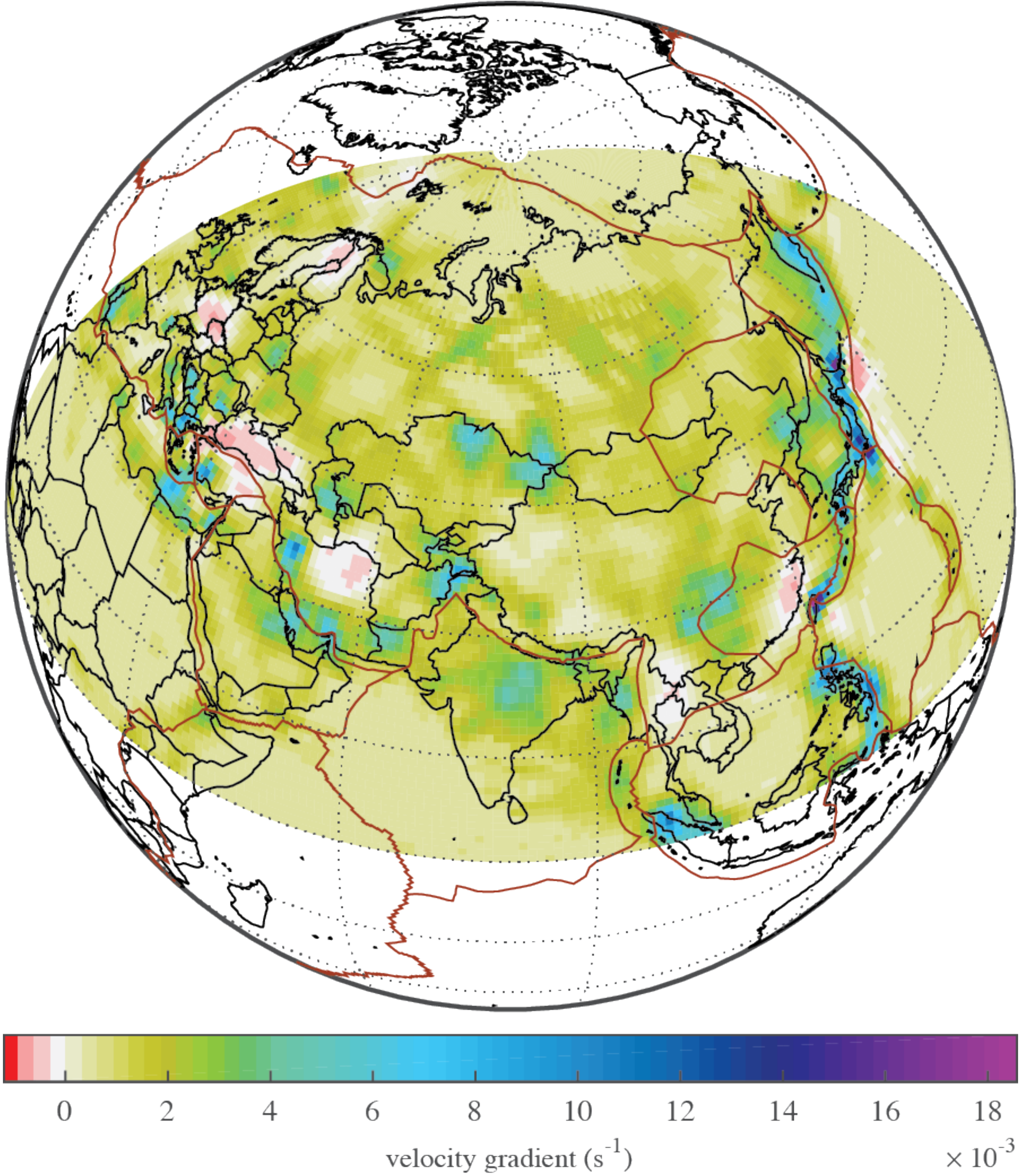

Figure 74. RSTT P_n velocity-gradient model.

Approved for public release; distribution is unlimited.

5.0 SUMMARY OF FINDINGS

New 2D computations of Pn geometric spreading have established that the amplitude variation is dependent on direction of the path and that complex frequency dependence is expected to have mixing of the near-source and near-receiver structures. This further weakens the rationale for using average power-law representations of the Pn (and Sn) geometric spreading. As the only structure that will result in a power law behavior for sure are those with negative critical gradients in the mantle lid (a possible, but probably very rare situation), we further support the contention of Yang (2011) that a simple velocity model based correction, or an empirically grounded correction is a more sensible choice than a frequency-independent power law.

We explored 2D models with fine-scale heterogeneity to evaluate whether the tendency to smooth out the distance behavior for 1 Hz signals as found by Avants et al. (2011) holds for broadband Pn signals. All calculations, for suites of heterogeneity realizations, support some modification of the amplitude-distance trends for Pn, but the frequency-dependence of models with radial velocity gradients is enhanced by the presence of small-scale lithospheric heterogeneity. This is the result of scattering of Pn energy out of the lid waveguide into the crust. While the general trends of the amplitude spreading terms do approach the power law decay form commonly assumed, there is associated strong frequency dependence, which is not commonly assumed.

Effects of crustal thinning and Moho dip on Pn from North Korean nuclear tests to stations in Japan account for relatively enhanced Pn amplitudes near 1000 km observed for relatively low frequencies in Japan compared to continental structure paths to stations in China near the same distance. The lateral transitions from continent to ocean and ocean to island arc favor transfer of P energy into the Pn wavefield near the sources and into the crust near the receivers. Above 7 Hz, the observations in Japan show rapid amplitude decrease, which we attribute to intrinsic attenuation effects.

Application of regionalized Pn spreading corrections based on RSTT models (derived exclusively from regional travel time observations and velocity models) or regionalized fitting of attenuation models to data provide fairly similar Q(f) estimates, much lower than those from a constant power law spreading coefficient. While the choice of optimal spreading is not unambiguous in every case based on some measure of variance reduction in the model performance, the more reasonable attenuation parameters obtained using the RSTT or empirical spreading corrections suggest they are more appropriate than standard power law assumptions. This means that it is possible in general to develop self-consistent travel time and amplitude models for Pn. The major challenge is to attain sufficient data coverage to actually resolve the radial gradients in upper mantle structure that have strong effect on the Pn spreading. When this is achieved, the regional model should be used for both event location and regional amplitude analysis (and attenuation model determination), as the modeling conducted here demonstrates the reduction of bias in the attenuation models that is likely to be achieved.

Approved for public release; distribution is unlimited.

We developd a 2D P_n velocity-gradient model for Eurasia based on observed P_n travel times. These travel times were corrected for crustal and head-wave components to isolate the velocity-gradient contribution for path-specific velocity-gradient calculation. The assumption that these path-specific velocity gradients were the mean of the laterally varying velocity gradients along the paths was validated through a Monte Carlo simulation. A tomographic P_n velocity-gradient model was then derived using a linear Bayesian inversion approach.

The velocity-gradient model is well resolved in tectonically active regions. The gradient is positive almost everywhere. Large gradient variations are observed mainly along collisional plate boundaries under overriding plates. It may imply a relationship between the presence of active tectonic processes involved in plate collisions and the P_n velocity-gradient variation in the uppermost-mantle. This model can be used to predict path-specific Pn spreading along with use for travel time calculation and event location.

Approved for public release; distribution is unlimited.

REFERENCES

Aki, Keiiti and Paul G. Richards, 2002, Quantitative Seismology: Theory and Methods, University Science Books, ISBN 0-935702-96-2, ISBN 978-0-935702-96-5.

Avants, M., T. Lay, X.-B. Xie, and X. Yang, 2011, Effects of 2D random velocity heterogeneities in the mantle lid and Moho topography on *Pn* geometric spreading, *Bull. Seism. Soc. Am.* 101, pp. 126-140.

Ballard, S., J. R. Hipp, and C. J. Young, 2009, Efficient and accurate calculation of ray theory seismic travel time through variable resolution 3D Earth models, *Seismol. Res. Lett.*, 80, pp. 990-1000, doi: 10.1785/gssrl.80.6.990.

Ballard, S., M. A. Begnaud, C. J. Young, J. R. Hipp, M. Chang, A. V. Encamacao, C. A. Rowe, W. S. Phillips, and L. K. Steck, 2010, A global 3D P-velocity model of the Earth's crust and mantle for improved event location – SALSA3D, in *Proceedings of the 2010 Monitoring Research Review: Ground-Based Nuclear Explosion Monitoring Technologies*, Orlando, Florida, September 21-23, 2010, pp. 31-39.

Ballard, S., J. R. Hipp, A. V. Encamacao, C. J. Young, and B J. Kraus, 2012, A generalized Earth model software utility, in *Proceedings of the 2012 Monitoring Research Review: Ground-Based Nuclear Explosion Monitoring Technologies*, Albuquerque, New Mexico, September 18-20, 2010, pp. 745-753.

Begnaud, M. A., S. Ballard, C. J. Young, J. R. Hipp, M. Chang, A. V. Encamacao, C. A. Rowe, W. S. Phillips, and L. K. Steck, 2011, A global 3D P-velocity model of the Earth's crust and mantle for improved event location, in *Proceedings of the 2011 Monitoring Research Review: Ground-Based Nuclear Explosion Monitoring Technologies*, Tucson, Arizona, September 13-15, 2011, pp. 237-248.

Bird, P., 2003. An updated digital model of plate boundaries, *Geochem. Geophys. Geosyst.* **4**, 1027, doi: 10.1029/2001GC000252.

Červený, V. and R. Ravindra, 1971, *Theory of Seismic Head Waves*, University of Toronto Press, Toronto.

Fisk, M. D., H. L. Gray, and G. D. McCartor, 1996, Regional discrimination without transporting thresholds, *Bull. Seism. Soc. Am.*, 86, pp. 1545-1558.

Fisk, M.D., S.R. Taylor, and T. Lay, 2005, Modeling and empirical research on energy partitioning of regional seismic phases used for explosion monitoring, *Proceedings of the 27th Seismic Research Review*, pp. 539-549.

Hartse, H.E., S.R., Taylor, W.S., Phillips, and G.E. Randall, 1997, A preliminary study of regional seismic discrimination in central Asia with emphasis on western China, *Bull. Seism. Soc. Am.*, 87, pp. 551-568.

Hassouna, M. S. and A. A. Farag, 2007, Multistencils fast marching methods: a highly accurate solution to the Eikonal equation on Cartesian domains, *IEEE Transactions on Pattern Analysis and Machine Intelligence*, 29, pp. 1563-1574, doi: 10.1109/TPAMI.2007.1154.

Hill, D. P., 1973. Critically refracted waves in a spherically symmetric radially heterogeneous Earth model, *Geophys. J. R. Astr. Soc.*, 34, pp. 149-177.

Kim, W. Y., V. Aharonian, A. L. Lerner-Lam and P. G. Richards, 1997, Discrimination of earthquakes and explosions in southern Russia using regional high-frequency three-component data from IRIS/JSP Caucasus Network, *Bull. Seism. Soc. Am.*, 87, pp. 569-588.

Laske, G., G. Masters., Z. Ma, and M. Pasyanos, 2013, Update on CRUST1.0 - A 1-degree Global Model of Earth's Crust, Geophys. Res. Abstracts, 15, Abstract EGU2013-2658.

Myers, S. C., M. L. Begnaud, S. Ballard, M. E. Pasyanos, W. S. Phillips, A. L. Ramirez, M. S. Antolik, K. D. Hutchenson, J. J. Dwyer, C. A. Rowe, and G. S. Wagner, 2010, A Crust and Upper-Mantle Model of Eurasia and North Africa for *Pn* Travel-Time Calculation, *Bull. Seismol. Soc. Am.*, 100, pp. 640-656, doi: 10.1785/0120090198.

Patton, H.J., 2001, Regional magnitude scaling, transportability, and Ms:mb discrimination at small magnitudes, *Pageoph*, 158, pp. 1951-2015.

Phillips, W. S., M. L. Begnaud, C. A. Rowe, L. K. Steck, S. C. Myers, M. E. Pasyanos and S. Ballard, 2007, Accounting for lateral variations of the upper mantle gradient in *Pn* tomography studies, *Geophys. Res. Lett.*, 34, L14312, doi:10.1029/2007GL029338.

Richards, P. G. and W.-Y. Kim, 2007, Seismic signature, *Nature Physics*, 3, pp. 4-6.

Sereno, T.J., S.R. Bratt, and T.C. Bache, 1988. Simultaneous inversion of regional wave spectra for attenuation and seismic moment in Scandinavia, *J. Geophys. Res.*, 93, pp. 2019-2036.

Sereno, T. J. and J. W. Given, 1990, *Pn* attenuation for a spherically symmetric Earth model, *Geophys. Res. Lett.*, 17, pp. 1141-1144.

Street, R. L., R. Herrmann, and O. Nuttli, 1975, Spectral Characteristics of the Lg Wave Generated by Central United States Earthquakes, *Geophys. J. R. Astr. Soc.*, 41, pp. 51-63.

Taylor, S.R., 1996, Analysis of high frequency *Pn*/Lg ratios from NTS explosions and western U.S. earthquakes, *Bull. Seism. Soc. Am.*, 86, pp. 1042-1053.

Taylor, S. R., M. D. Denny, E. S. Vergino, and R. E. Glaser, 1989, Regional discrimination between NTS explosions and western U.S. earthquakes, *Bull. Seism. Soc. Am.*, 79, pp. 1142-1176.

Taylor, S. R. and H. E. Hartse, 1997, An evaluation of generalized likelihood ratio outlier detection to identification of seismic events in western China, *Bull. Seism. Soc. Am.*, 87, pp. 824-831.

Walter, W.R., K.M., Mayeda, and H. Patton, 1995, Phase and spectral ratio discrimination between NTS earthquakes and explosions. Part I: Empirical observations, *Bull. Seism. Soc. Am.*, 85, pp. 1050-1067.

Xie, J., 2002, Source scaling of *Pn* and Lg spectra and their ratios from explosions in central Asia: Implications for the identification of small seismic events at regional distances, *J. Geophys. Res.* 107, B7, 10.1029/2001JB000509.

Xie, X.B. and T. Lay, 1994, The excitation of Lg waves by explosions: A finite-difference investigation, *Bull. Seism. Soc. Am.*, 84, pp. 324-342.

Yang, X., 2011, A *Pn* spreading model constrained with observed amplitudes in Asia, *Bull. Seism. Soc. Am.,* 101, pp. 2201-2211, doi: 10.1785/0120100314.

Yang, X., T. Lay, X. Xie, and M. S. Thorne, 2007. Geometric spreading of *Pn* and *Sn* in a spherical Earth model, *Bull. Seism. Soc. Am.,* 97, pp. 2053-2065.

Approved for public release; distribution is unlimited.

Zhao, L., 1993, Lateral variations and azimuthal isotropy of Pn velocities beneath Basin and Range province, *J. Geophy. Res.*, 98, pp. 22109-22122.

Zhao, L. and J. Xie, 1993, Lateral variations in compressional velocities beneath the Tibetan Plateau from P_n travel-time tomography, *Geophys. J. Int.*, 115, pp. 1070-1084.

Zhao, L.-F., X.-B. Xie, W.-M. Wang, and Z.-X. Yao, 2008, Regional seismic characteristics of the October 9, 2006 North Korean nuclear test, *Bull. Seism. Soc. Am.*, 98, pp. 2571-2589, doi: 10.1785/0120080128.

Zhao, L.-F., X.-B. Xie, B.-F. Tian, Q.-F. Chen, T.-Y. Hao, and Z.-X. Yao, 2015, Pn-wave geometrical spreading and attenuation in Northeast China and the Korean Peninsula constrained by observations from North Korean nuclear explosions, *J. Geophys. Res. Solid Earth*, 120, doi:10.1002/2015JB012205.

APPENDIX - Preprint of Manuscript Accepted for Publication in Journal of Geophysical Research.

Pn wave Geometrical Spreading and Attenuation in Northeast China and the Korean Peninsula Constrained by Observations from North Korean Nuclear Explosions

Lian-Feng Zhao,[1] Xiao-Bi Xie,[2] Bao-Feng Tian,[3] Qi-Fu Chen,[1] Tian-Yao Hao,[1] and Zhen-Xing Yao[1]

Running title:

Pn-wave geometric spreading and attenuation

[1] Key Laboratory of Earth and Planetary Physics, Institute of Geology and Geophysics, Chinese Academy of Sciences, Beijing, China (zhaolf@mail.iggcas.ac.cn)

[2] Institute of Geophysics and Planetary Physics, University of California at Santa Cruz, California, USA (xxie@ucsc.edu)

[3] Institute of Geophysics, China Earthquake Administration, Beijing, China

Published online 10 October 2015 in *Journal of Geophysical Research Solid Earth*, **120**,

doi:10.1002/2015JB012205

Corresponding Author:

Lian-Feng Zhao

Key Laboratory of Earth and Planetary Physics
Institute of Geology and Geophysics, Chinese Academy of Sciences
19 Beituchengxilu, Chaoyang District
Beijing, China
100029
Tel. 011-86-10-82998658
Fax 011-86-10-62010846
zhaolf@mail.iggcas.ac.cn

Approved for public release; distribution is unlimited.

Highlights

A data-constrained, frequency-dependent, log-quadratic Pn spreading model.
Apparent Pn-wave attenuation in Northeast China and the Korean Peninsula.
Uppermost mantle P-wave attenuation model in the region.

Abstract

We investigate the geometric spreading and attenuation of seismic Pn waves in Northeast China and the Korean Peninsula. A high-quality broadband Pn-wave dataset generated by North Korean nuclear tests is used to constrain the parameters of a frequency-dependent log-quadratic geometric spreading function and a power-law Pn Q model. The geometric spreading function and apparent Pn wave Q are obtained for Northeast China and the Korean Peninsula between 2.0 and 10.0 Hz. Using the two-station amplitude ratios of the Pn spectra and correcting them with the known spreading function, we strip the contributions of the source and crust from the apparent Pn Q and retrieve the P-wave attenuation information along the pure upper mantle path. We then use both Pn amplitudes and amplitude ratios in a tomographic approach to obtain the upper mantle P-wave attenuation in the studied area. The Pn-wave spectra observed in China are compared with those recorded in Japan, and the result reveals that the high-frequency Pn signal across the oceanic path attenuated faster compared with those through the continental path.

Key words

Pn; Geometric spreading; Attenuation; Uppermost mantle P-wave Q; North Korea nuclear tests

Approved for public release; distribution is unlimited.

1 Introduction

The seismic Pn wave typically appears as the first arrival in regional seismograms at distances between 200 and 2000 km. Unlike other regional phases, such as Pg and Lg waves, the Pn wave is typically less affected by the crustal structures or contaminated by prior phases and is therefore widely applied for seismic location, magnitude and yield estimation as well as for investigating seismic source process. The Pn-wave attenuation measurement is an important issue as well not only because obtaining accurate source parameters requires correction for the amplitude decay but also attenuation itself can be useful for characterizing the upper mantle properties. Pn and Sn waves cannot be simply explained as headwaves developed along a flat Moho discontinuity. Their actual propagation processes, particularly their amplitude variations in a spherical earth, are much more complicated. *Červený and Ravindra* [1971] and *Hill* [1973] theoretically investigated the behavior of Pn waves in a spherical Earth model and regarded this phase as an interference of multiple-diving waves reflected from the underside of the Moho discontinuity. *Sereno and Given* [1990] studied Pn waves in flat and spherical earth models and found that Earth's sphericity alone causes a significant departure in Pn geometrical spreading and that the phenomenon is frequency dependent. Based on numerical simulations, *Yang et al.* [2007] proposed a log-quadratic model for Pn and Sn geometric spreading functions to accommodate the Earth's sphericity. Compared with the traditional power-law model, their spreading model included 9 parameters to address both distance- and frequency-dependencies.

Many attempts have been targeted at using observed data to constrain Pn-wave attenuation and geometrical spreading [*Chun et al.*, 1989; *Sereno et al.*, 1988; *Xie*, 2007; *Xie and Patton*, 1999; *Zhu et al.*, 1991]. The underlying difficulties are that attenuation and geometrical spreading are tightly coupled and both are dependent on distance and frequency. In addition, the observed Pn amplitudes are highly scattered due to their narrow sampling of radiation patterns, inaccurate source locations, and pronounced sensitivity to the uppermost mantle structures. Different strategies were adopted to mitigate this difficulty. By assuming a frequency-independent spreading function of $\Delta^{-1.3}$, where Δ is the distance, *Sereno et al.* [1988] investigated the Pn-wave Q in Scandinavia and obtained a Q_0 (1 Hz Q) of 325. Using the same spreading function, *Xie and Patton* [1999] obtained a Q_0 of 364 for central Asia, and *Xie* [2007] observed low Pn Q under the north-central Tibetan plateau between 0.3 and 10.0 Hz. *Chun et al.* [1989] determined the high-frequency Pn attenuation in eastern Canada based on a frequency-dependent Pn spreading $\Delta^{-(2.2+0.02\cdot f)}$ between 3.0 and 15.0 Hz. *Zhu et al.* [1991] simultaneously estimated both frequency-dependent geometric spreading and Q for Pn waves in the Canadian shield.

Others attempted to estimate the Pn- or Sn-wave propagation efficiency without apparently addressing the geometric spreading. *Calvert et al.* [2000] measured the propagation efficiency by separating the attenuation into the average portion and the perturbation portion, avoiding defining the absolute attenuation measurement. Using the ratio of the Sn amplitude to the Pg coda amplitude, *Barron and Priestley* [2009] presented the frequency-dependent propagation efficiency of the Sn wave over the Tibetan Plateau. By stacking the densely distributed USArray data, *Buehler and Shearer* [2013] calculated the Sn propagation efficiency and identified highly attenuating regions in the Western

Approved for public release; distribution is unlimited.

United States. Another strategy involves building a geometric spreading model followed by separating the attenuation from the spreading. *Yang et al.* [2007] proposed a log-quadratic geometric spreading function based on numerical simulations in a radially symmetric earth model. *Avants et al.* [2011] further discussed the contribution of scattering to this spreading model. Applying this log-quadratic spreading model to Eurasia data, *Yang* [2011] obtained a more reasonable Pn Q between distances of 200 and 1000 km and frequencies of 0.5 and 10.0 Hz.

Between 2006 and 2013, North Korea conducted three underground nuclear tests. Compared with natural earthquakes, these explosive sources have accurate epicenter locations and source depths, simple and approximately identical source time functions, and most importantly virtually isotropic radiation patterns. Seismic networks recorded abundant regional phases from these events, including the Pn wave, in Northeast China, the Korean Peninsula and Japan, either across the continental or oceanic paths [e.g., *Chun et al.*, 2009; *Hong and Rhie*, 2009; *Murphy et al.*, 2013; *Richards and Kim*, 2007; *Wen and Long*, 2010; *Zhao et al.*, 2008, 2012, 2014].

In this study, we use this high-quality dataset to investigate Pn-wave propagation in Northeast China and the Korean Peninsula, including its geometrical spreading and the apparent Pn attenuation. An inversion method is used to formally separate the spreading and attenuation using the observed spectral amplitudes. Frequency dependent parameters for a log-quadratic spreading model in Northeast China and the Korean Peninsula are derived from the data. Using two-station amplitude ratios and the known spreading function, we strip the effect of the crust leg from the apparent Pn-wave attenuation to obtain the P-wave attenuation along the pure upper mantle path. Combining both single-station amplitudes and two-station amplitude ratios, an uppermost mantle P-wave attenuation tomography approach is proposed. Using Pn observations across Northeast China and those through the Japan Sea, the Pn spectral amplitudes across the continental and oceanic paths are compared.

2 Data

2.1 Regional dataset

On 9 October 2006, 25 May 2009, and 12 February 2013, North Korea conducted three successive nuclear tests near the China-Korea border, and their body wave magnitudes were 4.2, 4.7 and 5.1, respectively, as reported by the United States Geological Survey (USGS). Hereafter, these events are referred to as NKT1, NKT2 and NKT3, and their parameters are provided in Table 1. Broadband digital seismograms from these nuclear tests are collected. Figure 1 depicts the locations of the North Korean nuclear test site (NKTS) and the 297 broadband stations used in this study. Among them, 188 permanent stations are from the national and provincial networks under the China Earthquake Administration (CEA) and the China National Digital Seismic Network (CNDSN) operated by the China Earthquake Networks Center (CENC) since December 2000. Seven permanent stations are from the Global Seismographic Network (GSN), which has been operated by the USGS and the Incorporated Research Institutions for Seismology (IRIS) consortium from May 1994 to present. Two portable seismic arrays, including the 6 station SASK in South Korea and the 35 station NECsaids in Northeast China, originally for investigating deep structures, recorded NKT2 and NKT3 with high signal-to-noise ratios. The remaining 61 stations are from F-NET in Japan. These stations are equipped with broadband instruments with nearly flat velocity responses between 0.03 and 8.0 Hz or wider, and their sampling rates vary among 20, 40, 50, and 100 points per second. The distances from the NKTS to these stations are between 143 and 1930 km, within which the Pn phase is well-developed.

We plot regional waveforms in a record section to investigate the Pn-wave group velocity in this area. Instead of plotting waveforms themselves, we plot normalized waveform energy. Figure 2a presents a vertical-component velocity seismogram from NKT3 recorded by station LN.LYA at a distance of 813.0 km, where a bandpass filter between 0.1 and 10.0 Hz is applied. Figure 2b shows the normalized waveform energy. Figure 2c presents the waveform energy versus distance, in which several regional phases can be identified. The first arrival is the Pn wave, which has a group velocity of approximately 8.1 km/s. The Pg- and Lg-waves can be traced at group velocities of 6.0 and 3.5 km/s, respectively.

2.2 Pn amplitude measurements

The Pn wave is typically the first arrival at regional distances, and its amplitude can be measured within a time or group velocity window. For example, a fixed 5-second time window was used in Scandinavia by *Sereno et al.* [1988], a 4.3-second window was used in Eastern Canada by *Zhu et al.* [1991], and a 4.5-second window was used in Tibet by *Xie* [2007]. Considering the slightly dispersive properties of the Pn wave, some authors have used a group velocity window between 8.2 and 7.6 km/s to measure the amplitude [e.g., *Al-Damegh et al.*, 2004; *Mcnamara et al.*, 1997; *Reese et al.*, 1999]. In this study, we use the vertical-component seismogram and a 0.7 km/s group-velocity window around the IASP91 arrival time to measure the Pn amplitude. Figure 3 briefly illustrates the data processing process. The vertical-component seismogram recorded at station LN.LYA from NKT3 is presented in Figure 3a, where the gray-shaded areas indicate the 0.7 km/s group velocity window for measuring Pn and the pre-P-arrival window for sampling the noise. The windowed signal is plotted in Figure 3b, where 10% cosine tapers are applied at both ends. Following *Zhao et al.* [2010, 2013b], we select the noise series in an equal-length time window before the first arrival. Figure 3c presents the calculated Fourier spectra of the Pn and noise series between 0.3 and 15.0 Hz. The Pn spectral amplitudes are obtained at 44 frequencies distributed log-evenly between 0.3 and 15.0 Hz and corrected for the noise (Figures 3d and 3e). (for details, see *Zhao et al.*, 2013a; *Zhao et al.*, 2010).

3 Pn-wave geometric spreading and attenuation

3.1 Modeling of the Pn spectrum

The Pn-wave spectrum can be expressed as [*Sereno et al.*, 1988; *Xie*, 2007; *Xie and Patton*, 1999]:

$$A(f) = S(f)\cdot G(\Delta, f)\cdot \Gamma(\Delta, f)\cdot P(f)\cdot r(f), \tag{1}$$

where f is the frequency, $A(f)$ is the observed spectral amplitude, $P(f)$ is the site response, and $r(f)$ is the random amplitude effect. $S(f)$ is the Pn source spectrum, which is given by the following simplified explosion source function [*Hong*, 2013; *Mueller and Murphy*, 1971; *Sereno et al.*, 1988; *Xie and Patton*, 1999]:

$$S(f) = S_0 \cdot \left[1 + (1-2\beta)\frac{f^2}{f_c^2} + \beta^2 \frac{f^4}{f_c^4}\right]^{-1/2}, \tag{2}$$

where S_0 is the long period source spectral level, f_c is the corner frequency, and β controls the amount of overshot. For a Poisson medium, β = 0.75. For a near-surface explosion, $S_0 = M_0 / 4\pi\rho\alpha^3$, where M_0 is the seismic moment, and ρ and α are the density and P-wave velocity in the source region [*Sereno et al.*, 1988; *Stevens and Day*, 1985], which in this study are set to 2.7 g/cm^3 and 5.5 km/s [*Hong et al.*, 2008; *Jih*, 1998], respectively. In Equation (1), the geometric spreading factor $G(\Delta, f)$ is a function of the epicenter distance Δ and frequency f, and its details are provided in the next section. In Equation (1),

$$\Gamma(\Delta, f) = \exp\left[-\frac{\pi f}{V} B(\Delta, f)\right] \tag{3}$$

is the attenuation factor, where V is the Pn-wave group velocity, and will be treated as a regional constant,

$$B(\Delta, f) = \int_{ray} \frac{ds}{Q(f)} \tag{4}$$

is the integral of attenuation over the great circle path. In addition, $Q(f)$ is the apparent Pn-wave Q and assumed can be expressed by a power-law model [e.g., *Sereno et al.*, 1988; *Xie*, 2007]:

$$Q(f) = Q_0 f^{\eta}, \tag{5}$$

where Q_0 and η are the apparent Pn-wave Q at 1 Hz and its frequency-dependence, respectively.

3.2 Pn-wave geometric spreading function

The power-law spreading function linearly relates the logarithmic amplitude with the logarithmic distance. To account for the complex spreading relation obtained from the Pn-wave simulation in a spherical Earth, *Yang et al.* [2007] extended the power-law relation by adding a second-order term. Considering that Pn spreading is frequency dependent, these researchers also included a quadratic form for its frequency dependency. We will call the model the log-quadratic spreading model, which exhibits the following form [*Yang et al.*, 2007]:

$$G(\Delta, f) = 10^{\xi_3(f)} \Delta^{\xi_1(f)\log_{10}\Delta - \xi_2(f)}, \tag{6}$$

where coefficients $\xi_n(f)$ are dependent on the logarithm of the frequency

$$\xi_n(f) = \xi_{n1} \log_{10}^2(f) + \xi_{n2} \log_{10}(f) + \xi_{n3}, \quad (n = 1, 2, 3). \tag{7}$$

Based on a spherical earth model composed of a 40-km thick crust and an underlying constant upper mantle, *Yang et al.* [2007] used numerical simulation to determine the coefficients as

$$= \begin{bmatrix} -0.217 & 1.79 & 3.16 \\ -1.94 & 8.43 & 18.6 \\ -3.39 & 9.94 & 20.7 \end{bmatrix}. \tag{8}$$

Equation (6) is likely a more flexible model for the Pn geometric spreading than the simple power-law model, but its coefficients can vary for regions with different velocities, crust thickness, and upper mantle lid structures. Therefore, we adopt equation (6) for Northeast China and the Korean Peninsula but fine-tune its parameters using observed Pn data.

3.2.1 Prior information and model space

Table 2 summarizes the model parameters to be searched for, including four parameters for sources, nine geometric spreading coefficients, and two parameters for the apparent Pn-wave Q. We estimate the variation range of these parameters. For the three North Korean nuclear tests, their seismic moment M_0 and the corner frequency f_c can be calculated from their body-wave magnitude m_b using the empirical relationship established by *Taylor et al.* [2002]. We set $\pm 10\%$ perturbations for m_b to obtain the variation ranges for M_0. The source corner frequency f_c can be calculated from the seismic moment using the empirical relation $\log M_0 = a + b \cdot \log f_c$ from *Xie and Patton* [1999]. From the Pn data recorded for explosions in central Asia, these researchers found $a = 18.34$ and $b = 4.73$. There is likely a tradeoff between M_0 and a, so we fix $a = 18.34$ in our model. The slope b also exhibits certain regional dependence, so we allow $\pm 30\%$ variation for this parameter. The log-quadratic Pn spreading model derived by *Yang et al.* [2007] is expected to be transferable to other regions with proper modification of its parameters. Thus, we impose ±10% perturbation for all 9 coefficients. *Sereno et al.* [1988] obtained apparent attenuation of $Q(f) = 325 f^{0.48}$ in Scandinavia using 1 to 15 Hz Pn spectra. *Sereno* [1990] investigated Pn amplitude spectra in eastern Kazakhstan in central Asia and obtained a similar power-law Q model of $Q(f) = 300 f^{0.5}$. *Chun et al.* [1989] suggested that a frequency-dependent Q model, $Q(f) = 255 f^{0.74}$, can explain the observed Pn spectra in the Canadian shield between 3 and 10 Hz. *Xie* [2007] used 0.6 to 5.0 Hz Pn spectra to obtain an average Q model, $Q(f) = 278 f^{0.14}$, for the Tibetan plateau. *Yang* [2011] investigated Pn geometric spreading based on observations in Asia, wherein he observed that the Pn Q approximately follows a power-law function $Q(f) = 204 f^{0.58}$ for frequencies greater than 2 Hz. Using these results as prior information, we limit the range of Q_0 and η from 200 to 600 and from -0.2 to 1.2, respectively. All prior information and model parameter spaces are summarized in Table 2.

3.2.2 Pn geometric spreading model in Northeast China and the Korean Peninsula

Because of the potentially different Pn propagation characteristics of continental and oceanic paths, and because the continental dataset covers a wide and relatively even distance range, we use only continental-path Pn amplitude measurements in the following parameter searching and tomography analysis. We also restrict our analysis to amplitudes within 2.0 to 10.0 Hz due to apparently different Pn attenuation behavior (see Figure 7d) beyond this frequency range. Simulated annealing [*Kirkpatrick et al.*, 1983], a non-exhaustive global optimization algorithm, is used to estimate the parameters in model space. This method has been widely applied in geophysical modeling [e.g., *Iritani et al.*, 2014; *Kirkpatrick*, 1984; *Zhao et al.*, 1996]. We perform the parameter searching by minimizing the L2 norm misfit function of the difference

Approved for public release; distribution is unlimited.

between observed and synthetic Pn amplitudes. Figure 4 illustrates the Pn spectral amplitudes at selected frequencies, after correcting for the source excitation functions. Different symbols indicate that the samples are from NKT1 (triangles), NKT2 (circles) and NKT3 (crosses). The solid blue lines are the best-fit Pn amplitudes from data between 2.0 and 10.0 Hz, and the shaded areas are their standard deviations of the fit calculated using the bootstrap method [*Efron*, 1983]. The frequency *f*, number of samples N, apparent regional average Pn Q, and correlation coefficient R are labeled in each panel.

The inverted Pn models are listed in Table 2 and illustrated in Figure 5. Figures 5a and 5b presents the Pn geometric spreading curves versus distance at 2.1 and 9.1 Hz, respectively. Figures 5c and 5d present these curves versus frequency at distances of 500 and 1,200 km, respectively. The solid lines indicate the results obtained here, and the dashed lines represent the model proposed by *Yang et al.* [2007]. The two spreading models exhibit similar overall shapes that first decrease and then increase with increasing distance. The minimums appear at shorter distances for higher frequencies. The models are also positively frequency dependent, at least within the investigated frequency band. Figure 5e illustrates the inverted source excitation functions, where the shaded areas are the standard deviations. Figure 5f presents the average regional Pn Q versus the frequency.

4 Upper mantle P-wave attenuation

Pn-wave attenuation is an apparent value because the Pn Q observed along the great circle is mixed with those traveling in the uppermost mantle and crust, with the latter propagating with a nonzero dipping angle. With the known Pn-wave geometric spreading function, we can strip the effect of crust legs and obtain the upper mantle P-wave attenuation.

4.1 Single-station data

Figure 6 presents the Pn propagation path between the NKTS and station LN.LYA, calculated using the CRUST1.0 model [*Laske et al.*, 2013]. The refraction points E and F separate the ray path into three sections, including the crust leg at the source side, the uppermost mantle leg, and the crust leg at the station side. From equation (4), $B(\Delta, f)$ can be expressed as

$$B(\Delta, f)=\int_{AE}\frac{ds}{Q_s}+\int_{EF}\frac{ds}{Q(x,y,f)}+\int_{FB}\frac{ds}{Q_r}, \tag{9}$$

where Q_s and Q_r are the source and station side crust P-wave Q, and $Q(x,y,f)$ is the uppermost mantle P-wave Q, which is a function of the frequency and location (x,y) between E and F. By substituting Equation (9) into (3), the Pn attenuation factor can be expressed as

$$\begin{aligned}\Gamma(\Delta, f)&=\Gamma_s(AE,f)\cdot\Gamma(EF,f)\cdot\Gamma_r(FB,f)\\&=\exp\left[-\frac{\pi f}{\alpha_{1s}}\int_{AE}\frac{ds}{Q_s}-\frac{\pi f}{\alpha_2}\int_{EF}\frac{ds}{Q(x,y,f)}-\frac{\pi f}{\alpha_{1r}}\int_{FB}\frac{ds}{Q_r}\right],\end{aligned} \tag{10}$$

where α_{1s} and α_{1r} are the source and station side P-wave velocity, α_2 is the upper mantle P-wave velocity. From equations (1) and (10), we have

Approved for public release; distribution is unlimited.

$$A(f)G^{-1}(\Delta, f)\cdot S^{-1}(f)=\left[\Gamma_s(AE, f)\Gamma_r(FB, f)\right]\cdot\exp\left[-\frac{\pi f}{\alpha_2}\int_{EF}\frac{ds}{Q(x, y, f)}\right], \tag{11}$$

where $G(\Delta, f)$ and $S(f)$ are known from Section 3, and $A(f)G^{-1}(\Delta, f)\cdot S^{-1}(f)$ is the spreading and source corrected single-station data. $\Gamma_s(AE, f)\cdot\Gamma_r(FB, f)$ is the attenuation from the crust legs. We assume it is an unknown constant over the studied region and can be inverted for from the data. It is expected that the upper mantle leg dominates the Pn propagation, and the error in the crust legs can be neglected. We will also neglect factors $P(f)$ and $r(f)$ caused by the site effect and the random fluctuations.

4.2 Two-station data and Pn amplitude ratio

Assuming that the two stations are located at different epicenter distances but within the similar azimuth direction from the NKTS, we calculate their amplitude ratio as follows [e.g., *Xie et al.*, 2004]:

$$A_{ij}=\frac{A_j(f)}{A_i(f)}=\frac{G(\Delta_j, f)}{G(\Delta_i, f)}\frac{\Gamma_s(AE_j, f)}{\Gamma_s(AE_i, f)}\frac{\Gamma(EF_j, f)}{\Gamma(EF_i, f)}\frac{\Gamma_r(FB_j, f)}{\Gamma_r(FB_i, f)}\frac{P_j(f)\cdot r_j(f)}{P_i(f)\cdot r_i(f)}, \tag{12}$$

where $A_i(f)$ and $A_j(f)$ are the Pn amplitude spectra observed at stations i and j, the source terms have been canceled, and $G(\Delta_j, f)/G(\Delta_i, f)$ is the ratio between known geometrical spreading functions at these distances. $\Gamma_s(AE_i, f)$ and $\Gamma_s(AE_j, f)$ represent the source side crust legs. For observations from the same source, their ratio should be equal to unity. $\Gamma_r(FB_i, f)$ and $\Gamma_r(FB_j, f)$ represent the station side crust legs. As above mentioned, we assume these values are approximately the same, and their ratio approaches unity. We also neglect the ratio $P_j(f)\cdot r_j(f)/P_i(f)\cdot r_i(f)$. After these treatments and by introducing equation (10), equation (12) becomes

$$A_{ij}(f)\frac{G(\Delta_i, f)}{G(\Delta_j, f)}=\exp\left[-\frac{\pi f}{\alpha_2}\int_{F_i}^{F_j}\frac{ds}{Q(x, y, f)}\right], \tag{13}$$

where the integral $\int_{F_i}^{F_j} 1/Q(x, y, f)\,ds$ is from the refraction point F_i to F_j over the upper mantle path. The left hand side of equation (13), the amplitude ratio corrected by the known geometrical spreading function, is directly linked to the accumulated attenuation over the pure upper mantle path. Thus, the two-station amplitude ratio strips the source term and contributions from the crust legs near the source and station.

Figures 7a to 7c illustrate the Pn amplitude ratios after correction for the spreading function versus the interstation distance at 3.0, 5.2 and 9.1 Hz. The solid lines are linear regressions, and their slopes provide the regional average upper mantle P-wave Q. The circles in Figure 7d represent upper mantle P-wave Q versus frequency. They show a nearly linear relation between 2.0 and 10.0 Hz (shaded area), within which a power-law Q model, $Q_P=176f^{0.48}$, for the upper mantle P wave can be obtained. However, outside this frequency band, the Q versus frequency behaves quite differently. In our Pn Q model, we assume a power-law frequency dependence. The results demonstrate that this assumption may only be valid within the 2.0 to 10.0 Hz band in the studied region.

4.3 Upper mantle P-wave Q tomography

An inversion system for the upper mantle P-wave Q can be created either from the single-station data, the two-station data, or by combining both. One might think that the two datasets are from the same group of observations and should contain exactly the same information, but certain differences still exist. The advantage of using the two-station data is that the amplitude ratio eliminates the source effect at the data processing stage, reducing the tradeoff between the source term and attenuation in the inversion. However, the slight azimuth difference between two stations may result in additional errors. Most importantly, the two-station data must match the source-station geometry, which often results in less useful rays and shorter ray length compared with the single-station method. This effect is particularly severe for the heavily attenuated region and for high frequencies, where near-station information is vital. Thus, combining the single- and two-station data improves data coverage and avoids serious tradeoffs.

Similar to the Lg-wave Q tomography [e.g., *Zhao et al.*, 2010, 2013b], we linearize equations (11) and (13) by taking the logarithm to combine both the single- and two-station data for inversion. In our tomography, the initial Q model is a constant model resulted from two-station data analysis, as shown in Figure 7. The constant Q model is also used to create checkerboard-shaped model by superimposing positive and negative perturbations. A broadband uppermost mantle P-wave attenuation model in Northeast China and the Korean Peninsula at 18 discrete frequencies between 2.0 and 10.0 Hz is obtained. As examples, Figure 8a presents the P-wave Q distribution at 3.0 Hz, and Figure 8b presents the broadband Q, which is calculated by average logarithmic Q between 2.0 and 10.0 Hz. The major geology blocks, including the Songliao Basin (SB), Bohai Bay Basin (BB) and Changbai Mountains (CM), are illustrated in these figures. The northern SB, the areas between the southern SB and BB, and the southeastern CM are characterized by low Q anomalies, whereas areas between SB and CM are high Q regions. A number of volcanoes in this region were previously investigated using seismic velocity tomography [e.g., *Duan et al.*, 2009; *Lei and Zhao*, 2005; *Zhao et al.*, 2009; *Zhao et al.*, 2011]. Prominent low P-wave velocity anomalies have been found in the crust and upper mantle beneath these volcanoes [*Zhao et al.*, 2009]. These anomalies are consistent with the strong P-wave attenuation in the uppermost mantle observed in this study. Figures 8c and 8d illustrate the 3.0-Hz ray coverage and the checkerboard test for the 2.0° × 2.0° resolution.

5 Comparison of Pn-wave amplitudes through continental and oceanic paths

The ray paths from NKTS to Japan cross the Japan Sea, where the oceanic Moho depth is approximately 11 to 15 km [*Laske et al.*, 2013]. The continental crust and oceanic crust have different thicknesses and underlying upper mantle P-wave velocities, and the transition zone between them may also influence Pn attenuation and spreading. In Figure 1, the data observed via continental path surround the NKTS for an azimuth range of approximately 160º and cover epicenter distances from 150 to 1300 km, forming the dataset for investigating the Pn spreading function and attenuation in Northeast China and the Korean Peninsula. The data crossing the oceanic path are mostly recorded by F-NET stations in Japan. The data cover an azimuth range of approximately 120º but are mostly

Approved for public release; distribution is unlimited.

recorded at distances of approximately 1,000 km, thus preventing them from being used for an independent geometric spreading function for the oceanic path.

Given that the explosion sources are virtually isotropic and the observations are nearly completely surrounding the source, the data still provide an excellent opportunity to investigate the Pn amplitudes and their frequency dependency on the continental and oceanic paths. To avoid ambiguity, we make a straight forward comparison with minimum data processing. Given that the oceanic data are mostly recorded at 1,000 km, we collect the Pn spectral amplitudes between distances 800 and 1,200 km (with a nominal epicentral distance of 1,000 km). We remove the Pn-wave source excitation functions and present the result in Figure 9 as a function of the azimuth. The triangles, circles and crosses are the directly measured spectral amplitudes for NKT1, NKT2 and NKT3. In addition, black, blue and red colors indicate 0.8-, 7- and 10.0-Hz data, respectively. Solid circles with error bars indicate the mean values and standard deviations obtained within a 30º azimuth window. Prominent differences can be observed for the Pn waves crossing different paths. Between 60º and 180º, the Pn signals crossing the oceanic path are strongly frequency dependent, with extremely low high-frequency amplitudes. The Pn waves across the continental path can be divided into two groups. Between 230º and 280º with the direction towards Northern China, the low-frequency contents (0.8 and 7 Hz) are similar to that from the oceanic path, but the high-frequency (10 Hz) propagation is much more efficient than that from the oceanic path. Within the azimuth range of 315º to 30º towards Northeast China, the Pn spectra are less dependent on the frequency. In general, the intermediate frequency (7 Hz) spectra are less affected by different paths, but the low- and high-frequency contents exhibit apparent variations between the continental and oceanic paths. Because no data processing, other than the noise and source excitation function removal is involved, the observations are relatively reliable. The spreading function tends to raise the high-frequency signal, whereas attenuation tends to reduce the high-frequency contents. The detailed structure of transition zones may also affect the frequency dependence. Additional observational and/or numerical investigations are required to distinguish contributions from individual mechanisms.

6 Discussion

To determine the Pn wave geometric spreading function and the attenuation, several assumptions are adopted, e.g., isotropic source radiation, a log-quadratic spreading model, and a power-law Pn Q model. Given that both geometric spreading and attenuation are frequency dependent, tradeoffs between them may exist. Certain clues (e.g., Figure 7d) indicate that a power-law Q model may oversimplify the frequency dependency of the attenuation in a broad frequency band. In Section 3, we obtain the regional average Pn Q using the single-station data, and we obtain the regional average upper mantle P wave Q using the two-station data in Section 4. However, because the single-station data extend to a larger region compared with the two-station data, the two average Qs do not necessarily cover the same region. In the upper mantle P wave attenuation tomography, all seismic rays come from the same epicenter and there are no crossing rays. This forms an unfavorable geometry for a high-quality tomography. Therefore, the result is limited and primarily used for introducing the technique.

The Pn-wave has a typical group velocity window between 8.2 and 7.6 km/s for continental paths. Selecting a window and the component to measure the Pn spectra is an

Approved for public release; distribution is unlimited.

important issue. *Sereno et al.* [1988] tested different window lengths of 5 to 20 s and suggested that the spectra are insensitive to the window length. In fact, their shortest 5-second window generated approximately the same Pn measurements for low-magnitude earthquakes with epicentral distances between 200 and 1400 km. To investigate the stability of the Pn-wave amplitude measurement, we tested four different methods, including combinations from two different Pn-wave windows (a 0.7 km/s group-velocity window around the IASP91 arrival times and a fixed 4-second window after the first arriving P wave) and two different displacement components (vertical component and the displacement rotated to the Pn incident direction). The methods generally exhibit consistent results. Therefore, we only present the result from the vertical component and a 0.7 km/s group-velocity window.

7 Conclusions

We present a method to separate the geometric spreading and attenuation from the seismic Pn-wave data. The frequency-dependent, log-quadratic spreading function of *Yang et al.* [2007] and the power-law Q model are adopted for Pn propagation. A high-accuracy broadband Pn-wave dataset from the recent North Korean nuclear explosions is used to constrain the model parameters. The geometric spreading function and regional Pn Q are obtained for Northeast China and the Korean Peninsula. By taking the two-station amplitude ratios and correcting for the known spreading function, we remove the effects of the source and crust legs from Pn data, obtaining the P-wave attenuation information along the pure upper mantle path. Combining both the single- and two-station data, the upper mantle P-wave attenuation distribution is obtained using a formal tomographic approach. The current method can be applied to earthquake data as well as Sn waves. We compared the Pn waves across China and through the Japan Sea. The results reveal prominent differences for Pn waves crossing different paths, with the high-frequency Pn signal propagating more efficiently through the continental path compared with the oceanic path.

Acknowledgments

The comments from Prof. Thomas M. Hearn and another anonymous reviewer are valuable, and greatly improved this manuscript. This research was supported by the National Natural Science Foundation of China (grants 41174048, 41374065, 41130316, 4062140435 and 41210005). X.B. Xie wishes to thank AFRL for support under grant FA9453-12-C-0234. The waveforms recorded at the CNDSN, GSN, and F-NET stations used in this study were collected from the China Earthquake Network Center (CENC), the Data Management Centre of the China National Seismic Network at the Institute of Geophysics, the China Earthquake Administration (SEISDMC, doi:10.7914/SN/CB) [*Zheng et al.*, 2010], the Incorporated Research Institutions for Seismology Data Management Center (IRIS DMC) at www.iris.edu (last accessed April 2015), and the National Research Institute for Earth Science and Disaster Prevention (NIED) at http://www.fnet.bosai.go.jp (last accessed April 2015). The seismograms recorded at the SASK and NECsaids stations were provided by the Seismic Array Laboratory (SAL) at the Institute of Geology and Geophysics, Chinese Academy of Sciences (IGGCAS). Some of the figures were generated using the Generic Mapping Tools version 4.3.1 (www.soest.hawaii.edu/gmt, last accessed April 2015) [*Wessel and Smith*, 1998].

Approved for public release; distribution is unlimited.

References

Al-Damegh, K., E. Sandvol, A. Al-Lazki, and M. Barazangi (2004), Regional seismic wave propagation (Lg and Sn) and Pn attenuation in the Arabian plate and surrounding regions, *Geophys. J. Int.*, *157*(2), 775-795, doi:10.1111/j.1365-246X.2004.02246.x.

Avants, M., T. Lay, X. B. Xie, and X. N. Yang (2011), Effects of 2D random velocity heterogeneities in the mantle lid and Moho topography on Pn geometric spreading, *Bull. Seism. Soc. Am.*, *101*(1), 126-140, doi:10.1785/0120100113.

Barron, J., and K. Priestley (2009), Observations of frequency-dependent Sn propagation in Northern Tibet, *Geophys. J. Int.*, *179*(1), 475-488, doi:10.1111/j.1365-246X.2009.04318.x.

Buehler, J. S., and P. M. Shearer (2013), Sn propagation in the Western United States from common midpoint stacks of USArray data, *Geophys. Res. Lett.*, *40*(23), 6106-6111, doi:10.1002/2013gl057680.

Calvert, A., E. Sandvol, D. Seber, M. Barazangi, F. Vidal, G. Alguacil, and N. Jabour (2000), Propagation of regional seismic phases (Lg and Sn) and Pn velocity structure along the Africa-Iberia plate boundary zone: tectonic implications, *Geophys. J. Int.*, *142*(2), 384-408, doi:10.1046/j.1365-246x.2000.00160.x.

Červený, V., and R. Ravindra (1971), Theory of seismic head waves, *University of Toronto Press*, *Toronto, Ont.*, *312*, pp.

Chun, K. Y., R. J. Kokoski, and G. F. West (1989), High-frequency Pn attenuation in the Canadian shield, *Bull. Seism. Soc. Am.*, *79*(4), 1039-1053.

Chun, K. Y., Y. Wu, and G. A. Henderson (2009), Lg attenuation near the North Korean border with China, Part I: model development from regional earthquake sources, *Bull. Seism. Soc. Am.*, *99*(5), 3021-3029, doi:10.1785/0120080316.

Duan, Y. H., D. P. Zhao, X. K. Zhang, S. H. Xia, Z. Liu, F. Y. Wang, and L. Li (2009), Seismic structure and origin of active intraplate volcanoes in Northeast Asia, *Tectonophysics*, *470*(3-4), 257-266, doi:10.1016/j.tecto.2009.01.004.

Efron, B. (1983), Estimating the error rate of a prediction rule: Improvement on cross-validation, *J. Am. Stat. Assoc.*, *78*(382), 316-331, doi:10.2307/2288636.

Hill, D. P. (1973), Critically refracted waves in a spherically symmetric radially heterogeneous earth model, *Geophys. J. Roy. Astr. Soc.*, *34*(2), 149-177, doi:10.1111/j.1365-246X.1973.tb02390.x.

Hong, T. K. (2013), Seismic discrimination of the 2009 North Korean nuclear explosion based on regional source spectra, *J. Seismol.*, *17*(2), 753-769, doi:10.1007/s10950-012-9352-1.

Hong, T. K., C. E. Baag, H. Choi, and D. H. Sheen (2008), Regional seismic observations of the 9 October 2006 underground nuclear explosion in North Korea and the influence of crustal structure on regional phases, *J. Geophys. Res.*, *113*(B3), B03305, doi:10.1029/2007jb004950.

Hong, T. K., and J. Rhie (2009), Regional source scaling of the 9 October 2006 underground nuclear explosion in North Korea, *Bull. Seism. Soc. Am.*, *99*(4), 2523-2540, doi:10.1785/0120080007.

Iritani, R., N. Takeuchi, and H. Kawakatsu (2014), Intricate heterogeneous structures of the top 300 km of the Earth's inner core inferred from global array data: II.

Approved for public release; distribution is unlimited.

Frequency dependence of inner core attenuation and its implication, *Earth Planet. Sci. Lett.*, *405*, 231-243, doi:10.1016/j.epsl.2014.08.038.

Jih, R. S. (1998), Location calibration effects in China, *in Proceedings, 20th Annual Seismic Research Symposium on Monitoring a Comprehensive Test Ban Treaty, 21-23 September 1998*, 44-45.

Kirkpatrick, S. (1984), Optimization by simulated annealing: Quantitative studies, *J. Stat. Phys.*, *34*(5-6), 975-986, doi:10.1007/Bf01009452.

Kirkpatrick, S., C. D. Gelatt, and M. P. Vecchi (1983), Optimization by simulated annealing, *Science*, *220*(4598), 671-680, doi:10.1126/science.220.4598.671.

Laske, G., G. Masters., Z. Ma, and M. Pasyanos (2013), Update on CRUST1.0 - A 1-degree global model of Earth's crust, *Geophys. Res. Abstracts*, *15,* Abstract EGU2013-2658.

Lei, J. S., and D. P. Zhao (2005), P-wave tomography and origin of the Changbai intraplate volcano in Northeast Asia, *Tectonophysics*, *397*(3-4), 281-295, doi:10.1016/j.tecto.2004.12.009.

McNamara, D. E., W. R. Walter, T. J. Owens, and C. J. Ammon (1997), Upper mantle velocity structure beneath the Tibetan Plateau from Pn travel time tomography, *J. Geophys. Res.*, *102*(B1), 493-505, doi:10.1029/96jb02112.

Mueller, R. A., and J. R. Murphy (1971), Seismic characteristics of underground nuclear detonaions, Part I, Seismic spectrum scaling, *Bull. Seism. Soc. Am.*, *61*(6), 1675-1692.

Murphy, J. R., J. L. Stevens, B. C. Kohl, and T. J. Bennett (2013), Advanced seismic analyses of the source characteristics of the 2006 and 2009 North Korean nuclear tests, *Bull. Seism. Soc. Am.*, *103*(3), 1640-1661, doi:10.1785/0120120194.

Reese, C. C., R. R. Rapine, and J. F. Ni (1999), Lateral variation of Pn and Lg attenuation at the CDSN station LSA, *Bull. Seism. Soc. Am.*, *89*(1), 325-330.

Richards, P. G., and W. Y. Kim (2007), Seismic signature, *Nat. Phys.*, *3*(1), 4-6, doi:10.1038/Nphys495.

Sereno, T. J. (1990), Frequency-dependent attenuation in Eastern Kazakhstan and implications for seismic detection thresholds in the Soviet Union, *Bull. Seism. Soc. Am.*, *80*(6), 2089-2105.

Sereno, T. J., S. R. Bratt, and T. C. Bache (1988), Simultaneous inversion of regional wave spectra for attenuation and seismic moment in Scandinavia, *J. Geophys. Res.*, *93*(B3), 2019-2035.

Sereno, T. J., and J. W. Given (1990), Pn attenuation for a spherically symmetric Earth model, *Geophys. Res. Lett.*, *17*(8), 1141-1144, doi:10.1029/Gl017i008p01141.

Stevens, J. L., and S. M. Day (1985), The physical basis of mb : Ms and variable frequency magnitude methods for earthquake/explosion discrimination, *J. Geophys. Res.*, *90*(B4), 3009-3020, doi:10.1029/Jb090ib04p03009.

Taylor, S. R., A. A. Velasco, H. E. Hartse, W. S. Phillips, W. R. Walter, and A. J. Rodgers (2002), Amplitude corrections for regional seismic discriminants, *Pure Appl. Geophys.*, *159*(4), 623-650.

Wen, L. X., and H. Long (2010), High-precision location of North Korea's 2009 nuclear test, *Seis. Res. Lett.*, *81*(1), 26-29, doi:10.1785/gssrl.81.1.26.

Wessel, P., and W. Smith (1998), New, improved version of the generic mapping tools released, *Eos*, *79*, 579.

Approved for public release; distribution is unlimited.

Xie, J. (2007), Pn attenuation beneath the Tibetan plateau, *Bull. Seism. Soc. Am.*, *97*(6), 2040-2052, doi:10.1785/0120070016.

Xie, J., R. Gök, J. Ni, and Y. Aoki (2004), Lateral variations of crustal seismic attenuation along the INDEPTH profiles in Tibet from Lg Q inversion, *J. Geophys. Res.*, *109*(B10), B10308, doi:10.1029/2004JB002988.

Xie, J. K., and H. J. Patton (1999), Regional phase excitation and propagation in the Lop Nor region of central Asia and implications for P/Lg discriminants, *J. Geophys. Res.*, *104*(B1), 941-954.

Yang, X. (2011), A Pn spreading model constrained with observed amplitudes in Asia, *Bull. Seism. Soc. Am.*, *101*(5), 2201-2211, doi:10.1785/0120100314.

Yang, X., T. Lay, X. B. Xie, and M. S. Thorne (2007), Geometric spreading of Pn and Sn in a spherical Earth model, *Bull. Seism. Soc. Am.*, *97*(6), 2053-2065, doi:10.1785/0120070031.

Zhao, D. P., Y. Tian, J. S. Lei, L. C. Liu, and S. H. Zheng (2009), Seismic image and origin of the Changbai intraplate volcano in East Asia: Role of big mantle wedge above the stagnant Pacific slab, *Phys. Earth Planet. Inter.*, *173*(3-4), 197-206, doi:10.1016/j.pepi.2008.11.009.

Zhao, D. P., S. Yu, and E. Ohtani (2011), East Asia: Seismotectonics, magmatism and mantle dynamics, *J. Asian Earth Sci.*, *40*(3), 689-709, doi:10.1016/j.jseaes.2010.11.013.

Zhao, L. F., X. B. Xie, J. K. He, X. B. Tian, and Z. X. Yao (2013a), Crustal flow pattern beneath the Tibetan plateau constrained by regional Lg-wave Q tomography, *Earth Planet. Sci. Lett.*, *383*, 113-122, doi:10.1016/j.epsl.2013.09.038.

Zhao, L. F., X. B. Xie, W. M. Wang, and Z. X. Yao (2008), Regional seismic characteristics of the 9 October 2006 North Korean nuclear test, *Bull. Seism. Soc. Am.*, *98*(6), 2571-2589, doi:10.1785/0120080128.

Zhao, L. F., X. B. Xie, W. M. Wang, and Z. X. Yao (2012), Yield estimation of the 25 May 2009 North Korean nuclear explosion, *Bull. Seism. Soc. Am.*, *102*(2), 467-478, doi:10.1785/0120110163.

Zhao, L. F., X. B. Xie, W. M. Wang, and Z. X. Yao (2014), The 12 February 2013 North Korean underground nuclear test, *Seis. Res. Lett.*, *85*(1), 130-134, doi:10.1785/0220130103.

Zhao, L. F., X. B. Xie, W. M. Wang, J. H. Zhang, and Z. X. Yao (2010), Seismic Lg-wave Q tomography in and around Northeast China, *J. Geophys. Res.*, *115*, B08307, doi:10.1029/2009JB007157.

Zhao, L. F., X. B. Xie, W. M. Wang, J. H. Zhang, and Z. X. Yao (2013b), Crustal Lg attenuation within the North China Craton and its surrounding regions, *Geophys. J. Int.*, *195*(1), 513-531, doi:10.1093/gji/ggt235.

Zhao, L. S., M. K. Sen, P. Stoffa, and C. Frohlich (1996), Application of very fast simulated annealing to the determination of the crustal structure beneath Tibet, *Geophys. J. Int.*, *125*(2), 355-370, doi:10.1111/j.1365-246X.1996.tb00004.x.

Zheng, X. F., Z. X. Yao, J. H. Liang, and J. Zheng (2010), The role played and opportunities provided by IGP DMC of China National Seismic Network in Wenchuan earthquake disaster relief and researches, *Bull. Seism. Soc. Am.*, *100*(5B), 2866-2872, doi:10.1785/0120090257.

Zhu, T. F., K. Y. Chun, and G. F. West (1991), Geometrical spreading and Q of Pn waves: an investigative study in eastern Canada, Bull. Seism. Soc. Am., 81(3), 882-896.

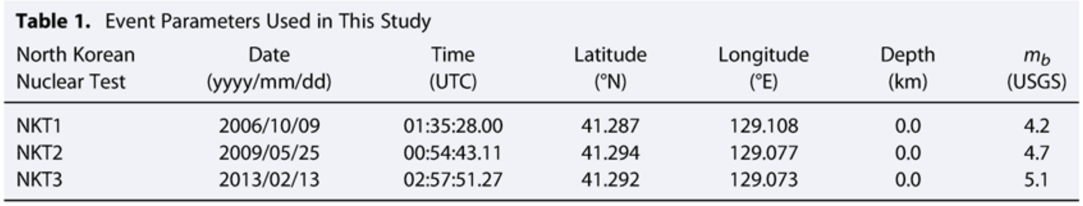

Table 1. Event Parameters Used in This Study

North Korean Nuclear Test	Date (yyyy/mm/dd)	Time (UTC)	Latitude (°N)	Longitude (°E)	Depth (km)	m_b (USGS)
NKT1	2006/10/09	01:35:28.00	41.287	129.108	0.0	4.2
NKT2	2009/05/25	00:54:43.11	41.294	129.077	0.0	4.7
NKT3	2013/02/13	02:57:51.27	41.292	129.073	0.0	5.1

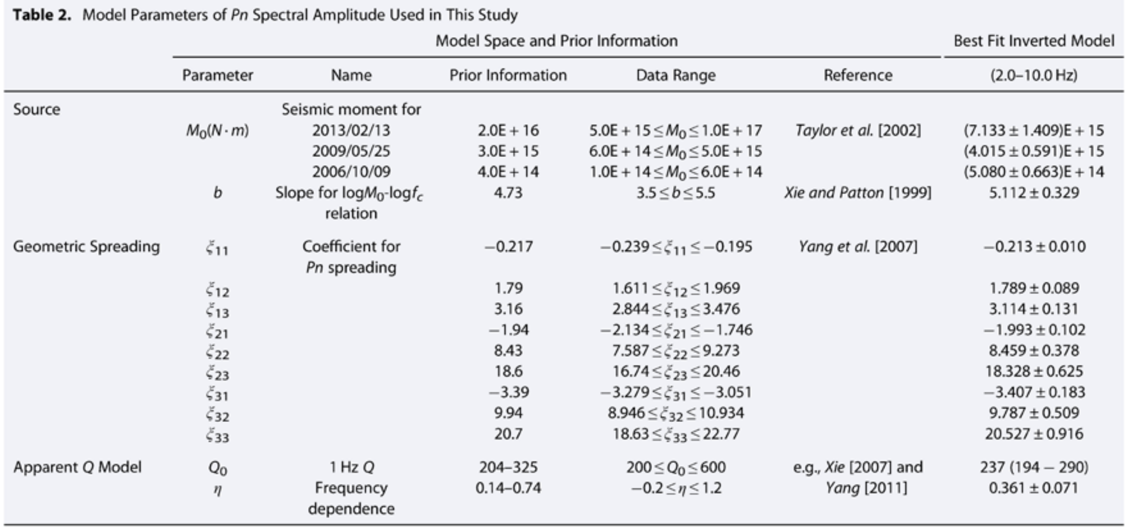

Table 2. Model Parameters of *Pn* Spectral Amplitude Used in This Study

	Model Space and Prior Information					Best Fit Inverted Model
	Parameter	Name	Prior Information	Data Range	Reference	(2.0–10.0 Hz)
Source		Seismic moment for				
	$M_0(N \cdot m)$	2013/02/13	2.0E + 16	$5.0E+15 \leq M_0 \leq 1.0E+17$	*Taylor et al.* [2002]	$(7.133 \pm 1.409)E+15$
		2009/05/25	3.0E + 15	$6.0E+14 \leq M_0 \leq 5.0E+15$		$(4.015 \pm 0.591)E+15$
		2006/10/09	4.0E + 14	$1.0E+14 \leq M_0 \leq 6.0E+14$		$(5.080 \pm 0.663)E+14$
	b	Slope for $\log M_0$-$\log f_c$ relation	4.73	$3.5 \leq b \leq 5.5$	*Xie and Patton* [1999]	5.112 ± 0.329
Geometric Spreading	ξ_{11}	Coefficient for *Pn* spreading	−0.217	$-0.239 \leq \xi_{11} \leq -0.195$	*Yang et al.* [2007]	-0.213 ± 0.010
	ξ_{12}		1.79	$1.611 \leq \xi_{12} \leq 1.969$		1.789 ± 0.089
	ξ_{13}		3.16	$2.844 \leq \xi_{13} \leq 3.476$		3.114 ± 0.131
	ξ_{21}		−1.94	$-2.134 \leq \xi_{21} \leq -1.746$		-1.993 ± 0.102
	ξ_{22}		8.43	$7.587 \leq \xi_{22} \leq 9.273$		8.459 ± 0.378
	ξ_{23}		18.6	$16.74 \leq \xi_{23} \leq 20.46$		18.328 ± 0.625
	ξ_{31}		−3.39	$-3.279 \leq \xi_{31} \leq -3.051$		-3.407 ± 0.183
	ξ_{32}		9.94	$8.946 \leq \xi_{32} \leq 10.934$		9.787 ± 0.509
	ξ_{33}		20.7	$18.63 \leq \xi_{33} \leq 22.77$		20.527 ± 0.916
Apparent *Q* Model	Q_0	1 Hz *Q*	204–325	$200 \leq Q_0 \leq 600$	e.g., *Xie* [2007] and *Yang* [2011]	237 (194 − 290)
	η	Frequency dependence	0.14–0.74	$-0.2 \leq \eta \leq 1.2$		0.361 ± 0.071

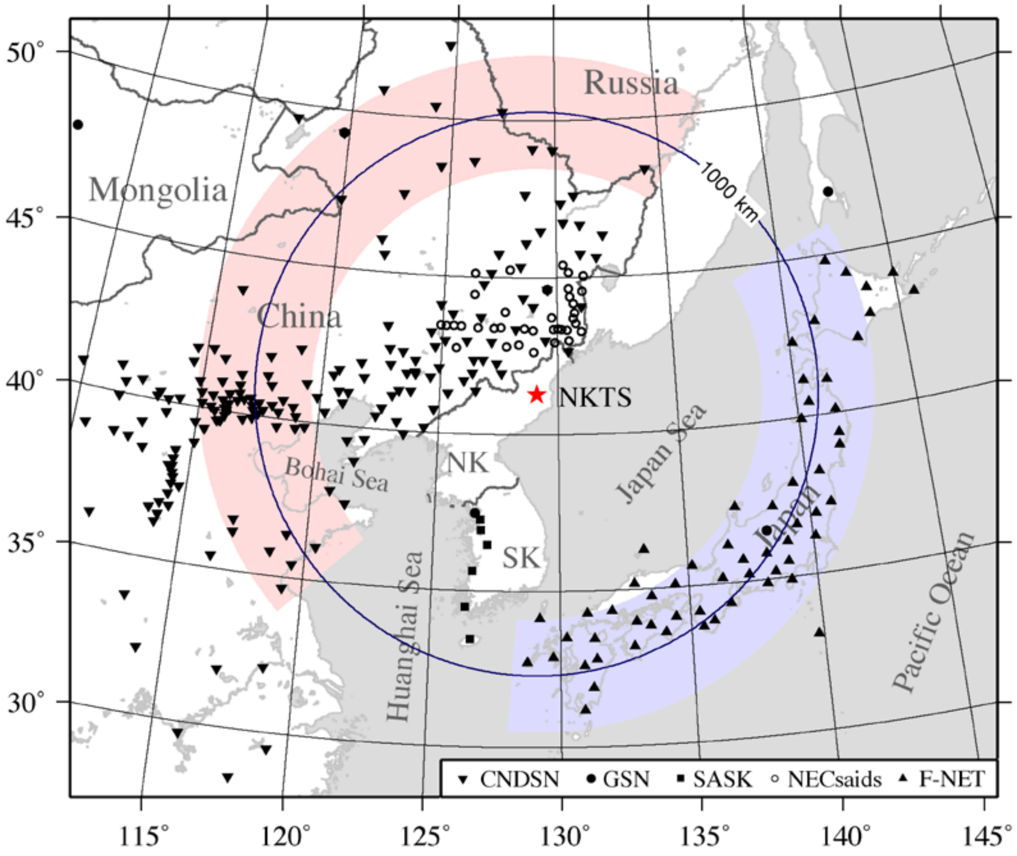

Figure 1. Map depicting locations of the North Korean test site (red star labeled NKTS) and seismic stations used in the study, including CNDSN (upset down triangles), GSN (solid circles), SASK (squares), NECsaids (open circles), and F-NET (triangles). The large circle indicates the 1000-km epicentral distance from the NKTS, with the pink and blue colors marking stations with continental and oceanic paths, respectively.

Approved for public release; distribution is unlimited.

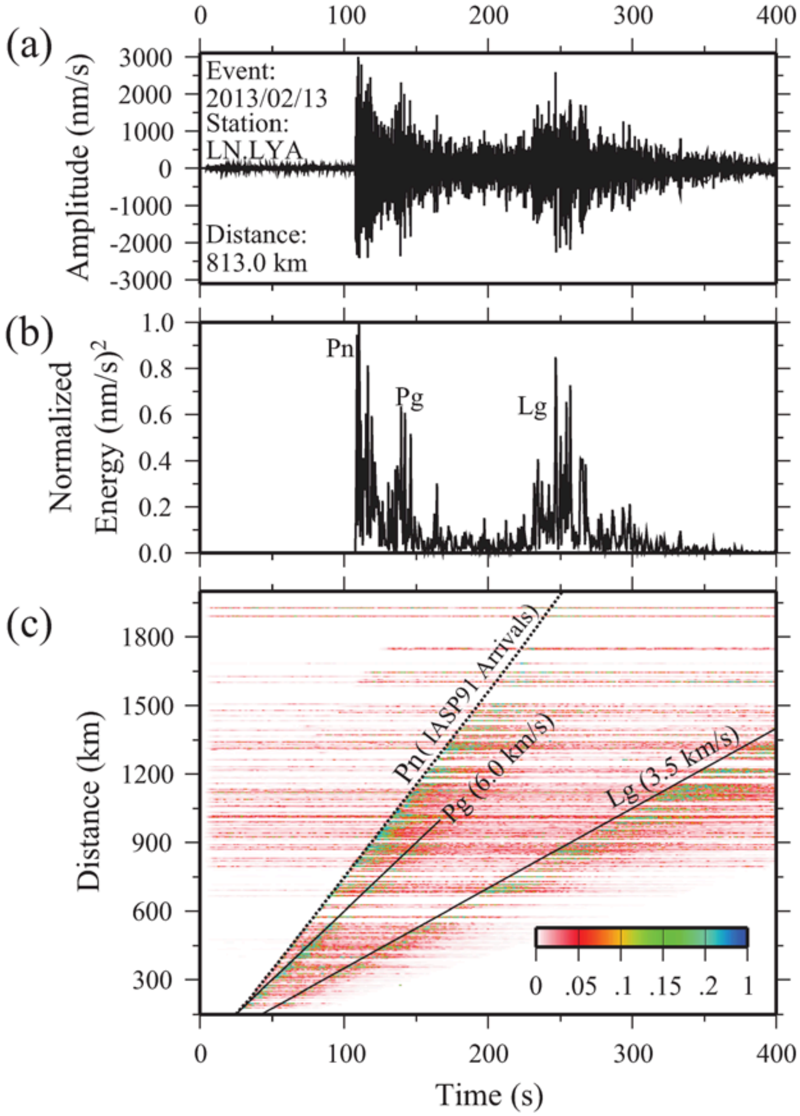

Figure 2. (a) A sample seismogram recorded at station LN.LYA, (b) its normalized energy, and (c) the record section of normalized waveform energy for all data used in this study. Color bar indicates the normalized energy level. The regional phases Pn, Pg, and Lg are labeled in (b) and (c).

Approved for public release; distribution is unlimited.

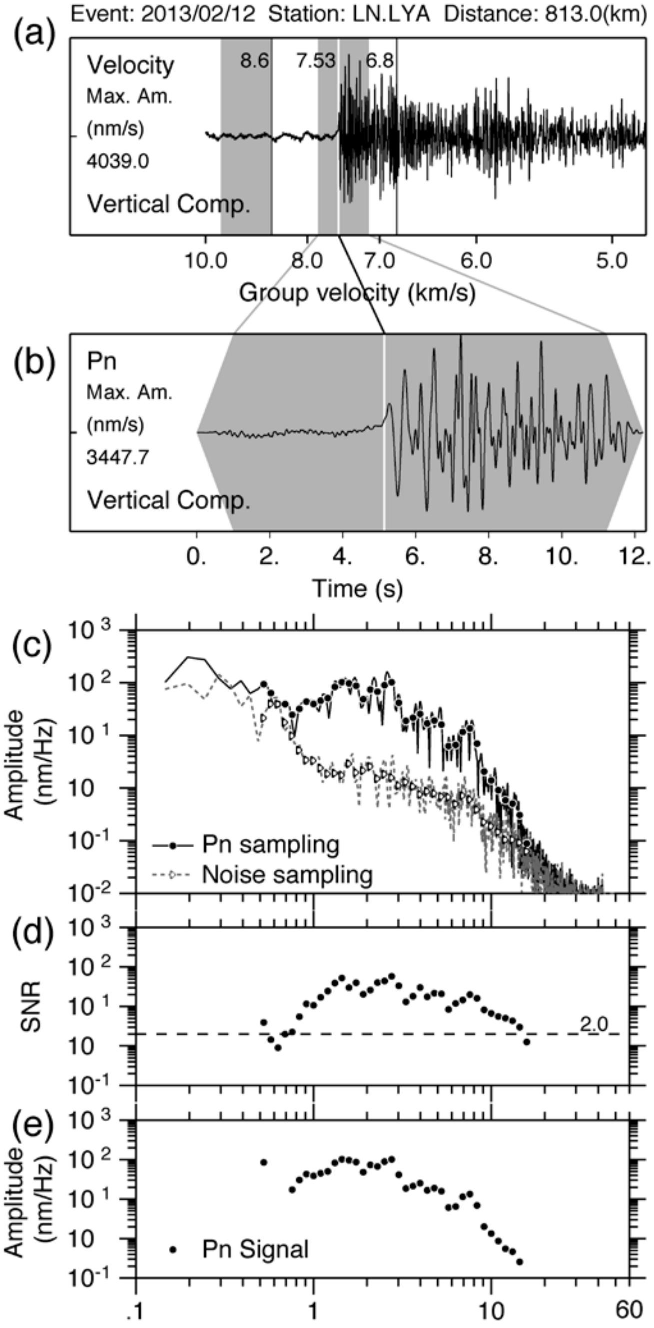

Figure 3. Pn wave spectral amplitude measurement. (a) Vertical-component Pn seismogram, with the shaded areas indicating windows for Pn and the pre-signal noise, (b) Pn phase sampled by a 0.7-km/s group velocity window, (c) Pn-wave and noise spectra,

(d) signal-to-noise ratio (SNR), and (e) Pn spectra after noise correction. Note that the data samples for SNR < 2.0 are eliminated.

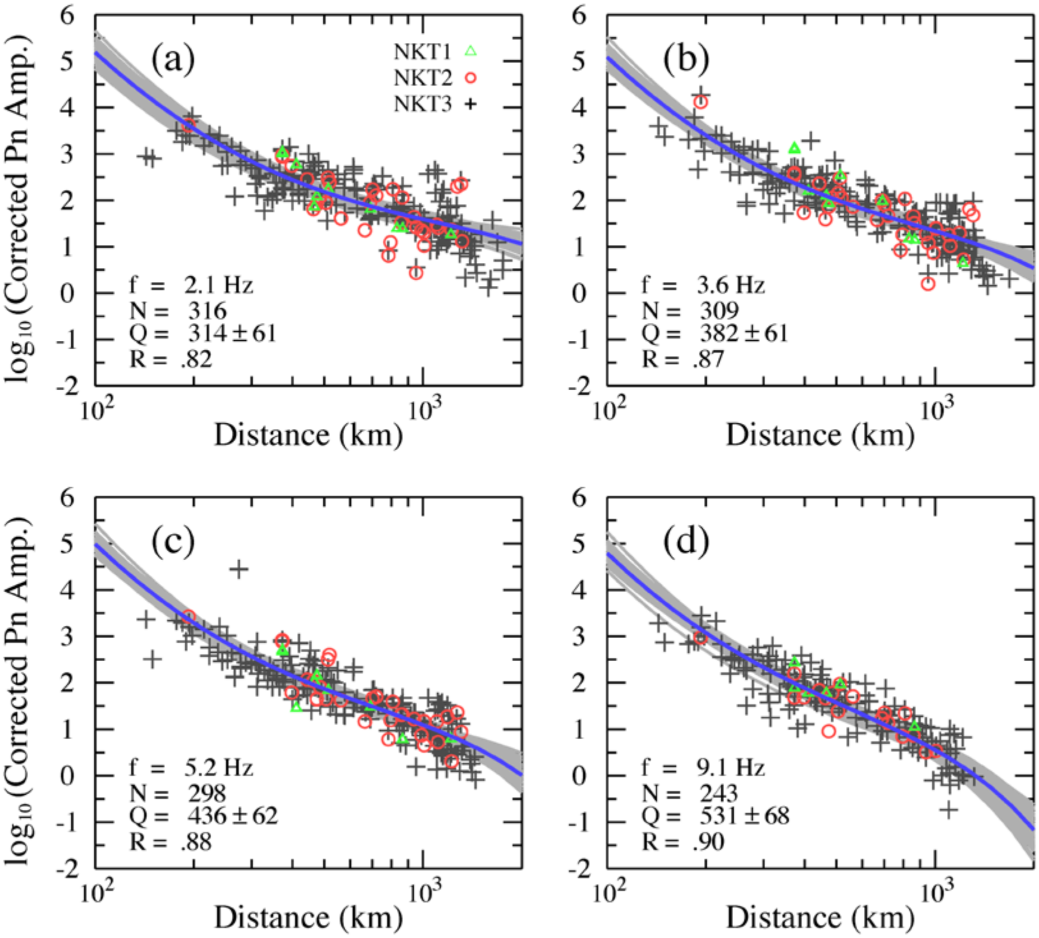

Figure 4. Pn spectral amplitudes versus distance at selected frequencies. The source excitation spectra have been removed. Different symbols indicate data from NKT1 (triangles), NKT2 (circles), and NKT3 (crosses). The solid blue lines are the best-fit Pn spectra with data between 2.0 and 10.0 Hz, and the shaded areas represent their standard deviations. The frequency (f), number of samples (N), apparent Pn Q, and correlation coefficient (R) are labeled in each panel.

Approved for public release; distribution is unlimited.

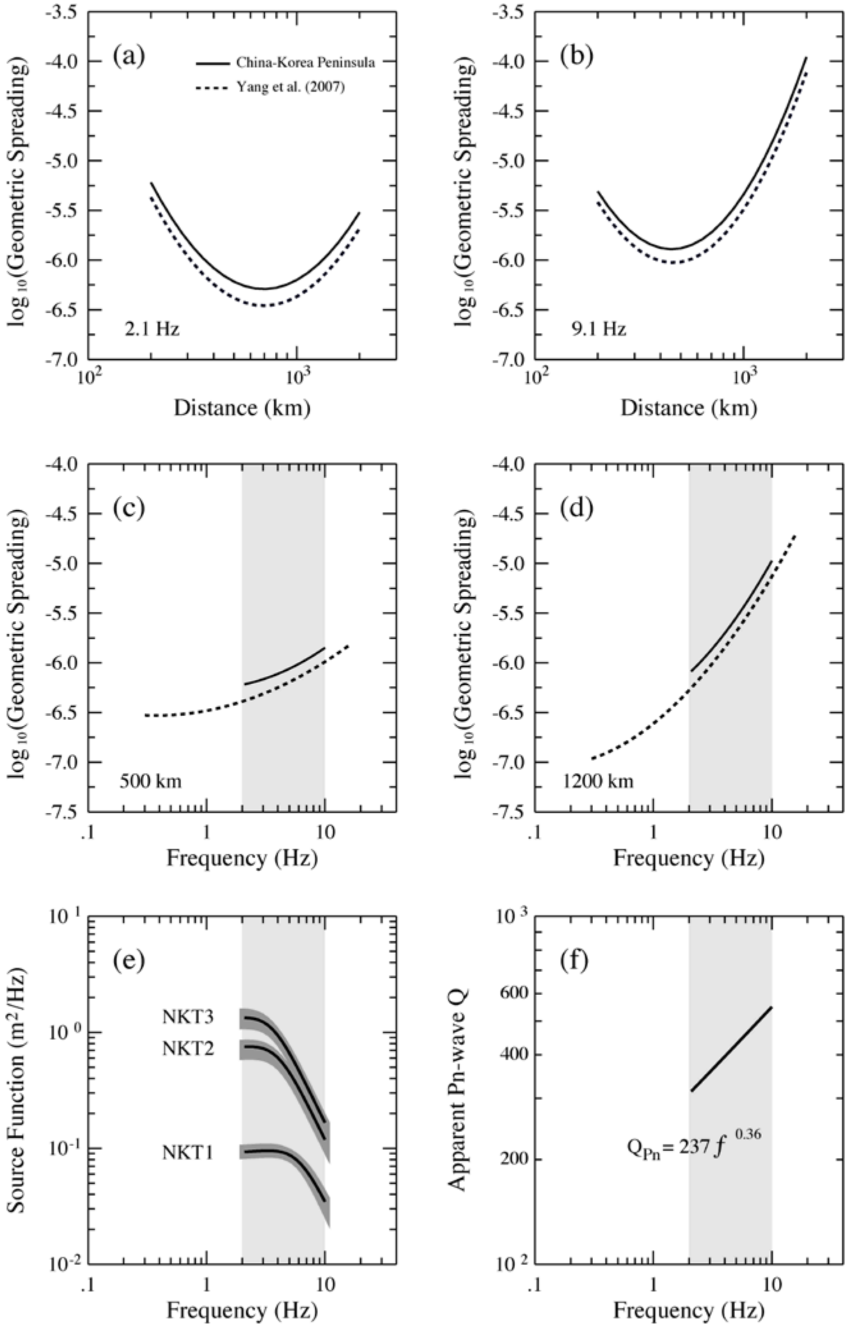

Figure 5. The inverted Pn models. (a) and (b) The Pn geometric spreading functions versus distance at 2.1 and 9.1 Hz. (c) and (d) The Pn geometric spreading functions versus frequency at 500 and 1,200 km. (e) Source excitation functions for three nuclear explosions, and (f) regional average Pn Q versus frequency. The solid lines are the result for Northeast China and the Korean Peninsula obtained using 2.0 to 10.0 Hz data, and the dashed lines represent the model given by*Yang et al.* [2007].

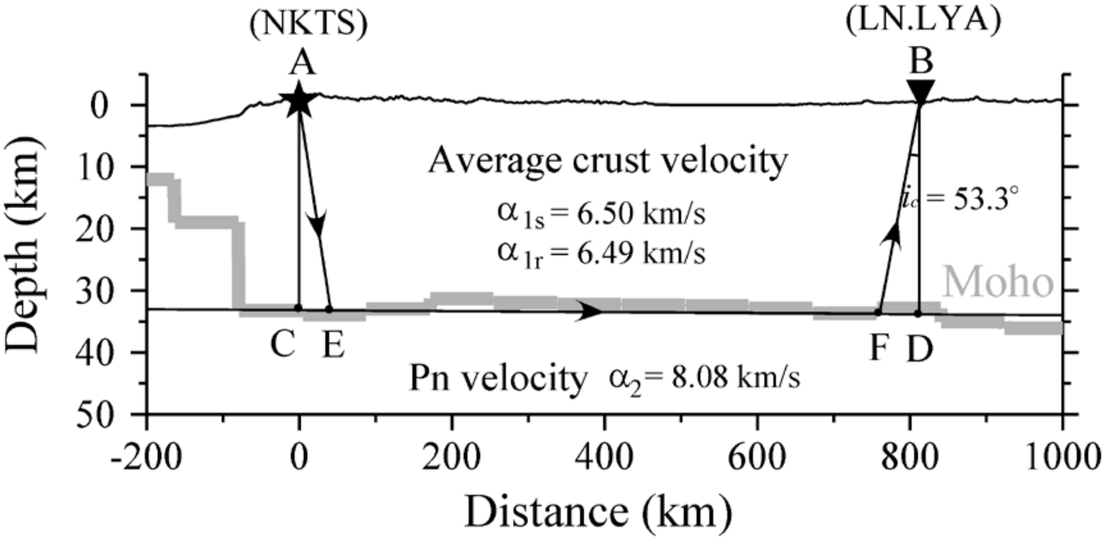

Figure 6. Sketch depicting the Pn-wave propagation path from the NKTS to LN.LYA. The crust model is based on CRUST1.0.

Approved for public release; distribution is unlimited.

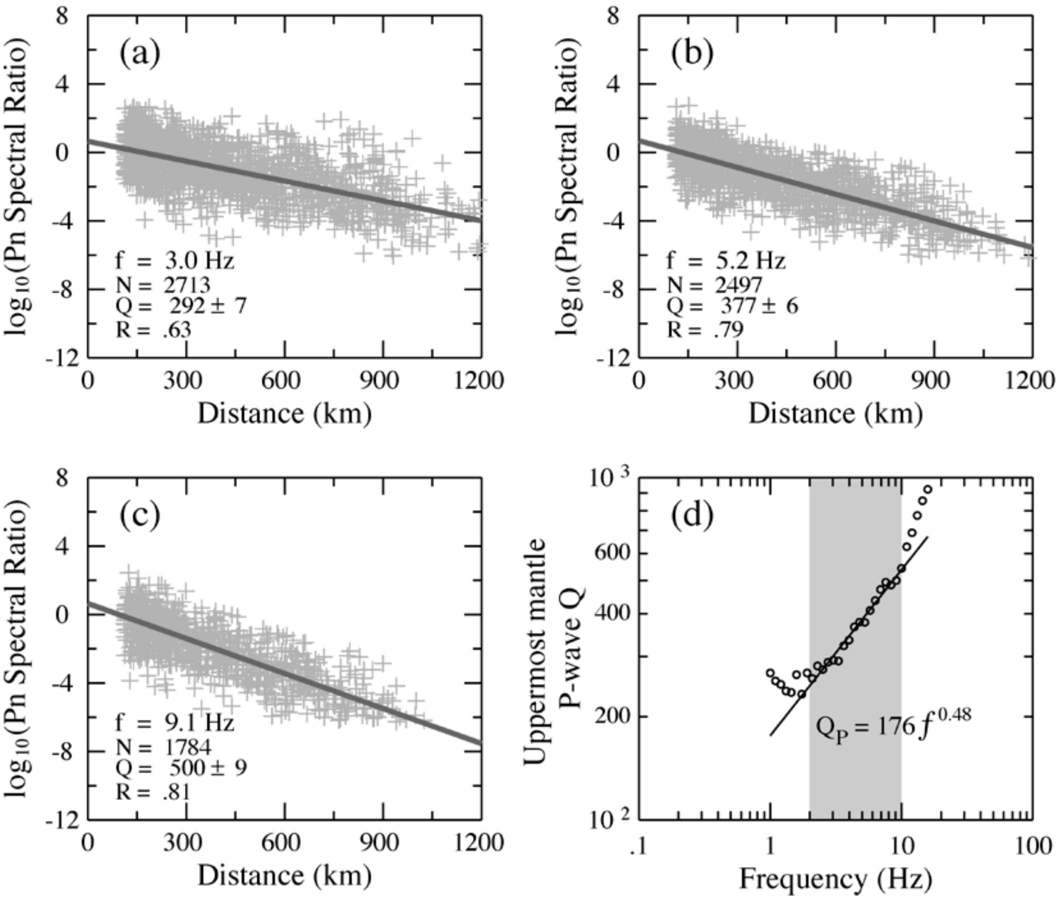

Figure 7. (a) - (c) Spreading-corrected Pn spectral ratios (light gray crosses) versus interstation distance at 3.0, 5.2 and 9.1 Hz. The solid lines indicate linear regressions, and their slopes represent the regional average uppermost mantle P-wave Q. (d) Regional average uppermost mantle P-wave Q (circles) versus frequencies. The solid line is the best-fit power-law Q model using data between 2.0 and 10.0 Hz.

Approved for public release; distribution is unlimited.

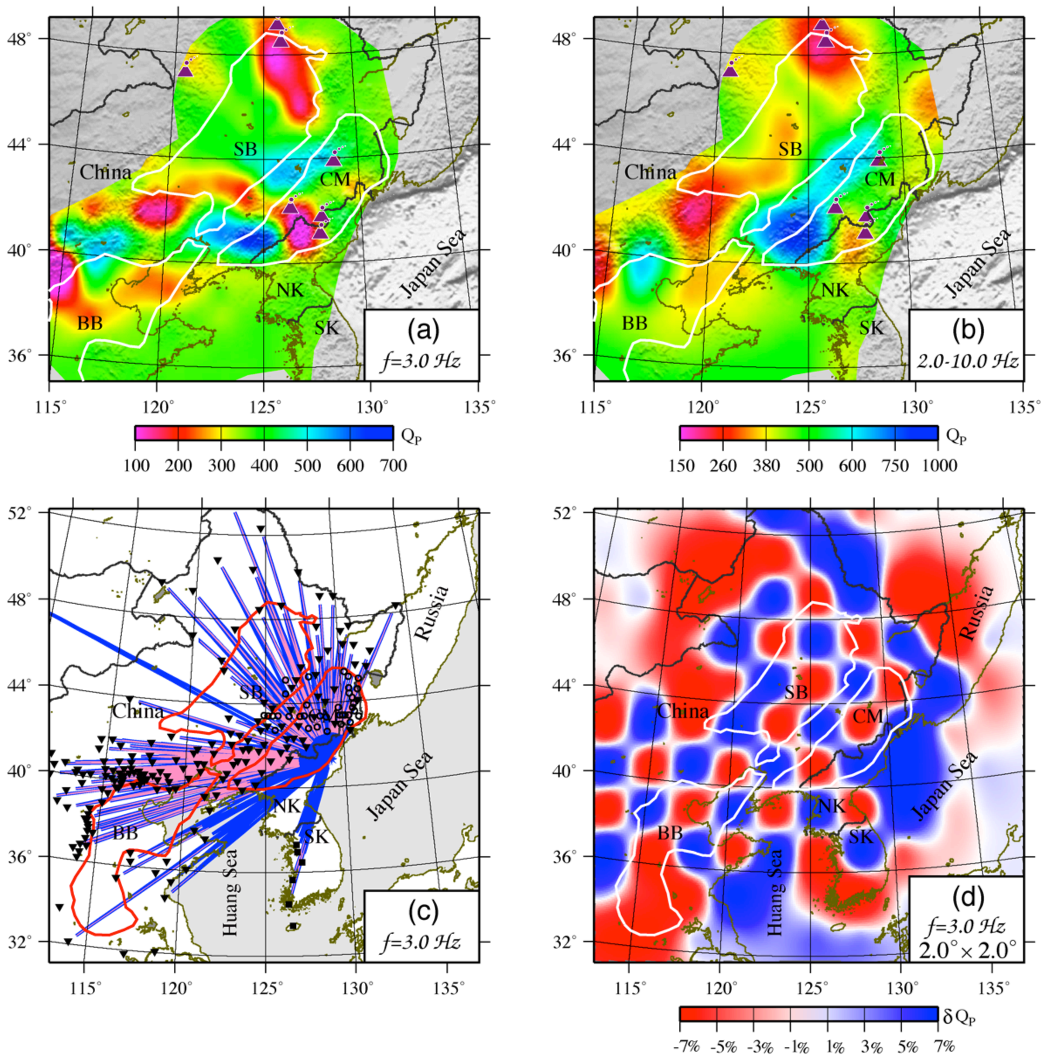

Figure 8. Results for the upper mantle P-wave Q model. (a) Inverted Q map at 3.0 Hz, (b) the broadband Q obtained by averaging logarithmic Q between 2.0 and 10.0 Hz, (c) 3 Hz ray-path coverage, in which the blue and pink lines indicate the single- and two-station paths, respectively, and (d) 2.0° × 2.0° checkerboard test for 3 Hz resolution check.

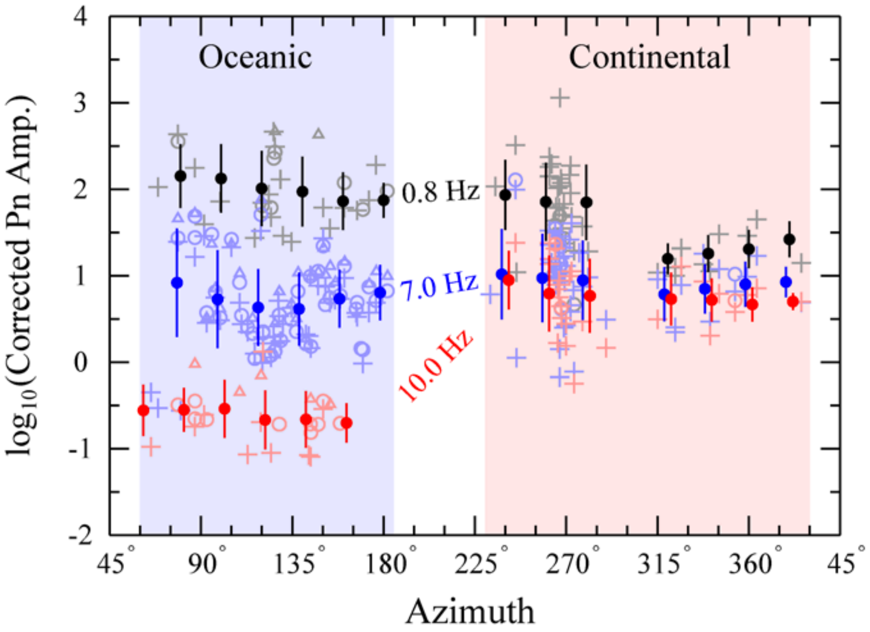

Figure 9. Pn spectral amplitudes at distance 1,000 km versus the azimuth. The triangles, circles and crosses represent NKT1, NKT2 and NKT3, respectively. Black, blue and red colors indicate 0.8-, 7- and 10.0-Hz data, respectively. Solid circles with error bars represent their mean values and standard deviations, obtained within 30-degree azimuth windows. The Pn source excitation functions are removed from the data.

Approved for public release; distribution is unlimited.

DISTRIBUTION LIST

DTIC/OCP
8725 John J. Kingman Rd, Suite 0944
Ft Belvoir, VA 22060-6218 1 cy

AFRL/RVIL
Kirtland AFB, NM 87117-5776 2 cys

Official Record Copy
AFRL/RVBYE/Robert Raistrick 1 cy